Department of Physics and Astronomy
University of Heidelberg

Master Thesis in Physics
submitted by

Nicolas Schmidt

born in Starnberg (Germany)

2017

Neutral meson and direct photon measurements with conversions in ALICE in proton-proton collisions at $\sqrt{s} = 0.9$, 7 and 8 TeV

This master thesis has been carried out by Nicolas Schmidt at the
Physikalisches Institut at the University of Heidelberg
under the supervision of
apl. Prof. Dr. Klaus Reygers
and
Prof. Dr. Johanna Stachel

Abstract

In this thesis the differential invariant cross-sections of the π^0 and η mesons as well as the direct photon excess ratios in pp collisions at $\sqrt{s} = 900$ GeV, $\sqrt{s} = 7$ TeV and $\sqrt{s} = 8$ TeV are presented. The neutral mesons are measured via their two photon decay channel by reconstructing the photons from the electron-positron pairs they produce in interactions with the detector material. For this reconstruction, information from the Time Projection Chamber and the Inner Tracking System is used. This allows the signal extraction of the π^0 (η) mesons down to 0.3 (0.4) GeV/c from the minimum bias triggered datasets at $\sqrt{s} = 7$ and 8 TeV. The resulting fully corrected spectra from the photon conversion method (PCM) are compared to the spectra measured using the ElectroMagnetic Calorimeter (EMCal) and the PHOton Spectrometer (PHOS). The spectra from the different reconstruction methods are combined using their weighted average, considering systematic error correlations. Comparisons to theory predictions show that the transverse momentum spectra of the π^0 and η meson at $\sqrt{s} = 7$ and 8 TeV are significantly overestimated by NLO calculations. The direct photon measurement is based on the measured inclusive sample of converted photons and utilizes decay simulations as well as the measured neutral pion spectra. This allows for the calculation of the direct photon excess ratio. This double ratio is consistent with unity and NLO predictions within the uncertainties and therefore no significant direct photon excess is observed in the analyzed data of pp collisions.

Zusammenfassung

In dieser Arbeit werden die invarianten Wirkungsquerschnitte von π^0 und η Mesonen, sowie die Überschussverhältnisse direkter Photonen in Proton-Proton Kollisionen bei Schwerpunktsenergien von $\sqrt{s} = 900$ GeV, $\sqrt{s} = 7$ TeV und $\sqrt{s} = 8$ TeV präsentiert. Die neutralen Mesonen werden über den zwei-Photon Zerfallskanal gemessen, wobei die Photonen aus Elektron-Positron Paaren rekonstruiert werden, welche durch Wechselwirkungen mit dem Detektormaterial erzeugt wurden. Die Rekonstruktion basiert auf Informationen, die von der Time Projection Chamber und dem Inner Tracking System geliefert werden. Dies ermöglicht die Signalauslese des π^0 (η) Mesons bereits ab 0.3 (0.4) GeV/c in den $\sqrt{s} = 7$ und 8 TeV Minimum-Bias Daten. Die vollständig korrigierten Spektren der Photon Conversion Method (PCM) werden zudem mit den Spektren aus Kalorimeter-basierten Messungen mit dem ElectroMagnetic Calorimeter (EMCal) und dem PHOton Spectrometer (PHOS) verglichen. Über das gewichtete Mittel werden die Spektren der unterschiedlichen Rekonstruktionsmethoden daraufhin kombiniert, wobei Korrelationen der systematischen Fehler berücksichtigt werden. Der Vergleich der kombinierten Transversalimpulsspektren von π^0 und η aus den $\sqrt{s} = 7$ und 8 TeV Messungen mit theoretischen Berechnungen zeigt eine deutliche Überschätzung der Daten durch die NLO Berechnungen. Die Messung der direkten Photonen basiert auf dem gemessenen Spektrum konvertierter inklusiver Photonen und verwendet zudem Zerfallssimulationen, sowie die gemessenen Spektren der neutralen Pionen. Hierdurch kann dann das direkte Photonen Überschussverhältnis berechnet werden. Das Überschussverhältnis stimmt innerhalb statistischer und systematischer Fehler mit einem Wert von eins, sowie den NLO Berechnungen überein und zeigt somit keinen signifikaten Überschuss an direkten Photonen in den analysierten Proton-Proton basierenden Datensätzen.

Contents

1 Introduction

> *"Nature uses only the longest threads to weave her patterns, so each small piece of her fabric reveals the organization of the entire tapestry."*
>
> Richard Feynman (1918–1988)

There is a certain fascination in studying the smallest structures of the universe and in return gaining deeper insights about the evolution of the universe itself. This interesting link can be studied at the Large Hadron Collider (LHC), which is the largest and most powerful particle accelerator to date. It allows to accelerate and collide protons with center-of-mass energies up to $\sqrt{s} = 14$ TeV as well as heavy ions with a maximum of $\sqrt{s_{\mathrm{NN}}} = 5.02$ TeV per nucleon pair. Such high energies have not been archived before and enable testing of theoretical models like the Standard Model. The latest member of this Model, the Higgs boson, was predicted already in the 1960s, but first measured by using high energy proton-proton collisions at the LHC. Furthermore, many important particle properties like rare decays or CP violation can be measured with a much greater precision using high energy collisions. Besides protons, also heavy-ions are used in the LHC whose collisions produce the quark-gluon plasma, a strongly coupled form of matter, which is believed to have existed shortly after the Big Bang.

The dedicated heavy-ion collisions detector system at the LHC is ALICE (A Large Ion Collider Experiment), which is also the detector system used for this thesis. Being capable of handling very high charged-particle densities, it can investigate the properties of the quark-gluon plasma by measuring and identifying particles originating from this medium with great precision.

The content of this thesis is the measurement of the neutral mesons, π^0 and η, as well as direct photons in proton-proton collisions at $\sqrt{s} = 0.9$, 7 and 8 TeV. The two photon decay channel is used for the detection of neutral mesons and photons are reconstructed using the photon conversion method.

The thesis starts with a theoretical overview in the next chapter explaining the necessary knowledge for the contents of this thesis followed by an explanation of the experimental setup in Chapter 3. This includes the accelerator system, the ALICE detector system as well as the software framework that is used for the analysis. Chapter 4 introduces the different data sets from the three center-of-mass energies and discusses the event selection as well as the quality of the data sets. Afterwards, the photon conversion method is explained as well as the cuts used in the analysis to obtain clean photon samples. Chapter 6 explains the necessary steps to get the corrected neutral meson spectra and provides the results including systematic uncertainties. The following chapter is then focused around the direct photon measurement and the thesis ends with a summary as well as an outlook.

2 Theoretical Overview

This section will focus on the basic concepts of particle physics. An introduction to the fundamental particles and the basic theoretical structure of the Standard Model (SM) will be given as well as more detailed descriptions of the particles measured in this thesis.

2.1 The Standard Model and Quantum Chromodynamics

The fundamental particles and their interactions through the electromagnetic, strong and weak force are described by the Standard Model, which is a Quantum Field Theory (QFT) that is self-consistent and able to describe a large fraction of the experimental data with outstanding precision [1]. The latest addition to this model is the Higgs boson which serves as an exchange particle of the higgs mechanism [2, 3].

Within the Standard Model, the fundamental particles are split into two categories, half-integer spin fermions and bosons with integer spin. The fermions are subdivided into 6 quarks (up, down, charm, strange, bottom, top) and 6 leptons (electrons, muons, tauons and their corresponding neutrinos). These particles carry different charges with respect to the three SM forces (weak, strong and electromagnetic) and can therefore be distinguished by this property. In addition, for each particle an anti-particle with opposite charge considering their interaction, but same mass exists.

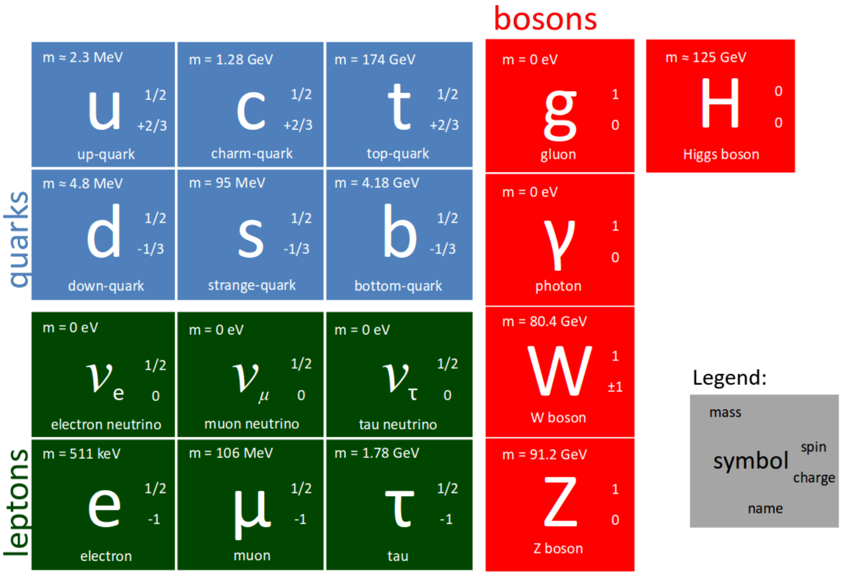

Figure 2.1: Fundamental particles of the Standard Model.[4]

Quarks experience the strong interaction due to the color charge they carry. Consistent with the theoretical expectation of confinement [5], no free colored particles have yet been observed. Instead, quarks are combined into colorless particles which are called hadrons. These are either quark-antiquark pairs or states of three quarks, called mesons and baryons, respectively. Furthermore, they can also form tetra- and pentaquarks, which are made of four or five quarks [6]. Quarks themselves can either be up-type quarks with an electric charge of $Q = +\frac{2}{3}$ and weak isospin $T_3 = +\frac{1}{2}$ or down-type quarks with $Q = -\frac{1}{3}$ and $T_3 = -\frac{1}{3}$.

Most of the matter around us is made of first generation quarks, meaning up- (u) and down-quarks (d). As seen in the overview of the Standard Model particles in Figure 2.1, these are the lightest quarks with masses of only a few MeV. The quark masses increase with each generation and peak at the top-quark mass with 174 GeV.

The leptons, which make the other half of the fermions, do not carry a color charge and can also be subdivided into two groups depending on the electric charge: The electron (e), the muon (μ) and the tauon (τ) with an electric charge of $Q = -1$ and the neutrinos. The latter do not carry an electric charge and can therefore only interact via the weak interaction.
The interactions between fermions are mediated via the exchange of gauge bosons carrying spin 1. Electromagnetic, weak and strong interaction each employ different bosons. The massless photons (γ) mediate the electromagnetic force whereas the weak force employs the heavy $W^{\pm}$ and Z bosons. The gauge bosons mediating the strong interaction carry a color charge and are called gluons. Therefore they interact not only with the quarks but also with each other.

In the quark interactions, gluons take a comparable role to photons in quantum electrodynamics (QED), which mediate the electromagnetic interaction between two charged currents. To describe the strong force, a non-abelian quantum field theory called Quantum Chromodynamics that is based on the gauge group SU(3). In Quantum Chromodynamics (QCD), the color quantum number takes the same role as the charge in electromagnetic interactions. Due to the degrees of freedom in SU(3), the color charge can take one of three values (red, blue, green). However, every bound state of quarks has to be colorless. The Lagrangian density of QCD [7, 8] can be expressed as:

$$\mathcal{L} = \sum_q \overline{\psi_q} \gamma^\mu \left(i\partial^\mu - g_s A_a^\mu \frac{\lambda_a}{2} \right) \psi_q - \sum_q m_q \overline{\psi_q} \psi_q - \frac{1}{4} \sum_a F_a^{\mu\nu} F_{\mu\nu,a} \tag{1}$$

where ψ_q corresponds to the quark field, g_s to the effective strong coupling constant, A_q^μ to a gluon field, λ_a to the Gell-Mann matrices [9] and the gluon field strength tensor given by:

$$F_a^{\mu\nu} = \partial^\mu A_a^\nu - \partial^\nu A_a^\mu + i g_s f_{abc} A_\mu^b A_\nu^c \tag{2}$$

For massless particles, the QCD Lagrangian is invariant under the exchange of right- and left-handed components of the quark spinor. This invariance, called chiral symmetry, is explicitly broken for quark where is generates the quarks' rest mass. The strong force between quarks and anti-quarks would even lead for massless quarks to a rise of a so-called chiral condensate [10], which, in addition, is not invariant under the exchange of right- and left-handed fermions. The fact that the chiral symmetry of the QCD Lagrangian can spontaneously break, leads to the Goldstone bosons, which are massless and carry spin 0. However, as chiral symmetry is not exact in nature, the Goldstone bosons are identified as the lightest mesons, for example the neutral pion, the charged pions, kaons as well as the η meson [11].

Quarks couple in QCD with the strength g_s, which can also be written as $\alpha_s = g_s^2/4\pi$ [8]. However, the coupling strength α_s has to be determined from experiments as QCD is not able to predict its value. In addition, $\alpha_s = g_s^2/4\pi$ depends on the momentum transfer (Q) and can therefore be larger than the Quantum Electrodynamics (QED) coupling constant $\alpha_{\text{em}} \approx \frac{1}{137}$ for the right values of Q. The dependence of α_s on the momentum transfer in the leading order can be written in the following form which, however, can only be used if $Q^2 \gg \Lambda^2$:

$$\alpha_s(Q^2) \approx \frac{12\pi}{(33 - 2N_f)\ln\frac{Q^2}{\Lambda^2}} \tag{3}$$

Here, N_f stands for the number of available quark flavors and Λ represents the QCD scaling parameter which has been experimentally determined to be ≈ 200 MeV.

Quark pairs ($q\bar{q}$) form a potential between each other which, in an approximated form, can be described with:

$$V_s = -\frac{4}{3}\frac{\alpha_s}{r} + kr. \tag{4}$$

The distance between the quarks is hereby expressed by r. The different r dependence in both terms leads to very important consequences for the $q\bar{q}$-interaction. The first term dominates at small distances and acts similar to a Coulomb-like interaction. The second term with its linear dependence on r leads to a growth in the potential with increasing distances. This has the consequence that it would take an infinite amount of energy to separate two quarks completely by removing one quark from its bound state. Furthermore, this behavior leads to the creation of a new quark-anti-quark pair from the huge potential stored in the vacuum. The creation of this new quark pair is called hadronization.

The last member of the fundamental SM particles is the Higgs boson which carries spin 0 and charge 0. The particle itself is an excitation of a component of the Higgs field, which is believed to explain the masses of the fundamental particles found in the Standard Model. It was first observed by the ATLAS and CMS collaborations in 2012 [12, 13] and lead to the Nobel Prize in Physics of 2013 being awarded to Peter W. Higgs [2] and Francois Englert [3] for their theoretical prediction of the mechanism and particle.

2.2 The Quark Gluon Plasma

At high energies, hadronic matter dissolves into its constituent quarks and gluons as a consequence of asymptotic freedom and the implied weakening of the confinement condition. This state of deconfied matter, i.e. quasi-free quarks and gluons, is called Quark-Gluon Plasma (QGP). The QGP is believed to have existed shortly after the Big Bang. The critical temperature T_c at which normal matter transitions into a QGP has been estimated to be about 100-250 MeV [14]. In addition, Hagedorn proposed a limiting temperature for hadronic systems of 140 MeV already in the 1960s [15]. The phase diagram shown in Figure 2.2 depicts the transition of confined to deconfined matter depending on the temperature and the baryon chemical potential. The figure also visualizes the experiments that can reach the critical temperature in their particle collisions as well as the expected evolution of the early universe in the T-μ_B plane.

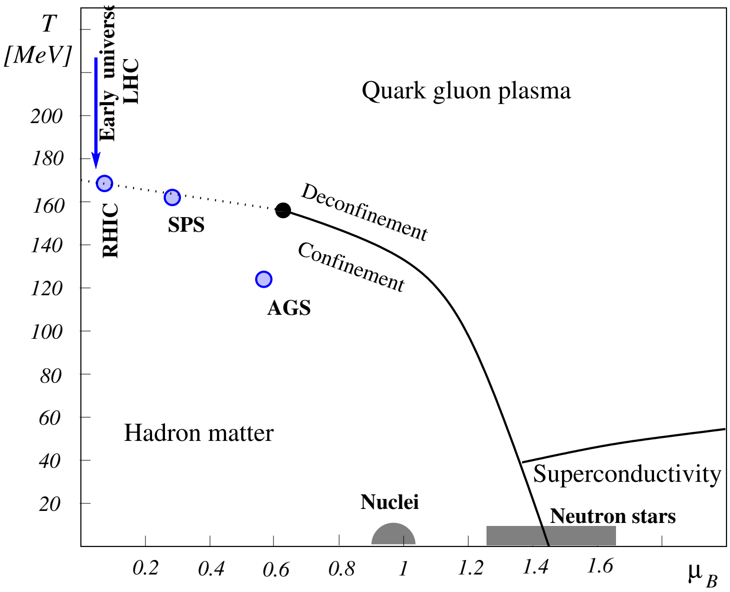

Figure 2.2: The phase diagram of QCD in the T - μ_B plane. Chemical freeze-out conditions for AGS, SPS and RHIC are shown as well as the low temperature and chemical potential region where matter experiences confinement into hadrons. The solid line indicates the phase transition at higher temperatures into a quark-gluon plasma. A critical point at $\mu_B \sim 0.7$ is given, where higher densities will lead to more exotic phases. In addition, the blue arrow illustrates the evolution of matter shortly after the Big Bang and before the chemical freeze-out in LHC collisions. [16]

More recently, calculations of T_c employ Lattice QCD (LQCD), which uses non-pertubative calculations of QCD on a space-time lattice. This allows for calculations of interactions in the low momentum transfer region, which leads to more precise values of $T_c \sim 150 - 160$ MeV at vanishing baryon chemical potential $\mu_B \approx 0$ [17, 18]. In addition, the critical temperature varies depending on the flavors used in LQCD [19, 20]. In the transition of hadronic matter to the deconfined phase, the hadrons split up into their quarks and gluons which therefore increases the number of degrees of freedom of the system. Figure 2.3 shows this behavior as a strong rise of the energy density around the critical temperature. The flattening behavior after the raise comes from no additional degrees of freedom being introduced to the medium and instead it only experiences increased heating. In addition, the Stephan Boltzmann limit is indicated with the horizontal dotted line where the medium can be, due to its asymptotic freedom, be described as an ideal gas.

For the production of the QGP it is necessary that the system can reach a state of thermal equilibrium for the thermodynamic quantities to be defined [21, 22]. The large amount of particles produced in high multiplicity heavy-ion collisions is the driving factor for the medium to reach an equilibrated state, as from the vast amount of particles, many will likely interact with the medium. In addition, the medium must have a minimum lifetime in order to reach thermal equilibrium.

The fireball that is produced in heavy-ion collisions experiences two stages during its lifetime. The first stage is before the equilibrium and is dominated by hard processes including jets or prompt photons, whereas the second stage, after reaching the thermal equilibrium and a temperature above T_c, is dominated by soft processes. These processes will be explained in more detail in Section 2.4. When the temperature drops below T_c

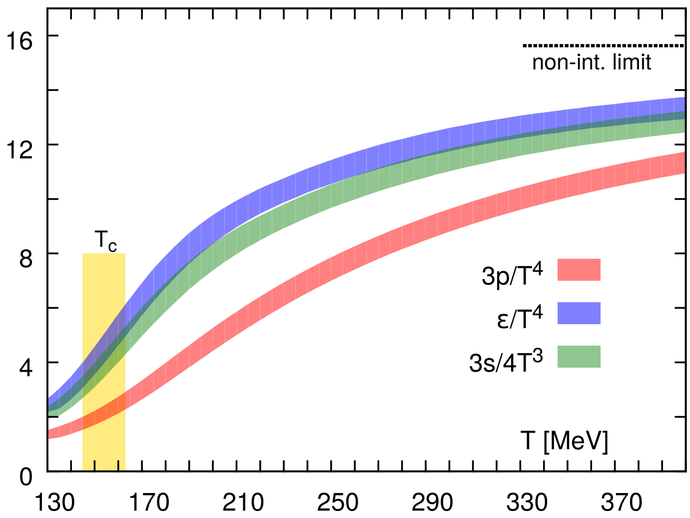

Figure 2.3: Normalized pressure, energy, and entropy density as a function of the temperature in MeV. The ideal gas limit for the energy density is given by the horizontal line and the vertical band shows the critical temperature region of $T_c = (154 \pm 9)$ MeV. [23, 24]

due to the expansion of the system, the quarks will recombine into hadrons and form a so-called hadron gas. With further expansion of the system, the freeze-out happens where the hadrons do no longer interact with each other.

To probe the QGP many different methods are available. However, the most relevant probe for which results of this thesis can be used as ingredients is the nuclear modification factor R_{AA} [25–27]. The nuclear modification factor represents the modification of the particle spectra due to medium interactions in heavy-ion collisions compared to the particle spectra in proton-proton collisions where no medium is expected. The factor itself is based on the idea that the spectra from heavy-ion collisions should just be a superposition of several proton-proton collisions. It is calculated using:

$$R_{\mathrm{AA}}(p_{\mathrm{T}}) = \frac{\mathrm{d}^2 N_{\mathrm{AA}}/\mathrm{d}p_{\mathrm{T}}\mathrm{d}y}{\langle T_{\mathrm{AA}}\rangle \cdot \mathrm{d}^2\sigma_{\mathrm{pp}}/\mathrm{d}p_{\mathrm{T}}\mathrm{d}y}, \tag{5}$$

where the nuclear overlap function, which stands for the expected number of superimposed proton-proton collisions that would represent a single heavy-ion collision, is given by:

$$\langle T_{\mathrm{AA}}\rangle = \frac{\langle N_{\mathrm{coll}}\rangle}{\sigma_{\mathrm{pp}}^{\mathrm{inel}}}. \tag{6}$$

Deviations of the nuclear modification factor from unity would mean a modification of the heavy-ion spectra due to nuclear or medium effects. As the calculation of the nuclear modification factor relies on the proton-proton spectrum as input, it is one goal of this thesis to provide a well understood and corrected spectrum. In addition, for heavy-ion collisions at different center-of-mass energies than the presented pp energies, the spectra can also be used for calculating well constrained interpolation spectra.

2.3 The Neutral Mesons

The neutral mesons discussed in this thesis are the neutral pion π^0 and the η meson. Both are composed of superpositions of quark and anti-quark pairs which can be written as:

$$
\begin{aligned}
|\pi^0\rangle &= \frac{1}{\sqrt{2}}\left(|u\overline{u}\rangle - |d\overline{d}\rangle\right),\\
|\eta^0\rangle &= \frac{1}{\sqrt{6}}\left(|u\overline{u}\rangle + |d\overline{d}\rangle - 2|s\overline{s}\rangle\right).
\end{aligned}
$$

With a rest mass of approximately 135 MeV/c^2 the π^0 is the lightest meson and can therefore not decay into other mesons. Instead it decays electromagnetically with a mean lifetime of the order of 10^{-16} seconds. The η meson is much heavier, with a rest mass of 547 MeV/c^2 [28]. While for the neutral pion the dominant decay is $\pi^0 \rightarrow \gamma\gamma$ with a branching ratio of more than 98%, the η meson only decays in about one third of its decays into two photons [29]. The full list of branching ratios which include photons is given in Table 13. The typical π^0 and η meson Feynman diagram for the decay into two photons is shown in Figure 2.4.

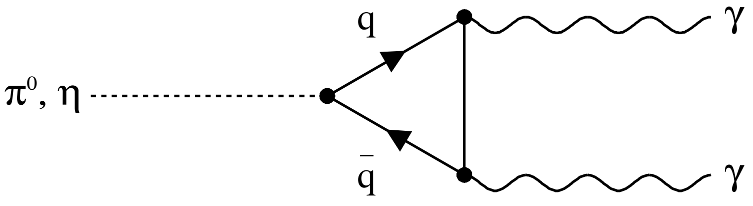

Figure 2.4: Feynman diagram for the decay of the neutral mesons into two photons.

The neutral mesons are an important measurement for all collision types as they are produced in vast amounts and therefore are responsible for the majority of decay photons found in the detector. Due to their large abundance they can usually be observed with a good signal to background ratio and therefore be measured with good precision.

2.4 Photons in High Energy Collisions

The use of photons as probes in high energy or heavy-ion collisions is beneficial since they only interact electromagnetically and can therefore deliver information about the collision and the fireball evolution outwards of the medium. In addition, their mean free path length is much larger than the medium itself [30]. This makes photons an important probe for the early stages of the collision compared to hadrons which would be affected in different ways by the quark-gluon plasma. Photons with high transverse momentum can additionally be used to test pQCD calculations. The processes at these momenta are called hard processes as they involve a large momentum transfer. On the other hand, the low momentum transfer processes are called soft processes which can be calculated by using lattice QCD. Measuring the photons from both, soft and hard, processes is a difficult task as the vast majority of photons measured from the collisions originate in electromagnetic decays with the neutral pion being responsible for more than 80% of those decay photons. The photons that do not originate from particle decays are called

direct photons which can then be subdivided into categories based on their production mechanisms.
The first category is composed of photons from hard processes, i.e. prompt or fragmentation photons, with the latter being byproducts of hadronization processes. The prompt photons are produced for example from Compton scattering or quark-antiquark annihilation which are 2 → 2 processes. These photons are the dominant contribution to the direct photon at large transverse momentum.
A further source of direct photons are photons from soft processes which indicate the formation of the strongly interacting medium, the quark-gluon plasma, in heavy ion collisions. These photons are produced in the same processes as the photons from hard processes, however with the difference that they do not originate from the collision itself but instead from interactions of thermalized particles. The thermal photons are emitted from a thermally equilibrated phase during the QGP and hadron gas stages. Photon production rate and p_{T} distribution depend on the emission temperature of the photons. These photons therefore allow to extract information on the thermodynamical state of the medium from the moment they were produced in the medium.
The direct photon signal is extracted by isolating the photons coming from soft and hard processes from the full photon sample including the decay photons. However, this is an experimentally challenging task as the vast amount of decay photons strongly suppresses the direct photon signal. The approach for the extraction therefore employs a double ratio that compares the ratio of the measured photon spectrum to the measured neutral pion spectrum with the same ratio obtained from a decay simulation where measured spectra are used as input. The direct photon excess ratio is calculated using the following double ratio:

$$R_\gamma = \frac{(\gamma_{\mathrm{inc}}(p_{\mathrm{T}})/\pi^0(p_{\mathrm{T}}))_{\mathrm{meas}}}{(\gamma_{\mathrm{dec}}(p_{\mathrm{T}})/\pi^0(p_{\mathrm{T}}))_{\mathrm{sim}}} \approx \frac{\gamma_{\mathrm{inc}}(p_{\mathrm{T}})}{\gamma_{\mathrm{dec}}(p_{\mathrm{T}})} \tag{7}$$

The use of ratios has the advantage of a partial cancellation of systematic uncertainties and a general normalization in the nominator and denominator. The direct photon spectrum itself is then obtained by subtracting the decay photons from the inclusive photons:

$$\gamma_{\mathrm{dir}}(p_{\mathrm{T}}) = \gamma_{\mathrm{inc}}(p_{\mathrm{T}}) - \gamma_{\mathrm{dec}}(p_{\mathrm{T}}) = \gamma_{\mathrm{inc}}(p_{\mathrm{T}}) \cdot \left(1 - R_\gamma^{-1}(p_{\mathrm{T}})\right) \tag{8}$$

The calculation of this spectrum for the three center-of-mass energies $\sqrt{s} = 0.9$, 7 and 8 TeV is the goal of this thesis. This will require a well understood measurement of the dominant decay photon contributors, the neutral mesons, as well as the extraction of a fully corrected inclusive photon spectrum.

3 The Experimental Setup

In this chapter, the accelerator and detector setup are explained. For this, the important detector subsystems and their properties as well as their purpose are introduced. Furthermore, an introduction to the analysis software framework is given.

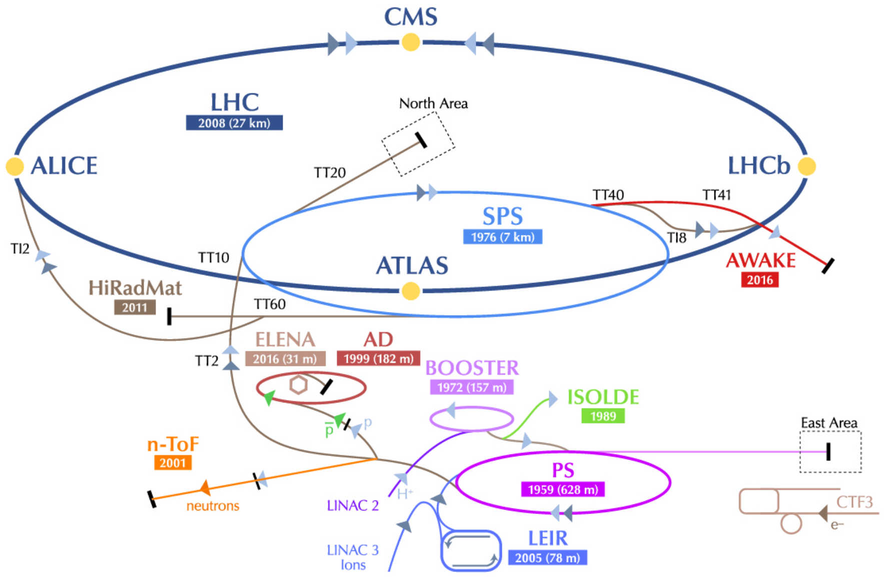

Figure 3.1: Overview of the CERN accelerator complex including the four main LHC experiments: ALICE, CMS, LHCb and ATLAS. Image derived from [31].

3.1 The LHC Experiment

The 27 km circumference Large Hadron Collider (LHC) at the European Organization for Nuclear Research (CERN) in Geneva on the Franco-Swiss border is currently the most powerful and largest particle accelerator in the world. After starting its operation in the year 2008 with the first proton beams at low energy, it stepwise increased its beam energies until the latest maximum of $\sqrt{s}$ = 13 TeV in proton-proton collisions. Being designed for a maximum center of mass energy of $\sqrt{s}$ = 14 TeV as well as a peak luminosity of $\mathscr{L} = 10^{34}$ cm^{-2}s^{-1} for proton-proton collisions or $\sqrt{s_{\mathrm{NN}}}$ = 5.02 TeV and $\mathscr{L} = 10^{27}$ cm^{-2}s^{-1} per nucleon-nucleon pair for Pb-Pb collisions it is stronger than any other collider by a factor of seven.

The LHC with its two beam pipes and eight interaction points was placed inside the tunnel of the Large Electron Positron Collider (LEP) which is on average 100 m under ground. The beam pipes are kept at an ultra-high vacuum of $\approx 10^{-17}$ bar [32]. Eight sections containing a total amount of 1232 dipole magnets keep the LHC beams in their orbits. The dipole magnets can generate a field of 8.36 T while being cooled down to superconductivity at 1.9 K during operation. In addition, several quadrupole magnets are used to focus the beams and acceleration cavities further increase the beam energies. The beam itself is created by stripping electrons from hydrogen atoms and injecting the protons into the LHC pre-accelerator chain. This chain is shown in Figure 3.1 and includes

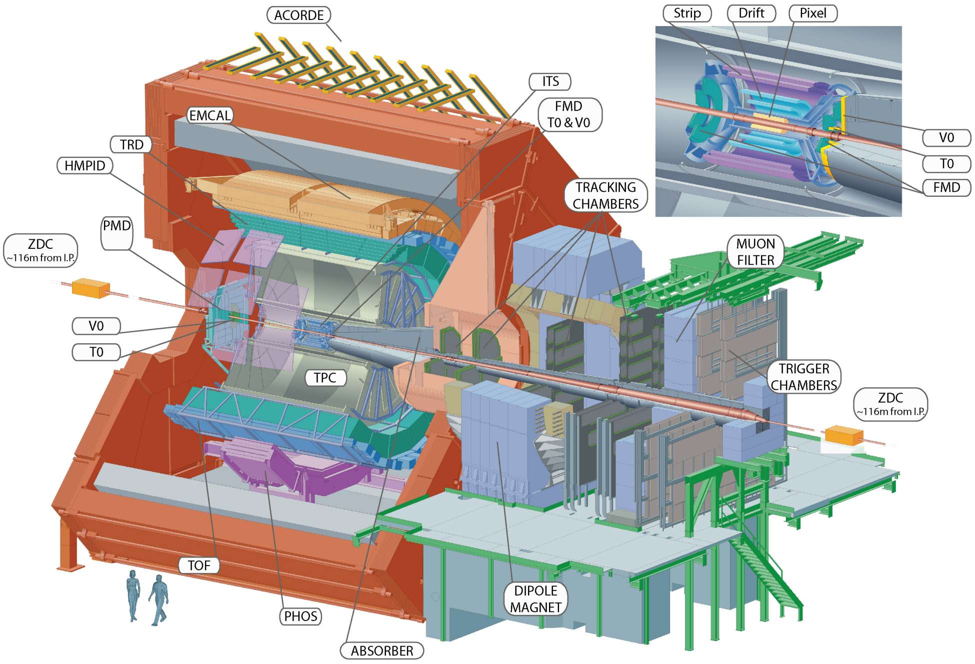

Figure 3.2: The ALICE experiment with all detector systems [37]. The inner barrel, contained in the red solenoid magnet, contains all detector systems used in this thesis. The forward muon spectrometers can be found further along the beam axis.

the Linear Accelerators (LINACS), the Proton Synchrotron Booster (PSB), the Proton Synchrotron (PS) and the Super Proton Synchrotron (SPS) in order to inject the beams with 450 MeV into the LHC where they are further accelerated to a current maximum of 6.5 TeV [32, 33].
Four of the eight interaction points of the LHC are equipped with huge detector systems as shown in Figure 3.1. Each experiment is designed to investigate different characteristics of the collisions and therefore different kinds of physics. The only dedicated heavy-ion experiment is ALICE and will be described in the following sections. A Toroidal LHC Apparatus (ATLAS) and the Compact Muon Solenoid experiment (CMS) are general purpose detector systems designed for measurements of each particle originating from a primary collision. Both experiments were involved in the Higgs boson discovery in 2012 [12, 13]. In addition, they focus their measurements on confirming or possibly providing theories for extending the standard model. Being equipped with different kinds of detectors, both experiments also investigate charge parity violation, super symmetries, additional dimensions as well as possible dark matter particles [34, 35]. The LHC beauty experiment (LHCb) is used to investigate hadron decays containing charm or bottom quarks as well as the study of CP violation. In addition, the experiment tries to improve the understanding of the asymmetry of matter and antimatter in the universe as the Standard Model fails to fully describe this phenomenon [36].

3.2 A Large Ion Collider Experiment

A Large Ion Collider Experiment (ALICE) is the dedicated general-purpose LHC experiment for heavy ion collision measurements [38]. The detector is therefore designed to handle high multiplicities while still delivering good particle identification (PID). Its

Detector	η acceptance	ϕ acceptance	position	main purpose
ITS				
SPD 1(2)	± 2 (± 1.4)	full	$r = 3.9$ (7.6) cm	tracking, vertex
SDD	± 0.9	full	$r = 15.0$ (23.9) cm	tracking, PID
SSD	± 1	full	$r = 38$ (43) cm	tracking, PID
V0				
T0				
TPC	± 0.9	full	$85 < r/\text{cm} < 247$	tracking, PID
TRD	± 0.8	full	$290 < r/\text{cm} < 368$	tracking, $e^{\pm}$ id
TOF	± 0.9	full	$370 < r/\text{cm} < 399$	PID
PHOS	± 0.12	$220° < \phi < 320°$	$460 < r/\text{cm} < 478$	photons
EMCal	± 0.7	$80° < \phi < 187°$	$430 < r/\text{cm} < 455$	photons and jets
HMPID	± 0.6	$1.2° < \phi < 58.8°$	$r = 490$ cm	PID

Table 1: Different detector systems of the ALICE experiment including their coverage and purpose [39].

main task is the study of the quark-gluon plasma for which it also requires a high momentum resolution, especially at low transverse momentum. The ALICE detector and its subsystems can be seen in Figure 3.2. Embedded in the red solenoid magnet from the L3 experiment at LEP are the detector systems from the central barrel. The magnet provides a magnetic field of up to 0.5 T that is aligned with the beam pipe. The central barrel detector systems are responsible for tracking, vertex finding and particle identification. Closest to the beam pipe is the Inner Tracking System (ITS), followed by the Time Projection Chamber (TPC), the Transition Radiation Detector (TRD), the Time-Of-Flight detector (TOF) and the High Momentum Particle Identification Detector (HMPID) as well as two calorimeters: the Photon Spectrometer (PHOS) and the Electromagnetic Calorimeter (EMCal). Table 1 shows the coverage, position and main purpose of the central barrel detector systems.

Outside of the central barrel along the beam pipe are the forward muon spectrometers which are placed behind thick layers of absorbing material. The following sections will introduce the different central barrel detector systems shown in Figure 3.2. As the muon spectrometers and the ALICE cosmic ray detector (ACORDE) are not part of this thesis they will not be further discussed.

3.2.1 V0 Detector (V0)

The V0 detector [40] is one of the three forward detectors and is composed of two scintillator arrays, V0A and V0C, which are located at $z = 340$ cm and $z = 30$ cm respectively on both sides from the interaction point along the beam axis. They cover pseudorapidity ranges of $2.8 < \eta < 5.1$ for the V0A and $-3.7 < \eta < -1.7$ for the V0C. The V0 detector system is used as a Minimum Bias (MB) trigger and also provides multiplicity information for centrality estimations in heavy ion collisions [41, 42].

3.2.2 Inner Tracking System (ITS)

The detector system closest to the beam pipe is the ITS [39]. It extends from 3.9 to 43 cm in radial direction and covers with its six cylindrical layers of silicon detectors a pseudorapidity range of $|\eta| < 0.9$ which is equal to ±45° relative to the interaction plane. This allows the ITS to locate vertices within $z = \pm 60$ mm of the nominal interaction point with a precision of more than 100 μm. Furthermore, the ITS was designed to handle the large charged multiplicities in heavy ion collisions of up to $\mathrm{d}N_{\mathrm{ch}}/\mathrm{d}y \approx 8000$. The layers of the detector are made of different silicon detectors: two Silicon Pixel Detectors (SPD), two Silicon Strip Detectors (SSD) and two Silicon Drift Detectors (SDD) [43]. Besides vertex finding, the ITS is also capable of particle identification for $p_{\mathrm{T}} < 200$ MeV/c particles, which would not reach the outer detectors. Due to its good vertex resolution, the ITS is also able to remove so called in-bunch pileup events. Those events occur when there are multiple collisions during a single bunch-crossing and the tracks in the detector from the different vertices overlap. The in-bunch pileup correction removes the tracks that do not belong to the selected primary vertex. In addition, the ITS is used to improve the momentum and angular resolution of the TPC as it can reconstruct particles that ended up in dead areas of the TPC.

3.2.3 Time Projection Chamber (TPC)

The TPC [44] as shown in Figure 3.3 is the main central barrel detector for tracking of charged particles and particle identification. It is positioned between the ITS and the TRD as seen in Figure 3.2. The detector is designed to be able to handle high multiplicity heavy-ion events with a maximum number of charged particles per rapidity unit of $\mathrm{d}N_{\mathrm{ch}}/\mathrm{d}y \approx 8000$. The coverage of the TPC is $|\eta| < 0.9$ in pseudorapidity and the full 2π range in azimuth. For this the cylindrical drift chamber extends 2.5 m in beam direction on each side of the interaction point. The TPC field cage is filled with a drift gas that is a mixture of Ne-CO$_2$-N$_2$ (85.7-9.5-4.8%) [44, 45]. This mixture was kept until the end of 2010 when the nitrogen was removed and the remaining drift gas was set to be a mixture of 90% Ne and 10% CO$_2$. The drift chamber itself is divided by the central electrode at $\eta = 0$ and $z = 0$ and the readout pads are located at the end plates of the barrel on both, the A and C side. By applying a high voltage of 100 kV to the central electrode, the electric field towards the endplates results in drift times of 92 μs for electrons from the ionization of the TPC gas mixture.

Located at the end plates are the readout pads which are composed of multi-wire proportional chambers and segmented into 18 sectors in azimuth with each consisting of two chambers in radial direction. Each chamber is made of several pads whose size is optimized to deal with the expected track density at their radial position. In order to reconstruct the charged particle tracks in the TPC, the hit position information of the pads and the drift time given by the T0 detector are combined to get three dimensional track points. The transverse momentum can then be calculated from the track curvature. The TPC can reconstruct primary tracks with 100 MeV/$c < p_{\mathrm{T}} <$ 100 GeV/c. The minimum is given by the track curvature in the magnetic field as well as the probability to reach the TPC in the first place with such low momentum. In addition, a primary track can only be reconstructed if the particle traverses through at least one third of the TPC in radial direction. Secondary tracks, however, can be reconstructed down to 50 MeV/c which is

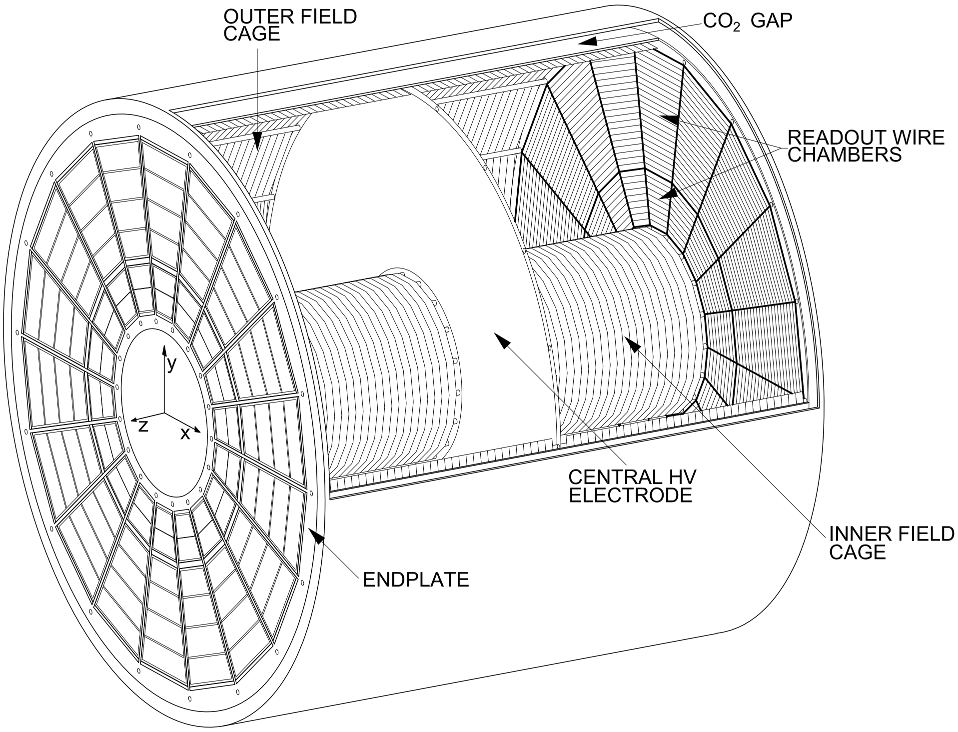

Figure 3.3: Overview of the TPC field cage including both endplates and the central electrode [44].

the accuracy limit of the tracking algorithm.
Besides tracking, the TPC is also used for particle identification (PID) by employing the energy loss measurements in the drift gas. The energy loss per path length for elastic scattering is described by the Bethe-Bloch-formula and is used for the calibration of the energy loss signal in the TPC. The TPC is able to resolve the $\mathrm{d}E/\mathrm{d}x$ signal from tracks with 160 clusters with a resolution of about 5% [44]. The PID will be important in Section 5.3 where we will cut on the energy loss signal of electrons and pions.

3.3 The Software Framework

The ALICE experiment and all of its detector systems generate massive amounts of data during operation. In order to deal with the data a powerful software framework is required. For ALICE this is done by using the two ROOT [46] based packages: AliRoot [47] and AliPhysics [48]. The whole framework is under constant development to improve data reconstruction, simulations and general performance. The coding in this framework is based on the C++ interpreter Clang [49], but also allows for python based software.
Raw data is processed using the AliRoot package, which can handle the detector data reconstruction as well as the production of Monte Carlo (MC) simulations using generators like PYTHIA [50–52] or PHOJET [53]. They can be used to create primary particles including their full kinematic information as well as their origins or decays. The particles are then introduced to a full detector simulation using GEANT [54, 55]. The analysis of detector data and Monte Carlo simulations is then done using the AliPhysics package which in the end allows to correct detector effects by combining data with Monte Carlo information.

4 Data Sets and Quality Assurance

This chapter introduces the data samples and their corresponding Monte Carlo simulations that are used for the analysis. The different data sets consist of proton-proton (pp) collision data from the center-of-mass energies $\sqrt{s} = 0.9$, 7 and 8 TeV [56]. At first, the data samples are presented which is then followed by the description of the simulations used for the corrections of the data samples. This is followed by the description of the event selection for this analysis. In the last part of this chapter, the quality of data and its agreement with the simulations is shown in the quality assurance for each data set.

4.1 Analysis Data Samples

After the first data takings from proton-proton collisions in ALICE in November of 2009 there have been recordings of collisions from six different center-of-mass energies ($\sqrt{s} =$ 0.9, 2.76, 5, 7, 8 and 13 TeV). In addition, ALICE also took data of Pb-Pb collisions at $\sqrt{s_{\mathrm{NN}}} = 2.76$ and 5.02 TeV as well as pPb collisions at $\sqrt{s_{\mathrm{NN}}} = 5.02$ TeV [56].
This analysis will focus on minimum bias triggered pp collision data from three different center-of-mass energies. One part consists of $\sqrt{s} = 0.9$ and 7 TeV pp collisions that were recorded in 2010 with the ALICE detector. This set is split into the periods LHC10[b-f] where each period is approximately one month of data taking and is subdivided into multiple runs. As part of the LHC10c period several runs at 900 GeV were recorded, whereas the remaining periods are purely recorded at $\sqrt{s} = 7$ TeV. For this data set, the fourth reconstruction pass (pass4) is used, which provides one additional period compared to pass2 and a better overall calibration of the data. The second part of the data set is from pp collisions at $\sqrt{s} = 8$ TeV recorded in 2012. The $\sqrt{s} = 8$ TeV periods are called LHC12[a-i] with the exception of LHC12g which was excluded due to very low overall statistics and multiple offline TPC readout pads during data-taking. From this data set, the second reconstruction pass (pass2) is used. In this pass, the period LHC12e was not reconstructed and is therefore also excluded.

4.2 Monte Carlo Simulations

The spectra from the data will require several correction. The correction factors which will be applied to the data are obtained from the Monte Carlo event generators which are used as input for a full detector simulation. Specifically tuned simulations are made for each data set. For the $\sqrt{s} = 0.9$ and 7 TeV periods, a Pythia 6.4 [50] generator is used, whereas for the $\sqrt{s} = 8$ TeV periods the two generators Pythia 8 [51, 52] and Phojet [53, 57] are taken.

Pythia

In this analysis and in ALICE in general two different Pythia versions are used. Pythia 6.4 is written in Fortran 77 and is less user friendly than Pythia 8 which is written in C++. The Pythia event generator uses Leading Order (LO) QCD matrix elements with the initial and final state parton showers to generate hard parton-parton interactions. In addition diffractive processes based on the Regge Field Theory are used to better reproduce the data [58]. Pythia can be used to generate high-energy events from collisions between elementary particles such as

e^+, e^-, p and $\overline{p}$ in every possible combination as well as string fragmentation and decay. As the QCD calculation doesn't hold for low p_T of the partons from hard interactions, a lower cut-off with $p_T > 2$ GeV is used to make a connection between low and high momentum processes. The LUND String Model is the basis for the hadronization simulations and for the decays, the decay properties from [28] are used and the hadrons are decayed according to the decay table.

Phojet

The Phojet Monte Carlo event generator is based on the two-component Dual Parton Model (DPM) [59] and includes soft hadronic processes, which are described by the supercritical Pomeron, and hard processes, which are described by pertubative constituent scattering. This allows the model to describe hadron-hadron, photon-hadron and photon-photon interactions at high energies [57]. A p_T cutoff at ≥ 3 GeV is made for the calculation of the hard processes while the soft interaction uses a model of multiple strings that are stretched between the proton and the resolved hadronic state of the photon. The characteristic features of this model are multiple soft and hard interactions [60]. The multiplicities of those interactions are calculated using a unitarization scheme [61] which was tuned to make the sum of the hard and soft cross sections nearly independent of the p_T cutoff.

In order to expose the generated particles to the detector responses, they are put into a full detector simulation using GEANT3 [54]. This detector simulation is anchored to the state of the detector during data taking and is optimized on a runwise basis. Interactions with the detector material as well as the response of each detector system are simulated and allow for a data-like analysis of the simulated events while still holding the Monte Carlo information. Therefore the simulations can be used to correct the data. However, it is important to check the agreement between the simulated events and the real events, which is done in Section 4.4 during the data set quality assurance.
The Monte Carlo productions that are anchored to the $\sqrt{s} = 7$ TeV data are LHC14j4[b-f] which are using the Pythia 6 event generator. For the $\sqrt{s} = 8$ TeV periods, the corresponding Monte Carlo productions are LHC15h1[a1-i] and LHC15h2[a-i] which are Pythia 8 or Phojet based respectively.

4.3 Event Selection

In this analysis two different minimum bias triggers are used depending on the center-of-mass energy of the data set. For the $\sqrt{s} = 900$ GeV and 7 TeV analyses the minimum bias trigger is the V0OR (kINT1) trigger which allows for invariant cross-sections of $47.78^{+2.39}_{-1.86}$ mb and 62.22 ± 2.18 mb respectively [62]. The $\sqrt{s} = 8$ TeV data set employs the V0AND (kINT7) minimum bias trigger with which an invariant cross-section of 55.75 ± 1.25 mb can be observed [63]. The minimum bias triggers are based on information provided by the V0 detector system which was introduced in the last chapter. For the lower interaction rate periods LHC10[b-f] the required minimum bias trigger condition was set to a hit in either of the V0 detectors on A or C side. It is therefore called the V0OR trigger. However, for the high interaction rate periods of the $\sqrt{s} = 8$ TeV data takings, this condition was set to coincidence of both V0 sides V0A and V0C. This trigger is therefore called V0AND and aims to remove unwanted background and provides a more stable trigger condition

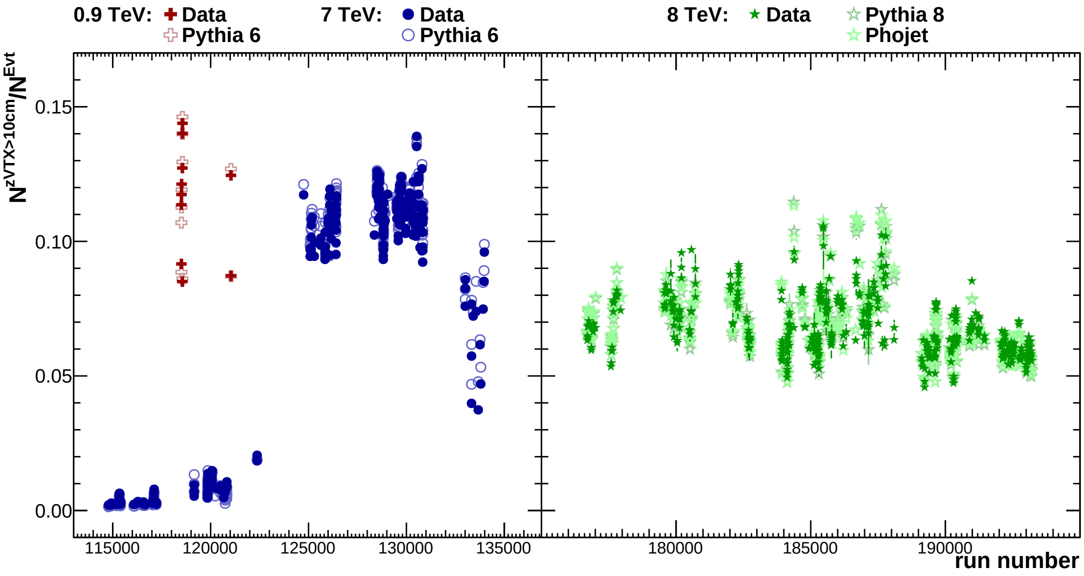

Figure 4.1: Fraction of events rejected due to a vertex position outside $Z_{\mathrm{vtx}} = \pm 10$ cm with respect to the total number of collected minimum bias events in the respective run.

in a high luminosity environment.

In addition to passing the minimum bias trigger requirements the events also have to fulfill the event selection criteria. Events are rejected which are not of physics type (e.g. calibration events). Additionally, events are only used if their reconstructed primary vertex is within $|z_{\mathrm{vtx}}| < 10$ cm to the center of the ALICE central barrel. This vertex can be reconstructed using either global tracks or only Silicon Pixel Detector (SPD) tracklets as long as they have at least one contributing track or tracklet to the vertex [64]. In Table 2 the statistics of the different data sets and their corresponding Monte Carlo simulations is shown as well as the fraction of events lost due to the different vertex requirements. Figure 4.1 shows the run dependence of this fraction for all data sets and their corresponding Monte Carlo simulations. The normalization of the spectra in this thesis is done with the following number of events that takes into account the events lost due to the vertex requirements and where N_{MB} stands for the number of minimum bias triggered events using either V0AND or V0OR. The values for each data set are also listed in Table 2.

$$N_{\mathrm{norm,evt}} = N_{\mathrm{MB,Vtx},|z_{\mathrm{Vtx}}|<10\mathrm{cm}} + \frac{N_{\mathrm{MB,Vtx},|z_{\mathrm{vtx}}|<10\mathrm{cm}}}{N_{\mathrm{MB,Vtx},|z_{\mathrm{vtx}}|<10\ \mathrm{cm}} + N_{\mathrm{MB,Vtx},|z_{\mathrm{vtx}}|>10\mathrm{cm}}} N_{\mathrm{MB,no\ Vtx}} \tag{9}$$

The event selection also contains an in-bunch pileup rejection based on SPD tracklets. This correction has become more and more important due to the steadily increasing instantaneous luminosity delivered by the LHC. Despite ALICE reducing the interaction rate by displacing both beams or using main-satellite beam collisions, this rejection is of growing importance. In addition, the filling schemes of the LHC contain an increasing number of bunches with less spacing between bunches. The fraction of events rejected due to in-bunch pileup can be seen in Figure 4.2 for all data sets. As in Monte Carlo only single collisions are simulated they do not contain in-bunch pileup and their fraction in Figure 4.2 as well as in Table 2 is zero.

Data Set	Min. Bias. Events (MB) N_{MB}	Events for normalization N_{norm}	$\frac{\mathrm{MB+Vtx+}\lvert z_{\mathrm{vtx}}\rvert<10}{\mathrm{MB}}$	$\frac{\mathrm{MB+Vtx+}\lvert z_{\mathrm{vtx}}\rvert>10}{\mathrm{MB}}$	$\frac{\mathrm{MB+\ no\ Vtx}}{\mathrm{MB}}$	$\frac{\mathrm{MB+Pile\text{-}up}}{\mathrm{MB}}$
			900 GeV			
Data pass4						
LHC10c_900GeV	6.65e06	5.82e06	0.806	0.112	0.079	0.003
MC Pythia 6						
LHC14j4c_900GeV	6.74e06	5.91e06	0.800	0.111	0.088	0.000
			7 TeV			
Data pass4						
LHC10[b-f]	4.16e08	4.64e08	0.819	0.082	0.087	0.013
LHC10b	2.71e07	2.74e07	0.900	0.004	0.092	0.003
LHC10c	7.39e07	7.59e07	0.888	0.009	0.087	0.016
LHC10d	1.53e08	1.75e08	0.795	0.103	0.089	0.013
LHC10e	1.27e08	1.47e08	0.795	0.113	0.081	0.011
LHC10f	3.53e07	3.89e07	0.822	0.068	0.091	0.019
MC Pythia 6						
LHC14j4[b-f]	4.20e08	4.64e08	0.820	0.085	0.094	0.000
LHC14j4b	2.78e07	2.79e07	0.905	0.004	0.091	0.000
LHC14j4c	7.22e07	7.29e07	0.898	0.008	0.093	0.000
LHC14j4d	1.55e08	1.76e08	0.797	0.107	0.096	0.000
LHC14j4e	1.29e08	1.48e08	0.790	0.115	0.094	0.000
LHC14j4f	3.66e07	3.98e07	0.832	0.073	0.094	0.000
			8 TeV			
Data pass2						
LHC12[a-i]	1.31e08	1.21e08	0.908	0.067	0.014	0.011
LHC12a	1.52e07	1.40e07	0.901	0.067	0.019	0.012
LHC12b	8.81e06	8.11e06	0.908	0.070	0.013	0.009
LHC12c	1.96e07	1.79e07	0.895	0.079	0.018	0.008
LHC12d	3.51e07	3.24e07	0.910	0.066	0.014	0.011
LHC12f	9.60e06	8.81e06	0.902	0.075	0.018	0.006
LHC12h	3.99e07	3.70e07	0.917	0.060	0.009	0.013
LHC12i	2.89e06	2.66e06	0.916	0.057	0.004	0.023
MC Pythia8						
LHC15h1[a1-i]	2.47e08	2.30e08	0.919	0.069	0.012	0.000
LHC15h1a1	3.45e07	3.19e07	0.916	0.072	0.012	0.000
LHC15h1b	3.22e07	2.98e07	0.914	0.073	0.012	0.000
LHC15h1c	3.31e07	3.04e07	0.909	0.078	0.012	0.000
LHC15h1d	5.58e07	5.21e07	0.922	0.065	0.012	0.000
LHC15h1f	2.07e07	1.90e07	0.906	0.081	0.012	0.000
LHC15h1h	6.66e07	6.25e07	0.928	0.059	0.012	0.000
LHC15h1i	4.64e06	4.38e06	0.931	0.056	0.012	0.000
MC Phojet						
LHC15h2[a-i]	2.60e08	2.42e08	0.921	0.069	0.010	0.000
LHC15h2a	3.61e07	3.35e07	0.917	0.072	0.010	0.000
LHC15h2b	3.41e07	3.16e07	0.916	0.074	0.010	0.000
LHC15h2c	3.48e07	3.21e07	0.911	0.079	0.010	0.000
LHC15h2d	5.85e07	5.46e07	0.924	0.066	0.010	0.000
LHC15h2f	2.13e07	1.95e07	0.907	0.082	0.010	0.000
LHC15h2h	6.97e07	6.55e07	0.930	0.060	0.010	0.000
LHC15h2i	4.83e06	4.56e06	0.933	0.056	0.010	0.000

Table 2: Number of events used for normalization in the analysis for each period. In addition the number of events of the respective Minimum Bias trigger and the fractions for $\frac{\mathrm{MB+Vtx+}\lvert z_{vtx}\rvert<10}{\mathrm{MB}}$, $\frac{\mathrm{MB+Vtx+}\lvert z_{vtx}\rvert>10}{\mathrm{MB}}$, $\frac{\mathrm{MB+\ no\ Vtx}}{\mathrm{MB}}$ and $\frac{\mathrm{MB+Pile\text{-}up}}{\mathrm{MB}}$ for each period used in the analyis.

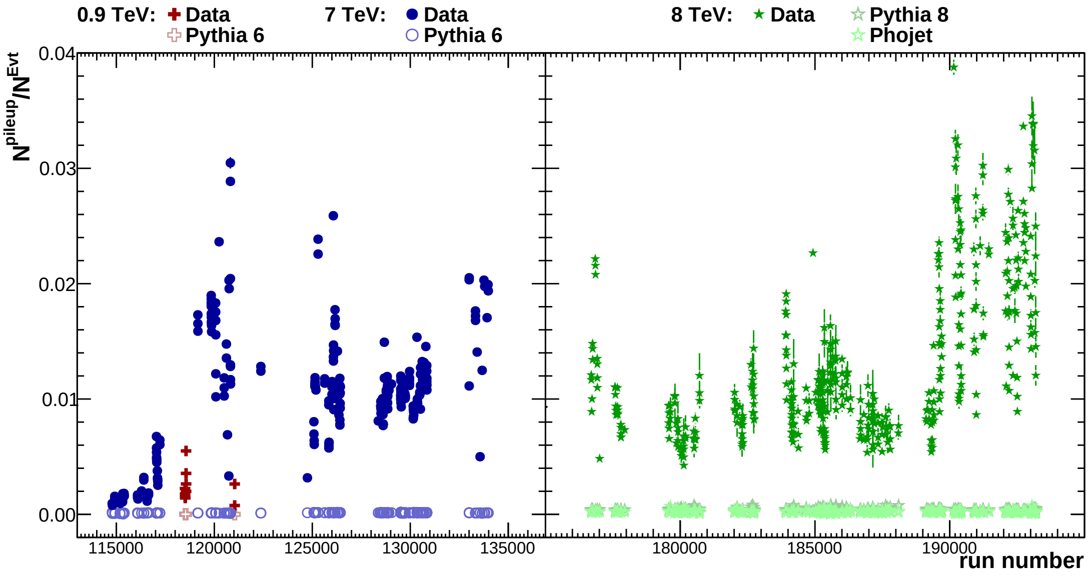

Figure 4.2: Fraction of events rejected due to in-bunch SPD pileup with respect to the total number of collected minimum bias events in the respective run.

4.4 Quality Assurance of the Data Sets

The Quality Assurance (QA) of the data sets that is discussed in this section compares important quantities between data and their corresponding Monte Carlo simulations on a runwise and complete data set basis. The runwise comparison is necessary as it is important to check that the MC describes the data detector performance in each run and follows possible changes in performance. Only if data and Monte Carlo agree we are able to use the MC to reliably correct the measured spectra.

As a result of the QA several runs are excluded from the analysis as they show a disagreement between data and MC or as they do not meet general quality requirements for the analysis. An important quantity for the PCM analysis is the fraction of photon candidates per event as seen in Figure 4.5 which should not show strong outliers. This quantity is also correlated to the amount of SPD rejected in-bunch pileup as seen in Figure 4.2. There, the increasing amount of rejected pileup events in the $\sqrt{s} = 8$ TeV periods can be observed. The last two periods LHC12h and LHC12i of that data set consist of very high interaction rate runs which resulted in large amounts of in-bunch pileup.

For the QA also the mass peak positions of the neutral pion integrated over p_{T} is compared between data and MC and should be consistent. This quantity is an indicator for the quality of the calibration of the Monte Carlo simulations. The peak positions on a runwise basis can be seen in Figure 4.3. In addition, the number of charged particle tracks in the TPC is compared between data and simulation to check the TPC calibration. The quantity $\overline{N}_{\text{good tracks}}$ is shown in Figure 4.4.

The rejection of runs from the data sample due to the different quality requirements results in approximately 5% of the $\sqrt{s} = 7$ TeV and 17% of the $\sqrt{s} = 8$ TeV dataset being removed from the sample. The larger percentage in the $\sqrt{s} = 8$ TeV dataset is a result of the worse TPC and ITS performance during data taking compared to the $\sqrt{s} = 7$ TeV data acquisition periods. The list of runs used for the analysis are shown in Table 14 and Table 15 and the statistics of each dataset after the QA is listed in Table 2.

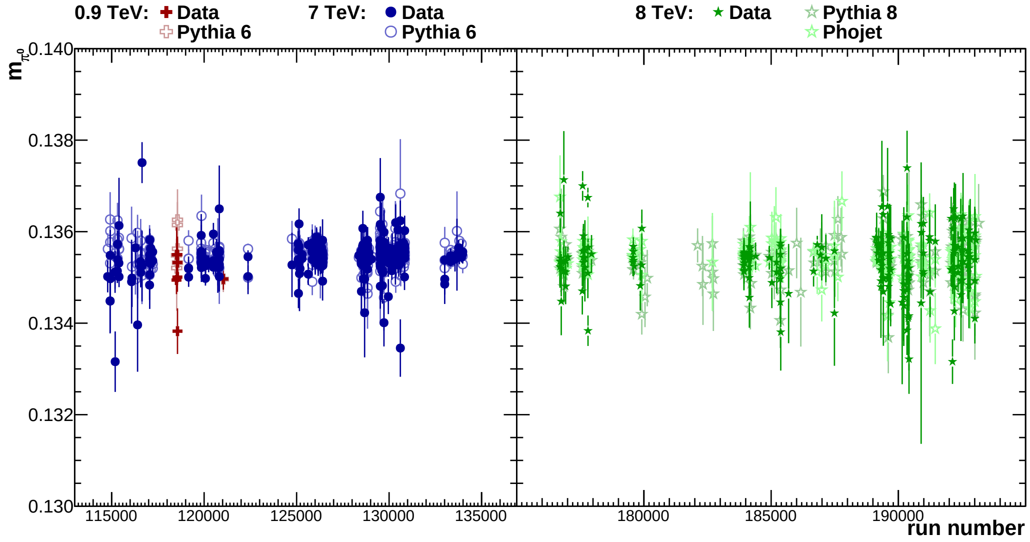

Figure 4.3: Neutral pion peak positions integrated over transverse momentum.

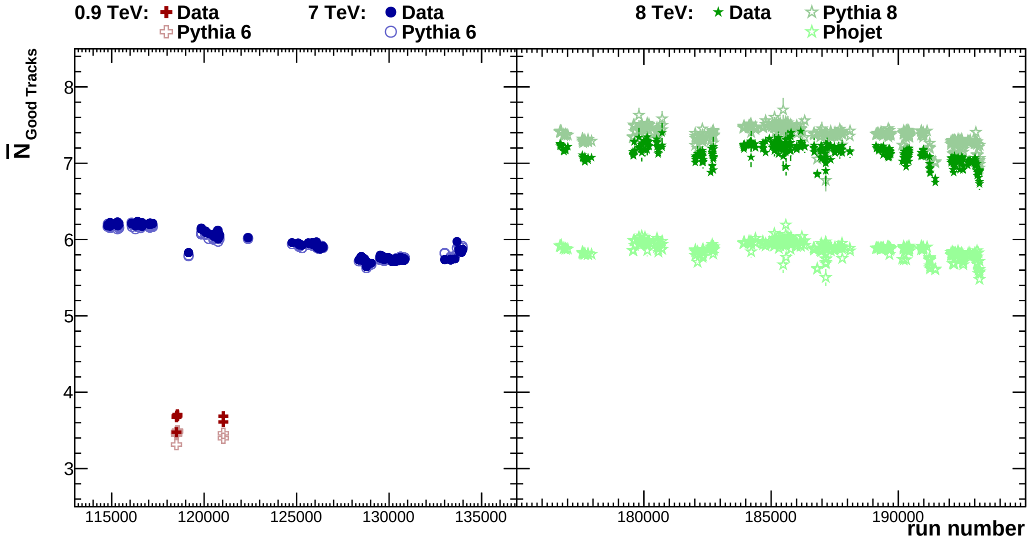

Figure 4.4: Mean number of good charged particle tracks in the TPC.

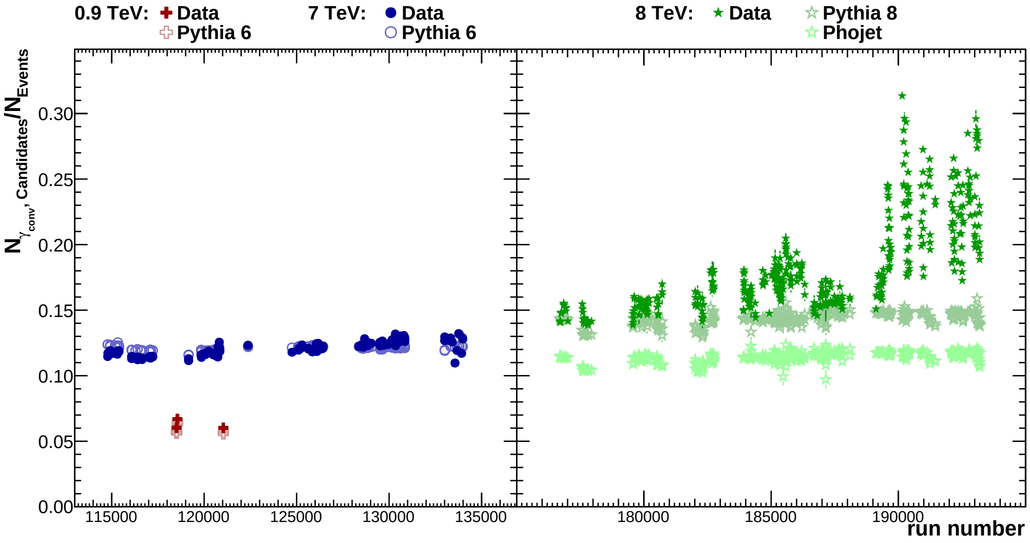

Figure 4.5: Fraction of photon candidates normalized to the number of events, which fulfill the event selection criteria.

5 Data Analysis with the Photon Conversion Method

The Photon Conversion Method (PCM) will be explained in this chapter. For this, the photon reconstruction using this method is illustrated as well as the cuts that are applied on several quantities which are important for this reconstruction method. The general idea of PCM is the measurement of neutral mesons via their two photon decay channel. This is realized by reconstructing the photons from their conversion products, meaning the e^+e^--pairs. For this reconstruction, information provided by the Time Projection Chamber and the Inner Tracking System is used.

5.1 Photon Reconstruction and Selection

In order to reconstruct the converted photons from their conversion products a secondary vertex finder is used. This vertex finder uses secondary tracks, which are tracks that do not originate from the primary vertex, to reconstruct the V^{0}s. A sketch of this reconstruction method is shown on the left side in Figure 5.1.

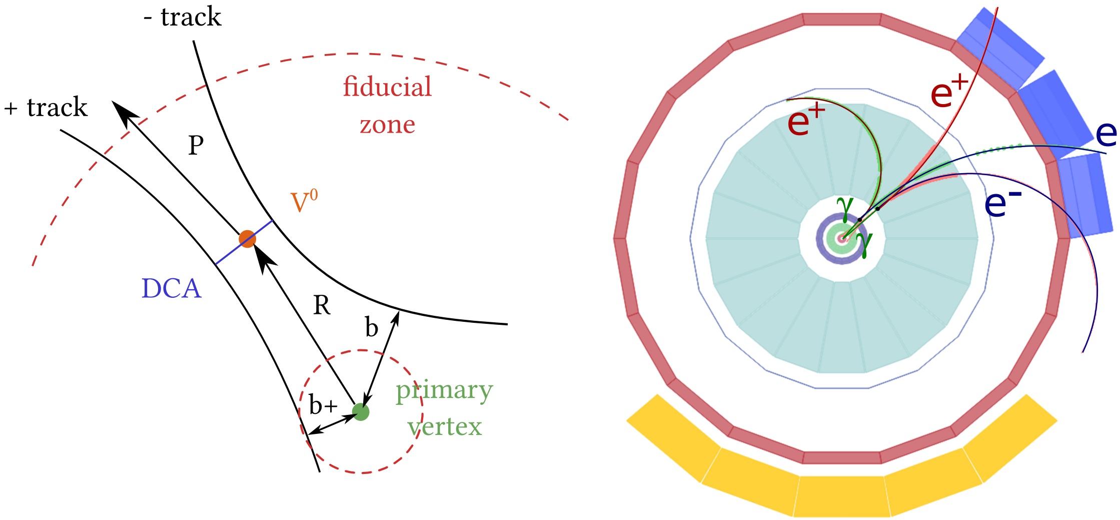

Figure 5.1: Left: Reconstruction sketch of a secondary vertex from two charged tracks. Derived from [39]. **Right:** Reconstructed π^0 candidate from $\sqrt{s} = 900$ GeV data takings in 2009. The π^0 candidate in this sketch is reconstructed from two photon conversions.

For the reconstruction, first two oppositely charged tracks are selected and their impact parameters (b, b+) with respect to the primary vertex are calculated. Tracks with too small impact parameters are discarded as they might rather originate from the primary vertex then from a secondary vertex. If two tracks are found with more than the minimum impact parameters their distance of closest approach (DCA) is calculated. Depending on the distance to the primary vertex R and its resolution the DCA value is required to be small and at most 1 cm or otherwise the track pair will be rejected. From the accepted track pairs the V^{0}s are formed where the secondary vertex is set to be the point of closest approach of the two charged tracks. The dotted lines in Figure 5.1 indicate the fiducial zone in which the secondary vertex is required to be reconstructed. This zone stretches from 5 cm to 180 cm in radial direction from the primary vertex. Furthermore, the V^0 momentum vector is calculated by extrapolation of the momenta of both tracks to the DCA and calculating their sum in this point. If this momentum vector does not point towards the primary vertex the V^0 candidate is discarded. This is done by checking the cosine of the angle between the V^0 momentum vector P and the vector between secondary and primary vertex R and requiring a value of less than 0.85 for it. The vectors are also indicated in Figure 5.1. The following sections will introduce the selection criteria for photons used in the neutral meson and direct photon analyses beginning with the track and V^0 selection, then the electron identification cuts and finally the photon selection cuts.

5.2 Track and V^0 Selection

This section introduces the track and V^0 selection cuts used in the analyses. An overview of the cuts is shown in Table 3. For this analysis, the standard V^0 finder is chosen to be the on-the-fly V^0 finder as the strict cuts implied by the offline V^0 finder are not required. For each V^0 candidate that is then selected several requirements are imposed on the secondary tracks. The tracks have to show no kink-topology, fulfill the TPC refit condition and must have opposite charges. In addition, a minimum momentum cut on the secondary particles is applied with $p_{\mathrm{T}} < 50$ MeV/c. To guarantee a certain track quality it is necessary to pass a cut of more than 60% of all theoretically possible TPC clusters which also accounts for inclination and origin of the tracks.

Track and V^0 cuts	
V^0 finder	On-the fly
minimum track p_{T} cut	$p_{\mathrm{T,track}} > 0.05$ GeV/c
Cut on $\frac{N_{\mathrm{clusterTPC}}}{N_{\mathrm{findableclusters}}}$	$> 60\%$
Cut on R_{conv}	5 cm $< R_{\mathrm{conv}} <$ 180 cm
Cut on Z_{conv}	$\lvert Z_{\mathrm{conv}}\rvert < 240$ cm
η cut	$\lvert\eta\rvert < 0.9$

Table 3: Standard cuts for the track and V^0 selection used in the neutral meson and direct photon analyses.

Furthermore, a cut on the V^0 pseudorapidity η is used. The pseudorapidity is interpreted as the angle between the beam-axis and the orientation of the 3-momentum vector of the particle in the ZR-plane. Not taking into account the starting point of the track, several photon candidates would pass this cut although being outside of the geometrical acceptance of the detector. To account for this, a line-cut is used which represents a cut on the geometrical η distribution of the conversion points with the nominal center of the detector as origin. By using the following conditions with $Z_0 = 7$ cm and R_{conv} and Z_{conv} being determined with respect to the center of the detector:

$$S_{\mathrm{ZR}} = \tan(2 \times \arctan(\exp(-\eta_{\mathrm{cut}}))) \tag{10}$$

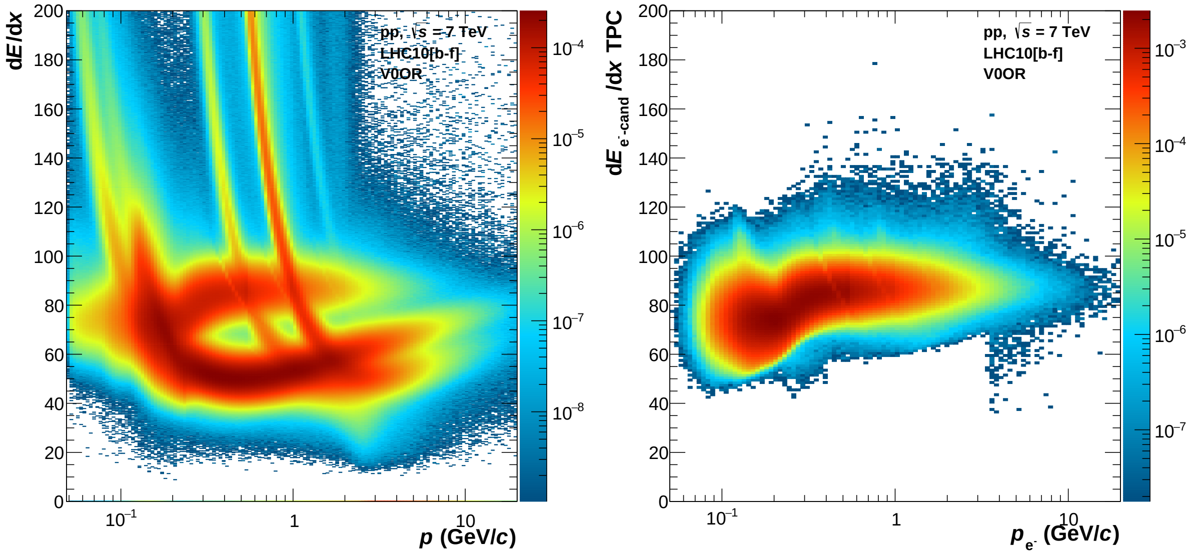

Figure 5.2: The TPC dE/dx plot for the V^0 daughters before (**left**) and after (**right**) all electron selection cuts.

$$R_{\text{conv}} > |Z_{\text{conv}}| \times S_{\text{ZR}} - Z_0 \tag{11}$$

By cutting on R_{conv} and Z_{conv} it is ensured that the secondary track reconstruction is limited to the TPC barrel. They are therefore limited to values of $Z_{\text{conv}} < 240$ cm and $R_{\text{conv}} < 180$ cm. In addition, a cut on the conversion radius of $R_{\text{conv}} > 5$ cm is applied to reject contaminations coming from neutral meson Dalitz decays.

5.3 Electron Identification Cuts

The application of electron identification cuts is necessary to obtain only photons from conversions in the remaining V^0 sample. For this, electron selection and pion rejection cuts are applied. The cuts are applied on the energy loss signal dE/dx distributions measured in the TPC. Besides using the TPC, ALICE can also identify electrons via dE/dx measurements in the ITS, with time-of-flight measurements using TOF, with transition radiation or dE/dx in the TRD or using energy deposits in the calorimeters.

The dE/dx signal in the TPC was chosen as the other techniques would show a significant loss in efficiency. The cuts that are used for the electron PID have been optimized to provide as little contamination as possible while still providing a large efficiency. In Table 4 the cuts for the electron identification are shown.

Particle identification cuts	
nσ_e TPC dE/dx	-3 < nσ_e < 5
nσ_π TPC dE/dx	0.3 GeV/c < p < 3.5 GeV/c: n$\sigma_\pi > 1$
	$p > 3.5$ GeV/c: n$\sigma_\pi > -10$

Table 4: Standard cuts for the electron identification in the different analyses. The ranges given in the table show the part of the distribution that is kept.

The cuts are applied around the theoretical energy loss line for electrons and pions in terms of standard deviations (nσ) from those values. For the analysis rather tight cuts are applied to minimize the contamination from pions and generating a clean electron sample. The most important cut is the electron nσ_e cut which removes everything in terms of standard deviations from the theoretical energy loss expectation outside of 5 σ_e above and 3 σ_e below the electron hypothesis line.
An additional cut on the pion nσ_π is used to further remove pions from the sample. This cut is set to different values in two momentum regions. For the low momentum region from the minimum momentum of the measurement up to 3.5 GeV/c everything above 1 σ_π above the pion line is kept whereas above 3.5 GeV/c in transverse momentum nearly everything is kept due to the -10 σ_π cut. The influence of these cuts on the dE/dx distributions can be seen in Figure 5.2 for the $\sqrt{s} = 7$ TeV data. Additional nσ dE/dx distributions for the other data sets as well as Monte Carlo simulations are shown in the appendix in Figure C.1.

5.4 Photon Selection

The photon selection step provides an additional level of purity to the photon sample. The sample itself is mainly made up of electron-positron conversion pairs since the two previous particle selection steps. Further improvements are now made by restricting the photon conversion topology and the cosine of the pointing angle as described in Section 5.1. The photon selection cuts used in the analyses are listed in Table 5.

Photon cuts	
χ^2_γ/ndf	2D triangular cut with χ^2_γ/ndf < 30 and $\Psi_{\mathrm{Pair}} < 0.1$
q_{T}	2D elliptic cut with $q_T < 0.05$ GeV/c and $\alpha_\gamma = 0.95$
cos(P.A.)	> 0.85

Table 5: Photon selection cut that are applied in the analyses.

In order to exclude K^0_S, Λ and $\overline{\Lambda}$ from the V^0 sample an elliptic cut in the Armenteros-Podolanski [65] plot in $q_{\mathrm{T}} = p \times \sin\theta_{\mathrm{mother-daugther}}$ and α is applied. This plot, shown in Figure 5.3 for the $\sqrt{s} = 7$ TeV dataset, provides the projection of the momentum of the daughter particle with respect to the mother particle in the transverse direction q_{T} versus the longitudinal momentum asymmetry $\alpha = (p^+_{\mathrm{L}} - p^-_{\mathrm{L}})/(p^+_{\mathrm{L}} + p^-_{\mathrm{L}})$. The q_{T} value of real photons is close to zero as the daughter particles fly, in the laboratory frame, in the same direction as the photon and therefore under a small opening angle. The symmetry in α in Figure 5.3 is given due to the identical mass of the decay products. The heavier particles K^0_S, Λ and $\overline{\Lambda}$ have a larger opening angle and therefore also have a larger q_{T}. The elliptical cut in $q_T < 0.05$ GeV/c and $\alpha_\gamma = 0.95$ removes the unwanted K^0_S, Λ and $\overline{\Lambda}$ contamination from the V^0 sample as seen in the figure.

In addition to the q_{T} and α cuts, a two dimensional cut in χ^2/ndf and Ψ_{Pair} is used. The χ^2/ndf cut can be applied because the AliRoot KFParticle package [66] is used for the photon reconstruction and allows to set constraints on the construction and quality of the photons. The cut itself is applied on a fit of a generic particle decay model based on the

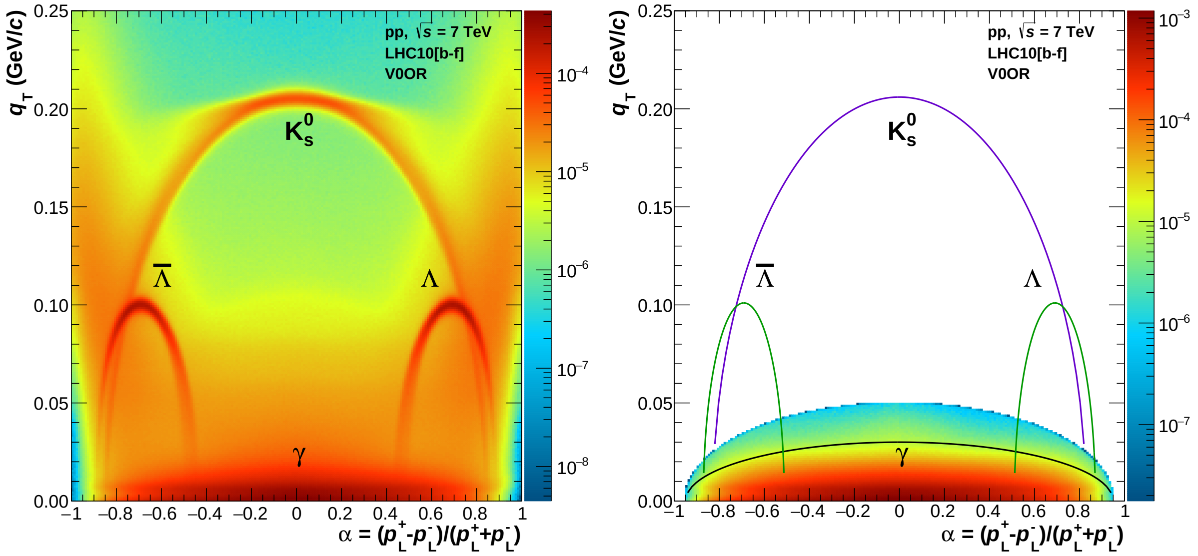

Figure 5.3: The Armenteros Podolanski plot for the V^0's before (**left**) and after (**right**) all photon selection cuts for the $\sqrt{s} = 7$ TeV dataset.

Kalman filter method to reconstruct a V^0. In this method, it is assumed that the particle has no mass and comes from the primary vertex. The Ψ_{Pair} cut is based on the opening angle of the electron-positron pair from a photon conversion and in addition employs the fact that the magnetic field only has a small effect on the track bending. Visualized in Figure 5.4 is the construction of the Ψ_{Pair} angle. In order to calculate Ψ_{Pair}, the tracks are first propagated to a radial distance of 50 cm from the conversion point. It is then calculated by the following formula:

$$\Psi_{\mathrm{pair}} = \arcsin\left(\frac{\Delta\theta}{\xi_{\mathrm{pair}}}\right), \tag{12}$$

where $\Delta\theta = \theta_{e^-} - \theta_{e^+}$ stands for the angle in the polar direction and ξ_{pair} is given by:

$$\xi_{\mathrm{pair}} = \arccos\left(\frac{\vec{p_{e^-}} \cdot \vec{p_{e^+}}}{|\vec{p_{e^-}}| \cdot |\vec{p_{e^+}}|}\right). \tag{13}$$

From this one can see that Ψ_{Pair} stands for the arcsine of the ratio between the angle difference of the two daughter tracks to the z-axis and the angle between the two propagated daughter tracks. While $\Delta\theta$ remains constant, the opening angle in the transverse plane increases due to the magnetic field. This allow the Ψ_{Pair} cut to suppress the remaining track combinations by forcing a limit to the ratio of the relative e^+e^- pair opening angle after creation to the opening angle at a radial distance of 50 cm from the conversion point [68]. In the analyses, Ψ_{Pair} is limited to a maximum value of 0.1 and χ^2/ndf to 30. The distribution of both values after the application of the cuts can be seen in Figure 5.4.

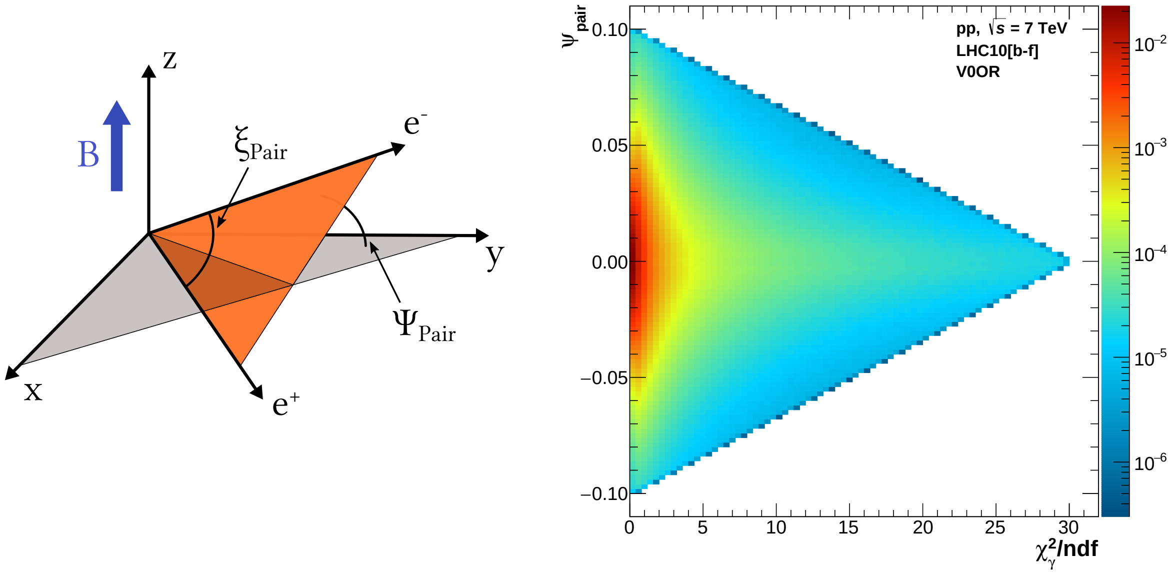

Figure 5.4: Left: Visualization of the Ψ_{Pair} angle as the angle between the plane of the electron and positron pair (orange) and the bending plane of the magnetic field (gray). Derived from [67]. **Right:** χ^2/ndf and Ψ_{Pair} plot after the two dimensional cut has been applied.

6 Neutral Meson Analysis

The neutral meson analysis in proton-proton collision at $\sqrt{s} = 0.9$, 7 and 8 TeV will be discussed in this chapter. The first section provides a general overview of the analysis method and the signal extraction. Afterwards, the spectrum corrections obtained from the Monte Carlo simulations are explained and the systematic uncertainties will be determined. The chapter is closed with the comparison of the fully corrected π^0 and η meson cross sections to other reconstruction methods as well as theory calculations.

6.1 Neutral Meson Reconstruction

The neutral mesons are reconstructed using the V^0 sample from Section 5.4 and combining the photons into pairs. The pairs, however, are not allowed to share tracks or to have an opening angle of less then 5 mrad and are otherwise discarded. The invariant mass of each pair can then be calculated with the following formula:

$$M_{\gamma\gamma} = \sqrt{2E_{\gamma_1}E_{\gamma_2}(1-\cos\theta_{12})}. \tag{14}$$

Here, the photon energies are given by $E_{\gamma_{1,2}}$ and the opening angle between the photons in the laboratory system is given by θ_{12}. By calculating the invariant mass of every possible photon pair the mass of the neutral mesons cannot be determined exactly. Instead the mesons appear as an excess in the invariant mass distributions around their respective nominal mass; $m_{\pi^0} = 134,976$ MeV/c^2 for the π^0 meson and $m_\eta = 547.862$ MeV/c^2 for the η meson [28]. This excess can be seen in the invariant mass distributions of the photon pairs close to the π^0 meson mass and close to the η meson mass in Figure 6.1. For the π^0 a clear peak is visible with very little underlying background whereas for the η meson an strong background below the peak can be seen. A large portion of the background in the invariant mass distributions comes from combinatorial background due to the combination of every possible photon pair. This background, however, can be subtracted very well using the Event Mixing method [69, 70] which can also be seen in the invariant mass plots indicated by the gray points. In order to reproduce the combinatorial background below the peaks, the Event Mixing method combines photons from different events. This removes any possible correlation between the photons. For each bin the same amount of photon sample statistics is used for this method to not induce additional uncertainties. The resulting distribution is then scaled to the right side of the peak and subtracted.

Data set	π^0	η
900 GeV	$0.4 < p_\mathrm{T} < 3.5$ GeV/c	$0.9 < p_\mathrm{T} < 3.0$ GeV/c
7 TeV	$0.3 < p_\mathrm{T} < 16.$ GeV/c	$0.4 < p_\mathrm{T} < 10.$ GeV/c
8 TeV	$0.3 < p_\mathrm{T} < 12.$ GeV/c	$0.4 < p_\mathrm{T} < 8.0$ GeV/c

Table 6: Neutral meson invariant mass extraction range in transverse momentum.

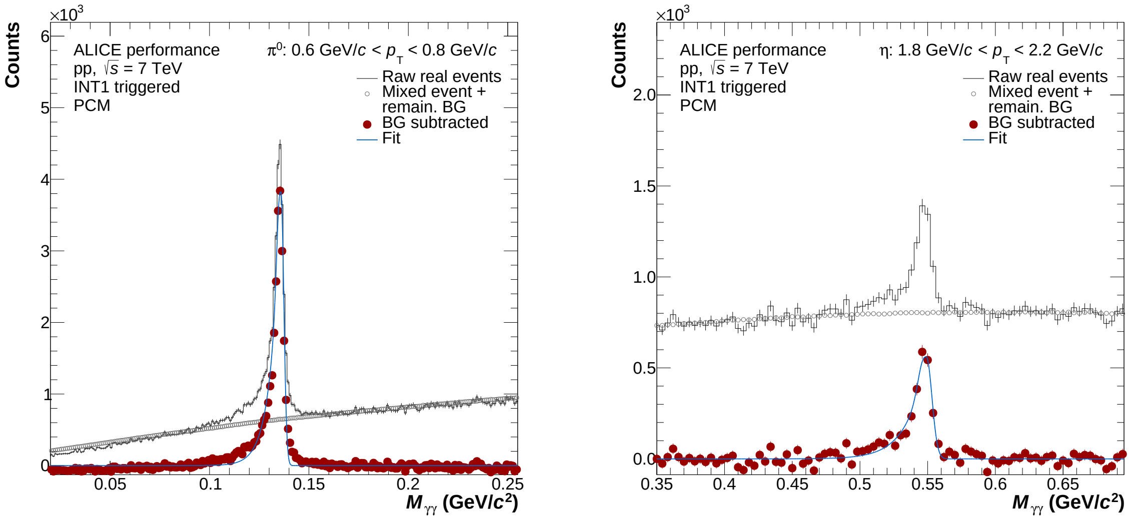

Figure 6.1: Neutral meson invariant mass distributions for example bins in the p_{T} range of 0.6 GeV/c to 0.8 GeV/c for the neutral pion and 1.8 GeV/c to 2.2 GeV/c for the η meson. The data including background is plotted in black and with background subtracted in red. The background parts coming from the event mixing and the linear part of the peak fit are combined and shown in gray points. In both plots, the fit to the background subtracted distribution is drawn in cyan.

6.1.1 Signal Extraction

The neutral meson signal extraction relies on the invariant mass distributions that have been calculated in the previous section. In addition, the distributions are calculated in several transverse momentum bins. The p_{T} range that has been achieved in each dataset for the π^0 and η mesons is shown in Table 6. In addition, the plots for each transverse momentum bin for π^0 and η mesons for each data set can be seen in the appendix in Figure C.2 for 900 GeV, Figure C.4 for 7 TeV and Figure C.6 for 8 TeV. For each invariant mass bin the calculation is done once for photons from the same event and afterwards for photons coming from two different events for the Event Mixing method as described in the last section. The scaling of the event mixing background can be done to the left or right side of the peak and should be done very close to the peak without going into the peak itself. The normalized background, done to the right side of the peak in this analysis, is then subtracted from the signal. Example bins for the π^0 and η mesons from the $\sqrt{s} = 7$ TeV dataset are shown in Figure 6.1 including the signal and the residual background.

The remaining signal is then fitted with a Gaussian function that is combined with an exponential low-energy tail on the left side of the peak to account for electron bremsstrahlung. An additional linear part is also added to the fit function to account for remaining background under the peak that could not be described by the combinatorial background. The fit function for the invariant mass peaks is given by:

$$y = A \cdot \left[G(M_{\gamma\gamma}) + \exp\left(\frac{M_{\gamma\gamma} - M_{\pi^0,\eta}}{\lambda} \right) (1 - G(M_{\gamma\gamma}))\theta(M_{\pi^0,\eta} - M_{\gamma\gamma}) \right] + B + C \cdot M_{\gamma\gamma} \quad (15)$$

$$\text{with } G = \exp\left[-0.5 \left(\frac{M_{\gamma\gamma} - M_{\pi^0,\eta}}{\sigma_{M_{\gamma\gamma}}} \right)^2 \right] \quad (16)$$

In this function, G represents a Gaussian function with the width σ, the amplitude A and the mean position $M_{\pi^0,\eta}$. This mean position can be identified with the reconstructed mass position of the neutral mesons. The exponential part for the bremsstrahlung tail is given by the parameter λ which is the inverse slope of the exponential function. The exponential is set to zero above $M_{\pi^0,\eta}$ with the Heaviside function $\theta(M_{\pi^0,\eta} - M_{\gamma\gamma})$. The linear part for the remaining background is described by B and C. In Figure 6.1 the mixed event combinatorial background is shown with the gray points which already includes the contribution from the linear part of the fit. The peak fit function consisting of the Gaussian and the exponential is shown with the cyan line.

The fit is then used to extract the invariant mass peak position and the full width at half maximum (FWHM) for both mesons in their transverse momentum bins. Both values for all data and Monte Carlo sets can be seen in Figure 6.2. This figure also shows the transverse momentum reach and performance of the PCM method with the statistics given in each dataset as well as the good agreement between data and Monte Carlo. As in this analysis no smearing of the Monte Carlo is used, a small difference in the FWHM between data and MC is visible for the $\sqrt{s} = 8$ TeV measurement. This originates from a different gas mixture in the TPC during the 2012 data takings where the N_2 was removed from the mix which resulted in a different multiple scattering behavior. In addition, during this data taking period there were more non-nominal operating ITS channels present compared to the 2010 data takings. Both effects contribute to a difference between data and Monte Carlo. However, this difference is negligible compared to the integration range of the peak for the yield extraction which is explained in the following.

The next step of the signal extraction is the meson yield extraction. This is done by integrating the background subtracted invariant mass distributions in each transverse momentum bin in a fixed mass range around the fitted meson mass $M_{\pi^0,\eta}$. From this bin-by-bin integration the linear part of the fit is subtracted to remove the remaining background. The integration range is the same for the three different center-of-mass energy measurements and is set for the neutral pion to $(M_{\pi^0} - 0.035 \text{ GeV}/c^{\,2}, M_{\pi^0} + 0.012 \text{ GeV}/c^{\,2})$ which corresponds to $(-11\langle n\sigma_\pi\rangle, 4\langle n\sigma_\pi\rangle)$ around the determined π^0 meson mass M_{π^0}. This asymmetric integration range incorporates the bremsstrahlung tail on the left side of the invariant mass distribution. The calculation of the π^0 meson raw yield is therefore given by:

$$N^{\pi^0}_{\text{raw}} = \int_{M_{\pi^0}-0.035\text{GeV/c}^2}^{M_{\pi^0}+0.012\text{GeV/c}^2} (N^{\gamma\gamma} - N^{\text{comb.BG}}) \mathrm{d}M_{\gamma\gamma} - \int_{M_{\pi^0}-0.035\text{GeV/c}^2}^{M_{\pi^0}+0.012\text{GeV/c}^2} (B + C \cdot M_{\gamma\gamma}) \mathrm{d}M_{\gamma\gamma} \quad (17)$$

The integration range for the η meson covers a larger invariant mass range due to the broader peak. The range is set to $(M_\eta - 0.048 \text{ GeV}/c^{\,2}, M_\eta + 0.022 \text{ GeV}/c^{\,2})$ which

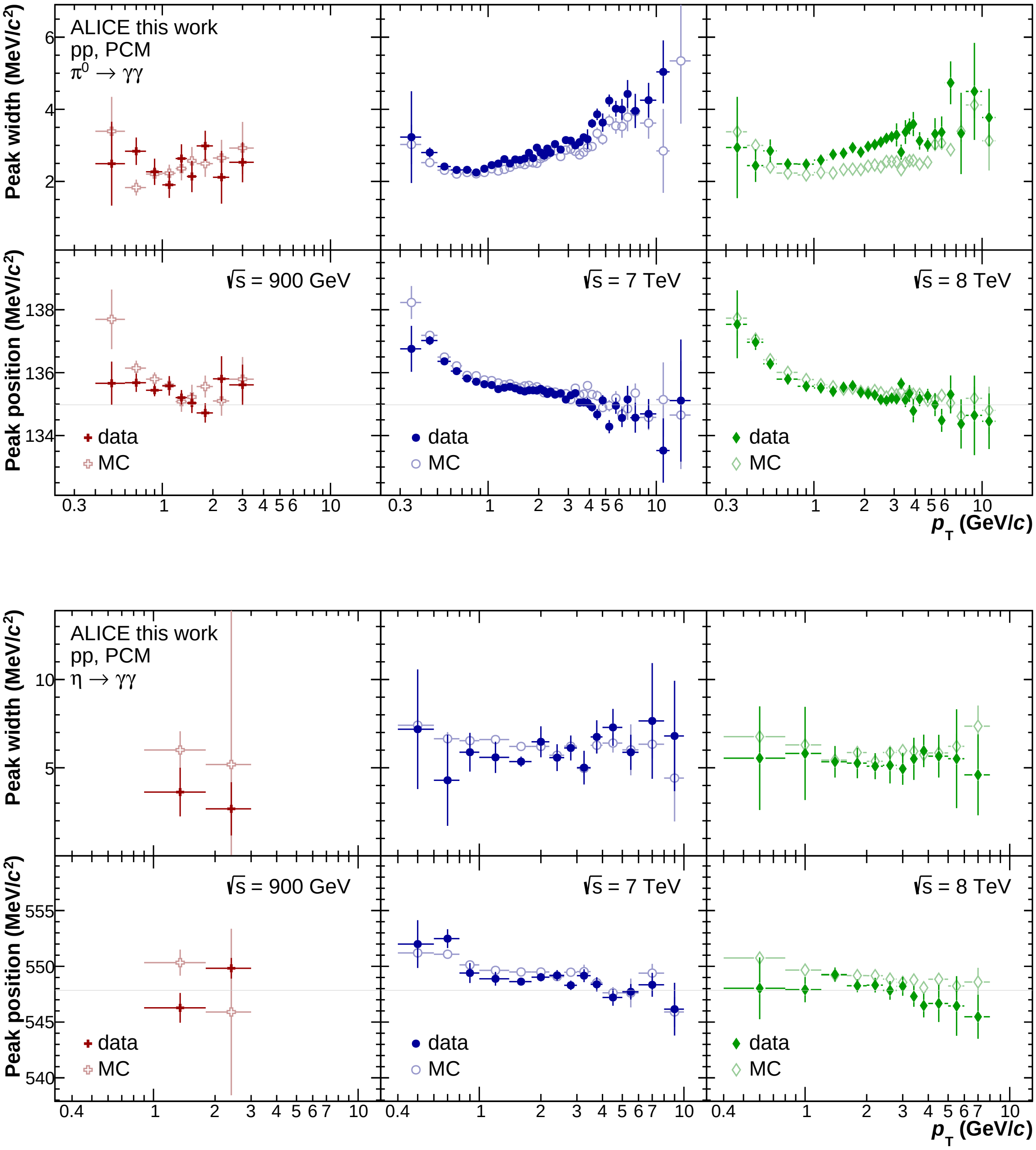

Figure 6.2: Mass and FWHM of the neutral mesons obtained from the respective invariant mass peak fits as a function of p_T. The upper plot shows the points for the neutral pions and the lower plot for the η mesons. Data is shown with full points whereas Monte Carlo is given by the open points. The gray line indicates the respective nominal meson mass.

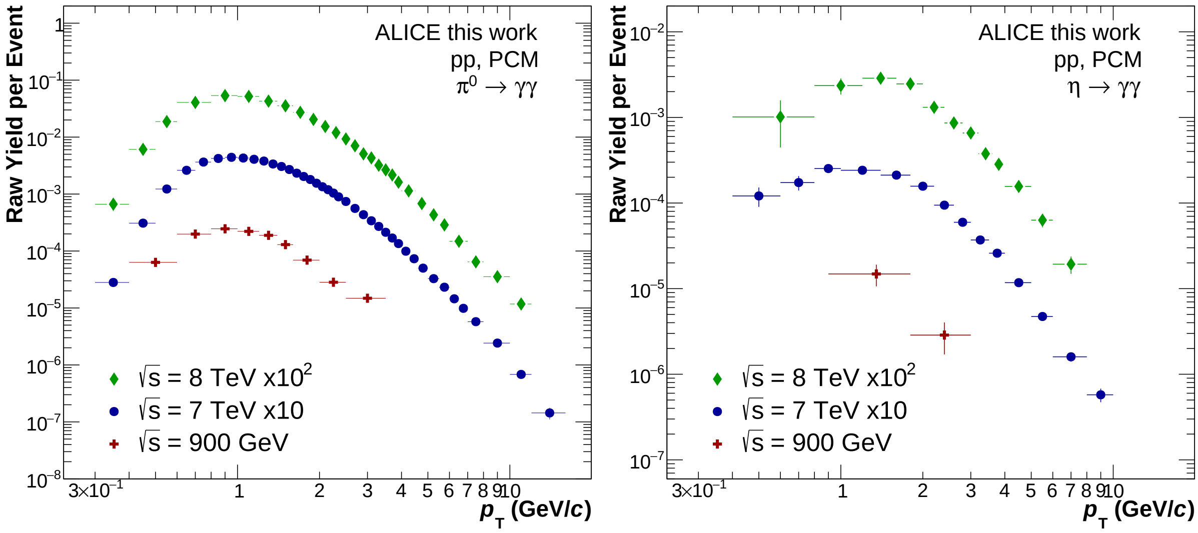

Figure 6.3: Left: Raw yield of the neutral pion for the three center-of-mass energy measurements. **Right:** Raw yield of the η meson per Event versus transverse momentum. All spectra are normalized by the number of events N_{norm}. $\sqrt{s}$ = 8 TeV points have additionally been scaled by a factor 100 and $\sqrt{s}$ = 7 TeV points by a factor of 10.

corresponds to $(-8\langle n\sigma_\eta\rangle, 3\langle n\sigma_\eta\rangle)$ around M_η. Similar to the π^0 the η meson raw yield is therefore given by:

$$N^{\eta}_{\mathrm{raw}} = \int_{M_\eta - 0.048\mathrm{GeV/c^2}}^{M_\eta + 0.022\mathrm{GeV/c^2}} (N^{\gamma\gamma} - N^{\mathrm{comb.BG}})\mathrm{d}M_{\gamma\gamma} - \int_{M_\eta - 0.048\mathrm{GeV/c^2}}^{M_\eta + 0.022\mathrm{GeV/c^2}} (B + C \cdot M_{\gamma\gamma})\mathrm{d}M_{\gamma\gamma} \quad (18)$$

The resulting raw yields for π^0 and η mesons for every center-of-mass energy can be seen in Figure 6.3. The raw yield is normalized to the number of events N_{norm} as given in Table 2 and by the bin with in transverse momentum. The p_{T} reach of each measurement is mainly limited by statistics at large transverse momenta and increasing background as well as constraints introduced by the analysis cuts at low p_{T}. The most important constraint at low transverse momentum is the minimum track momentum cut of 50 MeV/c which restricts the minimum momentum for the meson measurement to be greater than 0.2 GeV/c. This is the reason for the further signal extraction range of the $\sqrt{s}$ = 7 TeV measurement up to 16 GeV/c while the other measurements are limited at 12 and 3.5 GeV/c respectively for the neutral pion.

The η meson extraction is additionally limited by the smaller signal due to its branching ratio of only 38% for the two photon decay. This in addition with a smaller acceptance for the conversion photons from the η mesons leads to the more restricted extraction range which reaches up to 10 GeV/c in the $\sqrt{s}$ = 7 TeV measurement.

6.2 Neutral Meson Spectrum Corrections

The neutral meson raw yields from the last section require several corrections for which the additional Monte Carlo information as well as the cocktail simulation are used. In the following sections the raw yield will be corrected for out-of-bunch pileup, secondary particles, detector acceptance and efficiency, conversion probabilities as well as the finite bin width.

6.2.1 Correction for Neutral Mesons from Out of Bunch Pileup Vertices

The out-of-bunch pileup correction has become of increasing importance since the beginnings of the ALICE data taking. This correction is linked to the luminosity during data taking as well as the filling schemes and bunch spacings in the LHC. In Figure 6.4 the luminosity for all periods is shown and it shows that even during the data takings of the $\sqrt{s} = 7$ TeV periods a four orders of magnitude increase in luminosity was present whereas during the $\sqrt{s} = 8$ TeV periods it fluctuates strongly between three orders of magnitude with the last periods showing the highest peak luminosity. This behavior was already observed for the in-bunch pileup in Figure 4.2. While the in-bunch pileup originates from collisions of protons from the same bunch-pair and can be efficiently removed using the fast ITS detector systems, the out of bunch pileup comes from interactions between different bunches and is observed in the TPC. This is due to the drift velocity of charges in the TPC gas of about 2.7 cm/μs which results in drift times of about 92 μs. This is the same time that a bunch in the LHC requires for a full revolution around the 27 km ring. Therefore multiple events can overlap in the TPC chamber for which the TPC reconstruction algorithms are not equipped as they were designed to reconstruct one primary vertex at a time. The overlap of events and the presence of multiple primary vertices in a high luminosity environment therefore requires the out-of-bunch pileup correction.

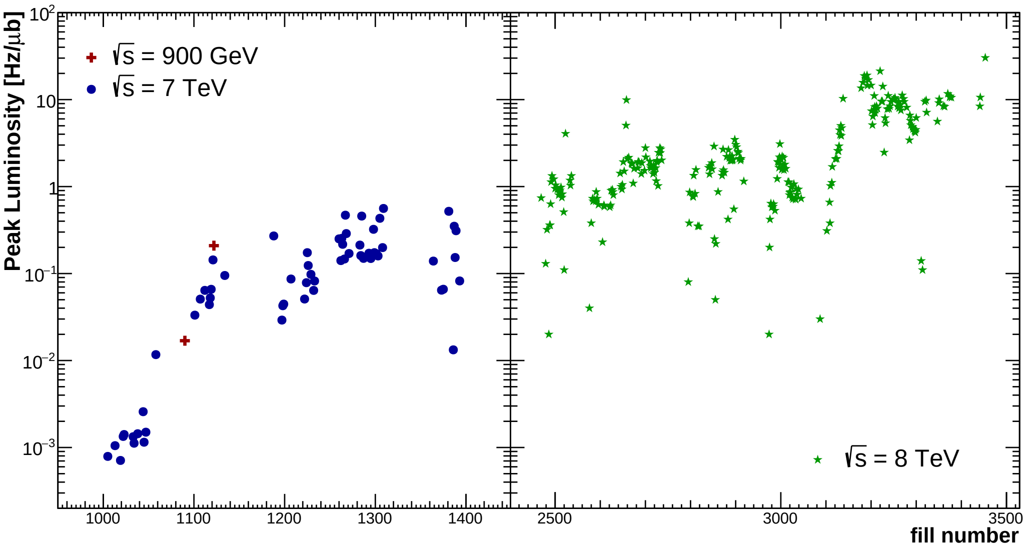

Figure 6.4: Peak luminosity of the LHC as a function of the fill number for the ALICE experiment [71]. Points are shown for the three center-of-mass energies $\sqrt{s} = 0.9$, 7 and 8 TeV.

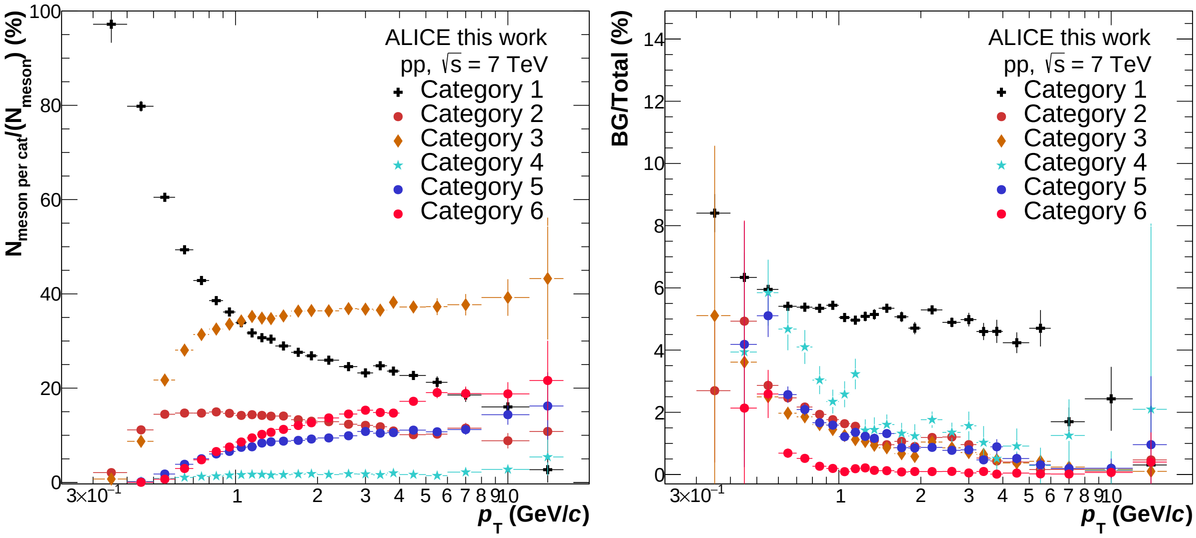

Figure 6.5: Left: Fraction of the neutral pions in the respective categories for pp at $\sqrt{s}$ = 7 TeV with respect to the total amount of neutral pions measured in the data sample. **Right:** Fraction of the neutral pions originating from pileup vertices with respect to the inclusive measured neutral mesons in the respective category.

The correction itself is based on the distance of closest approach (DCA) in beam direction (z) of the photons to the primary vertex. This is calculated by using a straight line from the momentum vector of the photon and determining the closest distance to the primary vertex from this line. The DCA itself was already explained in Section 5.1. The DCAz distributions are extracted in transverse momentum bins and are shown in the appendix in Section C.3 for the three center-of-mass energy measurements.

The photons that are reconstructed with the PCM method can be separated into three types depending on the detectors that are available for the leg reconstruction.

1. both legs are TPC only tracks (valid for all photons with $R_{\text{conv}} \geq 50$ cm)
2. one of the electrons has at least two hits in the Inner Tracking System
3. both legs have at least two ITS hits

The contributions of these types to the total photon yield is shown in Table 7 for the three center-of-mass energy measurements. The first type contributes the largest amount to the photon yield whereas type 2 does the least. The small contribution from type 2 is expected as it is very unlikely to have one leg with more than two ITS clusters while the other leg does not have ITS hits. However, two effects give rise to this type; dead areas in the ITS and the appearance of a single cluster for both electrons when passing the ITS through the same sensor. This single cluster will be assigned to only one of the electrons later detected in the TPC.

With the three photon types it is now possible to look at the mesons in six different categories as they are composed of two photons.

1. both photons from category 1
2. one photon from category 1 and one photon from category 2

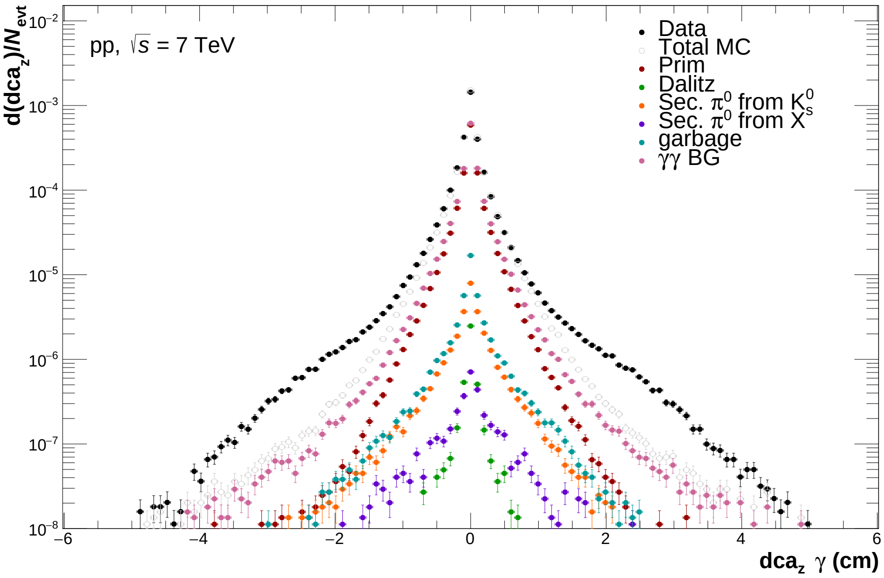

Figure 6.6: Integrated dca_z distribution of pp $\sqrt{s} = 7$ TeV photons in the invariant mass windows of 0.12 GeV/c $< M_{\gamma\gamma} <$ 0.145 GeV/c plotted together with the Monte Carlo distributions.

3. one photon from category 1 and one photon from category 3
4. both photons from category 2
5. one photon from category 2 and one photon from category 3
6. both photons from category 3

These categories are strongly momentum dependent as seen in the left plot of Figure 6.5. The largest contribution, especially at low p_{T}, comes from category 1 whereas category 2 and 3 are already fairly suppressed due to the ITS condition which forces the mesons to originate from the primary vertex. The strongest constrain is implied on category 6 where both photons contain ITS information and therefore are ensured to not originate from pileup events. However it is only a very small fraction of about 2% of the total meson yield.

	Photon Types [% of total]			Meson Types [% of total]					
$\sqrt{s}$	1	2	3	1	2	3	4	5	6
900 GeV	81.6	5.2	13.1	39.3	14.2	32.2	1.44	5.94	6.79
7 TeV	74.8	8.9	16.2	36.5	13.9	32.7	1.46	6.92	8.40
8 TeV	87.2	5.0	7.7	46.6	14.2	26.8	1.45	5.44	5.42

Table 7: Left half: Fractions of the photons to the total photon yield for the three different leg reconstruction types. **Right half:** Fraction of mesons coming from the six categories to the total meson yield.

In order to estimate the background coming from pileup the DCAz distributions are used. An example bin with data and additional MC points is shown in Figure 6.6. The pileup is estimated by fitting the background distribution which is visible as a broadening of the

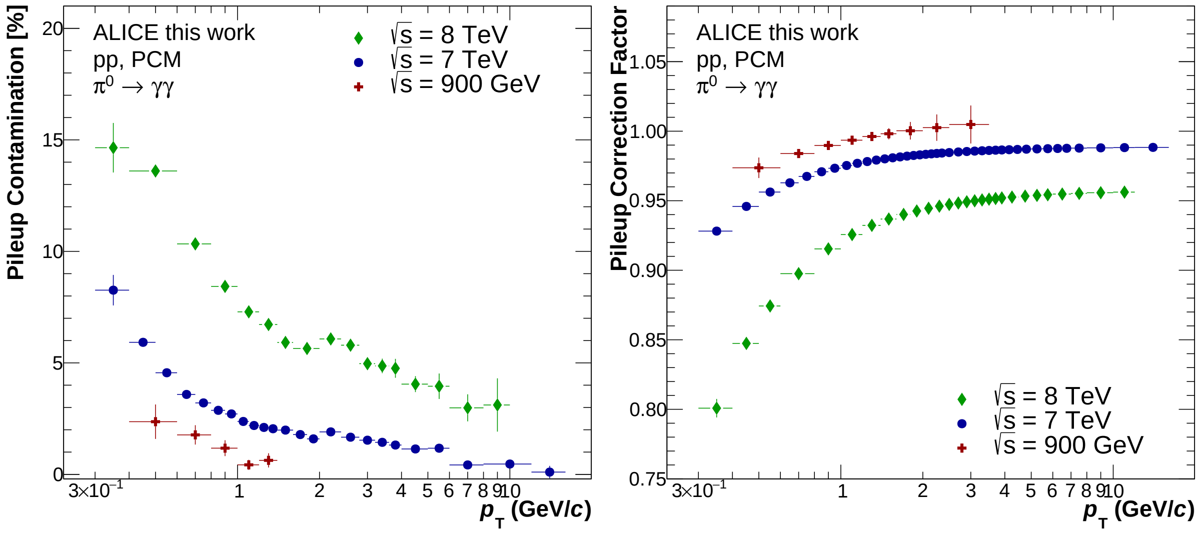

Figure 6.7: Left: Contamination from pileup to the inclusive neutral pion yield. **Right:** Final correction factor due to neutral pions originating from pileup vertices. Points shown for the three center-of-mass energy measurements investigated in this analysis.

data distribution compared to the MC distribution. For this background description a function called 'ShowBackground' is used which is implemented in the ROOT class TH1. This function has proven to be a better estimation than a Gaussian fit. For the different center-of-mass energy measurements different parameters for this function were used; 11 iterations for $\sqrt{s}$ = 900 GeV, 9 iterations $\sqrt{s}$ = 7 TeV and 11 iterations for $\sqrt{s}$ = 8 TeV as well as a background smoothing of 3 for all three energies. The fits for all transverse momentum bins can be seen in Section C.3 indicated by the blue line. The fitting is done for all categories and each momentum bin. The resulting fraction the background categories to the total yield is shown in the right plot of Figure 6.5. The fractions are then multiplied by the fraction of mesons in the respective category to obtain the final pileup fractions.

Those fractions are shown in Figure 6.7 as well as the smoothed final correction factors for the three measurements. As expected there is a large pileup contribution at low p_{T} where it is dominated by TPC-only reconstructed photons. In addition, the pileup correction for the high interaction rate $\sqrt{s}$ = 8 TeV measurement is by a factor of two larger than for the $\sqrt{s}$ = 7 TeV measurement. The finally applied corrections on the meson yields are around 1–3% for 900 GeV, 2–8% for 7 TeV and 5–20% for 8 TeV.

6.2.2 Correction for Secondary Neutral Pions

Secondary neutral pions from weak decays or hadronic interactions need to be removed from the raw yield in order to get only primary π^0 mesons. The largest source of these secondary pions is the decay $\mathrm{K}^0_S \rightarrow \pi^0\pi^0$ which is directly followed by material interactions in front of the TPC and by the decays of K^0_L and Λ. Due to the large decay lengths and decay kinematics of the K^0_L and Λ they contribute only very little as they usually decay at very large radii and are therefore not detected in the TPC. Due to this, they contribute at least one order of magnitude less to the pion yield then the K^0_S. The yields for kaons have been measured in $\sqrt{s}$ = 900 GeV [72] and in $\sqrt{s}$ = 7 TeV [73]. For

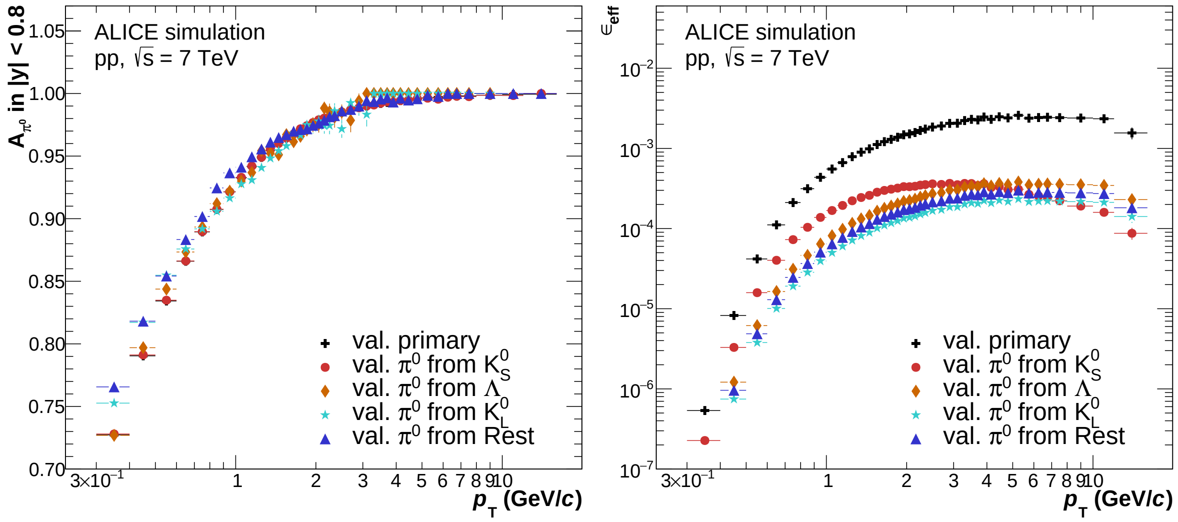

Figure 6.8: Acceptance (**left**) and reconstruction efficiency (**right**) for secondary neutral pions from different sources compared to the respective quantities for the primary pions.

the $\sqrt{s} = 8$ TeV measurement currently no direct measurement exists and therefore an extrapolated spectrum from the 7 TeV and 2.76 TeV [74] results is used. The spectra are used to generate a decay simulation, the so-called cocktail, for the secondary particle correction. However, the secondary particles coming from the material interactions are derived from the Monte Carlo simulations. The following paragraphs will explain both methods and their influence on the neutral pion raw yield.

6.2.2.1 Secondary Neutral Pion Cocktail

This method uses the measured spectra for kaons (K^0_S or $K^\pm$) and Λ as parametrized input for a Pythia 6 event generator. The decays are generated flat in transverse momentum, for a rapidity of $|y| < 1$ and the full azimuthal angle of $0 \leq \phi \leq 2\pi$. Table 8 shows the decay channels and branching ratios that are considered for the cocktail simulation. An extended version of this table is shown in Table 13 for the generation of the decay photon cocktail which will be explained in the corresponding chapter. Detailed information about the cocktail generation will be given in Section 7.2.1. The neutral pion yield is then calculated for the rapidity windows of this analysis $|y| < 0.8$ and the acceptance and efficiency for the secondary π^0 mesons obtained from the full detector simulations is applied. This is necessary to obtain the secondary raw yield from the generated spectra and to then subtract this yield from the π^0 raw yield. The generation of particles for the cocktail is

particle	decay channel	branching ratio	decay length ($c\tau$)
K^0_S	$\pi^0\pi^0$	30.69%	2.6844 cm
K^0_L	$\pi^0\pi^0\pi^0$ $\pi^+\pi^-\pi^0$	19.46% 12.50%	15.34 m
Λ	nπ^0	35.80%	7.89 cm

Table 8: Particles considered in the cocktail and their respective decay channels, branching ratios and decay lengths.

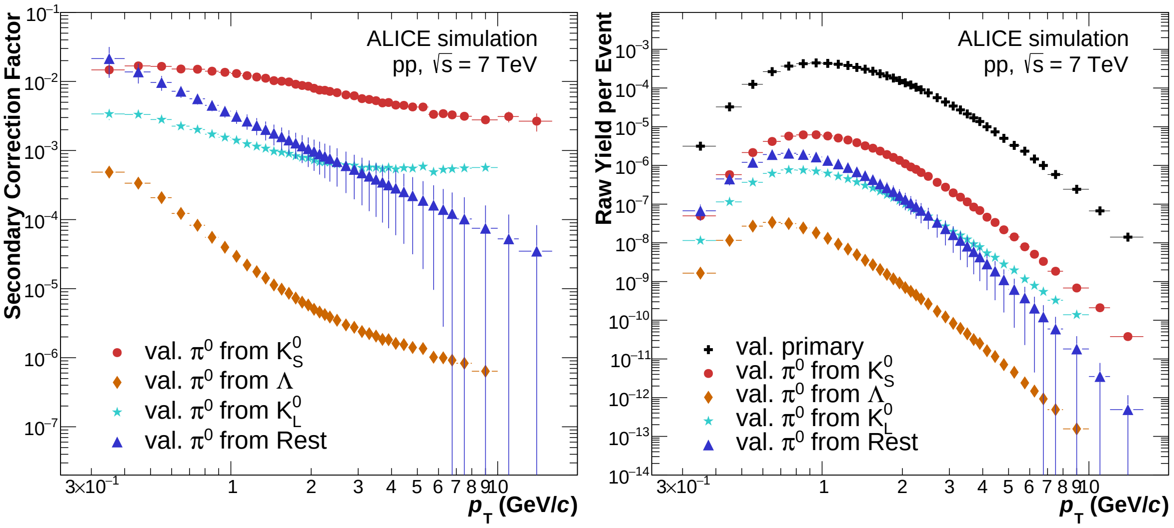

Figure 6.9: Left: Ratio of reconstructed secondary π^0 mesons from different sources to reconstructed neutral pions. **Right:** Secondary raw yield per event versus transverse momentum for all sources.

done flat in p_{T}, η and ϕ and the particles are then weighted with the parametrization of the measured transverse momentum distributions. The comparison of secondary acceptance and efficiency to the primary neutral pions is shown in Figure 6.8. The efficiencies shown are evaluated using fits to the ratio of the primary to the secondary efficiencies which are then multiplied by the primary efficiency. The ratio of the efficiencies was fitted with an exponential for the K^0_S and a constant for the K^0_L and Λ. This step was necessary as the efficiencies from Monte Carlo lacked statistics towards high transverse momentum whereas the cocktail spectra have negligible statistical uncertainties over the full p_{T} range. Fitting the efficiencies therefore allows a smooth and full application of the detector response up until the largest transverse momentum bin.

The final secondary raw yields that need to be subtracted from the π^0 raw yield are shown in Figure 6.9 alongside with the effective correction from each secondary source. This also shows that the K^0_S contribution is the largest for the secondaries while the neutral pions from K^0_L make one order of magnitude less of a contribution to the raw yield. A negligible impact on the π^0 meson raw yield have the secondaries from Λ mesons which are another two orders of magnitude lower.

6.2.2.2 Material Interactions from Monte Carlo

Besides the contributions from K^0_S, K^0_L and Λ an additional correction for the secondaries from material interactions and other particles that are considered for secondary interactions is required. The correction is fully based on the reconstructed fraction of secondary pions provided by the Monte Carlo simulations. This contribution, shown as "Rest" in Figure 6.8 and Figure 6.9 is dominated by the material interactions which make more than 99% of the secondary neutral pions from this category. Similar to the cocktail method the efficiency for this source of secondaries is also obtained from a fit in the efficiency ratio of secondaries to primaries. This again allows this correction to be applied over the whole p_{T} range. The final raw yield as shown in Figure 6.9 is then also subtracted from the neutral meson raw yield.

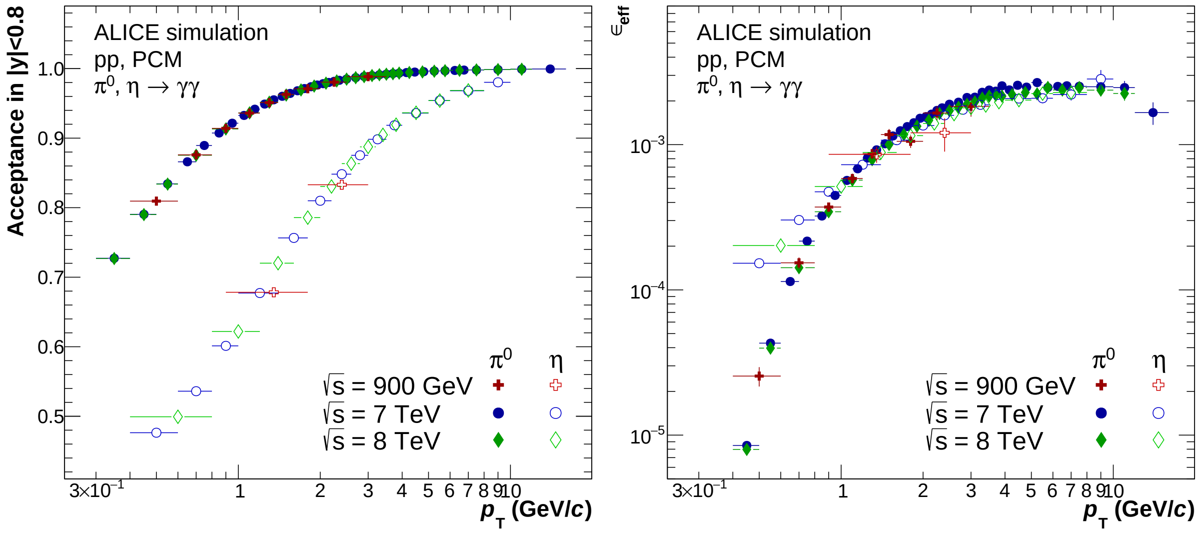

Figure 6.10: Left: Geometrical acceptance for the neutral mesons. **Right:** Reconstruction efficiency for π^0 and η mesons obtained from the Monte Carlo simulations and shown for all center-of-mass energies.

6.2.3 Correction for Acceptance and Efficiency

The secondary corrected raw yield is now corrected for the limited detector acceptance and the efficiency to reconstruct the mesons. In order to obtain the corrections the additional information provided by the Monte Carlo simulations is used. The p_{T} dependent geometrical acceptance $A_{\pi^0(\eta)}$ is a detector property and limited by the physical dimensions of the TPC in this analysis. It is defined as the ratio of π^0 (η) mesons within $|y| < 0.8$ whose daughter particles are within the pseudorapidity acceptance of $|\eta| < 0.9$ to the total amount of $A_{\pi^0(\eta)}$ mesons that are created in the same rapidity window.

$$A_{\pi^0(\eta)} = \frac{N_{\pi^0(\eta),|y|<0.8} \text{ with daughter particles within } |\eta_\gamma| < 0.9}{N_{\pi^0(\eta),|y|<0.8}} \tag{19}$$

The geometrical acceptance for both neutral mesons and the three center-of-mass energy measurements is shown in Figure 6.10. The acceptance shows only a difference between the mesons and no center-of-mass energy dependence. This is due to the fact that the TPC had the same dimensions during all data taking periods and therefore the same acceptance. The difference in the transverse momentum dependence between both mesons comes from the difference in opening angles due to the higher mass of the η meson compared to the π^0 meson. This results in decay products not being registered in the acceptance of the detector and therefore a decrease in the number of measured mesons in $|y| < 0.8$.

The correction for the reconstruction efficiency is determined by running the same analysis as for the measured data on the Monte Carlo simulations. In addition, each photon pair is verified to originate from the same neutral meson using the supplementary Monte Carlo information. With this verification, only true neutral mesons are reconstructed and it is possible to compare the true mesons to the reconstructed data mesons. The calculation of the reconstruction efficiency is done with the following formula.

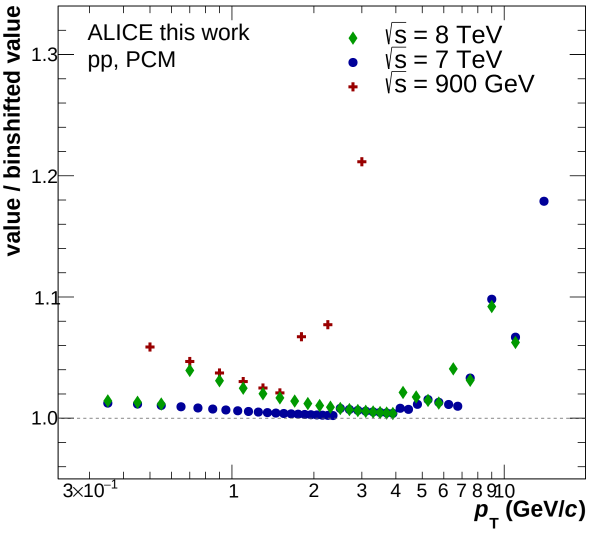

Figure 6.11: Bin shift correction factors obtained from the Tsallis fit to the neutral pion spectra for the three center-of-mass energy measurements.

$$\epsilon_{\mathrm{reco},\pi^0(\eta)} = \frac{\text{verified } N_{\pi^0(\eta),\mathrm{rec}}(p_{\mathrm{T}}, \mathrm{rec})}{N_{\pi^0(\eta),|y|<0.8} \text{ with daughter particles within } |\eta_\gamma| < 0.9(p_{\mathrm{T}}, \mathrm{rec})} \tag{20}$$

The reconstruction efficiency is shown in Figure 6.10 for both neutral mesons and the three center-of-mass energy measurements. The p_{T} dependence is determined by the conversion probability and the photon reconstruction efficiency. This comes from the requirement of both photons and their conversion products to be inside the detector acceptance and to additionally reach the TPC for their reconstruction. The reconstruction efficiency in Figure 6.10 therefore shows a slow rise until about 4 GeV/c where it finally levels out. The absolute value of the efficiency is dominated by the conversion probability of $\approx 8.6\%$ which enters quadratically as both photons are required to convert. In addition, the photon reconstruction efficiency itself with about 68% also enters quadratically which leads to a maximum efficiency of about 0.34% for the neutral mesons. This value, however, cannot be reached with the simulations but with about 0.3% is is coming very close with its maximum value.

6.2.4 Correction for Finite Bin Width

The neutral meson spectra are steeply falling and have different transverse momentum binnings. In addition, the binning becomes larger with increasing p_{T} and as a result the yield of the bin is no longer given by the central bin value but instead it needs to be shifted horizontally. This horizontal shift is done by using a Tsallis [75] fit function on the measured spectrum and shifting the bin centers to match with the fit function. The Tsallis function is given by:

$$E\frac{\mathrm{d}^3N}{\mathrm{d}p^3} = \frac{1}{2\pi p_{\mathrm{T}}}\frac{\mathrm{d}^3N}{\mathrm{d}y\mathrm{d}p_{\mathrm{T}}} = \frac{1}{2\pi}\frac{\mathrm{d}N}{\mathrm{d}y}\frac{(n-1)(n-2)}{nT^{\mathrm{eff}}(nT^{\mathrm{eff}}+m(n-2))}\left(1+\frac{\sqrt{p_{\mathrm{T}}^2+m^2}-m}{nT^{\mathrm{eff}}}\right)^{-n} \tag{21}$$

The parameters m and $\sqrt{m^2 + p_\mathrm{T}^2} = m_\mathrm{T}$ represent the neutral meson mass and the transverse mass. The remaining parameters $\frac{\mathrm{d}N}{\mathrm{d}y}$, T^eff and n are determined with the fit. The bin-shift correction strongly depends on the steepness and the bin width of the underlying spectrum. The bin shift correction factors for the neutral pion spectra of all three center-of-mass energy measurements are shown in Figure 6.11. This shows the importance of the correction and the correlation between bin width and the strength of the correction. Naturally, the high transverse momentum bins increase in width to incorporate enough statistics for a significant peak extraction. The correction ranges from 1% up to more than 20% depending on transverse momentum and the corresponding bin width.

6.3 Systematic Error Evaluation

The Monte Carlo simulations that are used for the correction of the measured spectra do not perfectly reproduce every physical quantity on which the analysis cuts are applied. The small differences will results in systematic changes of the final spectrum depending on the strictness of the cuts. Therefore the cuts for the track selection, the electrons, the photons and the mesons are varied one at a time and their effect on the final spectrum is compared to the standard cut used in the analysis. The calculation of the variations is done bin by bin with the following formulas for the deviation $\Delta(p_\mathrm{T})$ and the statistical uncertainty of the deviation $\sigma_\Delta(p_\mathrm{T})$.

$$\Delta(p_\mathrm{T}) = \left(\frac{\mathrm{d}^2N}{\mathrm{d}y\mathrm{d}p_\mathrm{T}}\right)_\mathrm{modified}(p_\mathrm{T}) - \left(\frac{\mathrm{d}^2N}{\mathrm{d}y\mathrm{d}p_\mathrm{T}}\right)_\mathrm{standard}(p_\mathrm{T}) \tag{22}$$

$$\sigma_\Delta(p_\mathrm{T}) = \sqrt{\left|\sigma^2_{\left(\frac{\mathrm{d}^2N}{\mathrm{d}y\mathrm{d}p_\mathrm{T}}\right)_\mathrm{modified}}(p_\mathrm{T}) - \sigma^2_{\left(\frac{\mathrm{d}^2N}{\mathrm{d}y\mathrm{d}p_\mathrm{T}}\right)_\mathrm{standard}}(p_\mathrm{T})\right|} \tag{23}$$

Due to the limited statistics in several transverse momentum bins it is very important to check for the statistical significance of the deviation to not incorporate statistical uncertainties into the systematical uncertainties. Therefore some variations are evaluated on a wider binning and the resulting more significant deviations are then assumed for the underlying merged bins.

The calculation of the errors within one cut is done on a bin by bin basis and by using the average of the maximum deviation in both, positive and negative, direction. A detailed overview of the cut variations used for the systematic error evaluation is given in Table 9. In addition there are also non cut based variations for the yield extraction and the uncertainty coming from the merging of different periods in the $\sqrt{s} = 7$ and 8 TeV analysis. The main categories of systematic error sources will be explained in the following:

Material Budget: The with 9.0% largest systematic error source for the mesons is the material budget uncertainty. The contribution from this source was studied in detail in [76] by investigating the differences between the offline and online V^0 finders as well as the influence from using different Monte Carlo generators. As for this uncertainty cut variations on the R distribution of the photon candidates were made there will be no additional variation of this cut in the systematic error evaluation.

Quantity	Standard	Cut Variation1	Cut Variation2	Cut Variation3
Track cuts				
single p_{T} $e^{\pm}$	> 0.05 GeV/c	> 0.040 GeV/c	> 0.075 GeV/c	> 0.1 GeV/c
min TPC clust./ find. TPC clust.	$> 60\%$	$> 35\%$	$> 70\%$	
dE/dx e-line				
$\sigma_{\mathrm{d}E/\mathrm{d}x,e}$	$-3 < n\sigma_e < 5$	$-4 < n\sigma_e < 5$	$-2.5 < n\sigma_e < 4$	
dE/dx π-line				
$p_{\mathrm{min},\pi\mathrm{rej.}}$	0.4 GeV/c	0.25 GeV/c	0.5 GeV/c	
$p_{\mathrm{max},\pi\mathrm{rej.}}$	3.5 GeV/c	2.0 GeV/c	5.0 GeV/c	
$n\sigma_{\mathrm{d}E/\mathrm{d}x,\pi}$ rej.	$n\sigma_\pi > 1$	$n\sigma_\pi > 2$	$n\sigma_\pi > 0$	
high p $\sigma_{\mathrm{d}E/\mathrm{d}x,\pi}$ rej.	$n\sigma_\pi > -10$			
Photon cuts				
$q_{\mathbf{T,max}}$	< 0.05 GeV/c (2D)	< 0.07 GeV/c (1D)	< 0.03 GeV/c (2D)	< 0.05 GeV/c (1D)
χ^2 γ	< 30	< 50	< 20	
Ψ_{pair}	< 0.1 (2D)	< 0.2 (2D)	< 0.05 (2D)	< 0.1 (1D)
Meson cut				
α **meson**	< 1	< 0.85	< 0.75	

Table 9: Variations for the neutral meson systematic error evaluation for all three center-of-mass energy measurements. The "Standard" column stands for the standard cut while the "Cut variation" columns show the variations that are applied to the standard cut. Only one cut (row) is changed at a time to estimate the systematic error.

Signal Extraction: Contributions to this category come from the energy asymmetry of the two photons as well as uncertainties due to the signal extraction itself. The peak positions, widths and shapes in data and Monte Carlo do not perfectly agree and therefore a systematic difference in integration range between both sides of the invariant mass peak are present. Due to this, a variation on the integration range in both directions, more narrow and wider, is done to estimate the uncertainty due to this difference. Table 10 shows the different integration ranges used for the estimation. The signal extraction is an important contribution to the overall systematic uncertainty especially for the harder to extract low and high momentum p_{T} bins and for the η meson with its much wider peak. With 1–15% this contribution also shows the largest transverse momentum dependence.

Integration range	π^0	η
standard	$(M_{\pi^0} - 0.035,\ M_{\pi^0} + 0.012)$ GeV/c^2	$(M_\eta - 0.048,\ M_\eta + 0.022)$ GeV/c^2
narrow	$(M_{\pi^0} - 0.015,\ M_{\pi^0} + 0.005)$ GeV/c^2	$(M_\eta - 0.036,\ M_\eta + 0.010)$ GeV/c^2
wide	$(M_{\pi^0} - 0.055,\ M_{\pi^0} + 0.025)$ GeV/c^2	$(M_\eta - 0.068,\ M_\eta + 0.025)$ GeV/c^2

Table 10: Variations of the integration windows for the systematic error estimation from the signal extraction.

Track Reconstruction: This category contains the cuts that are used on the electron and positron tracks. This includes the TPC cluster over findable cluster cut as well as the minimum transverse momentum cut. Both contributions are based on TPC performance differences between data and Monte Carlo. Despite the Monte Carlo being tuned to reproduce the TPC conditions during each run, there can be differences which will contribute to this uncertainty. Due to large statistical fluctuations both uncertainties have been smoothed above 2 GeV/c where they contribute around 1% to the total systematic error. However, at low p_{T} there is a strong rise of the TPC cluster uncertainty especially for the η meson which results in this source contributing more then the material budget in the lowest momentum bin.

Electron Identification: The cuts on the nσ dE/dx distributions for electrons identification and pion rejection are the two components of this systematic uncertainty category. As visible in Figure C.1 in the appendix the nσ distributions have a different shape in data and Monte Carlo as the latter is tuned to be a perfect mean distributions around zero whereas the data had a Bethe Bloch based splines calibration. This calibration, however, is not perfect and results in the mean not being exactly centered around unity. The contribution from this category is transverse momentum dependent and produces an uncertainty of about 1–4%.

Photon Reconstruction: The photon reconstruction related systematic uncertainties are the q_{T} cut as well as the 2D cut in χ^2 and Ψ_{Pair}. Being strongly correlated, the cut variations of the 2D cut components are looked at together and result in one combined contribution. The uncertainties are smoothed with a parabolic function to account for the low and high p_{T} rise of the deviations to the standard cut. This uncertainty adds up to 1–8% depending on transverse momentum.

Pileup: For the pileup contribution estimation two approaches were used. The first approach is a variation of the ShowBackground fit parameters to stronger and more loose constraints. The second approach is using a Gaussian instead of the ShowBackground fit for the background description of the DCAz distribution. This resulted in a contribution flat in p_{T} of 1–3% depending on the center-of-mass energy.

Periods: The systematic uncertainty from the merging of the different periods LHC10[b-f] and the periods LHC12[a-i] is estimated by running the full analysis on each period separately and comparing each single period measurement to the merged results. The motivation of this category is the difference in detector performance between the periods and how well this is reproduced in Monte Carlo. This resulted in a 1.5% contribution for the 7 TeV measurement and a 3% contribution for the 8 TeV measurement.

The contributions from each systematic uncertainty category as well as the total systematic uncertainty are shown in Figure 6.12 for both neutral mesons and the three center-of-mass energy measurements. All detailed systematic error sources are given in the appendix in Figure C.13. The total uncertainty is generally dominated by the material budget contribution. However, at low and high transverse momentum the signal extraction generates larger contributions for both mesons. For the neutral pion measurement a total uncertainty of 10–20% is observed. The η meson measurement shows slightly larger uncertainties with 12–25%.

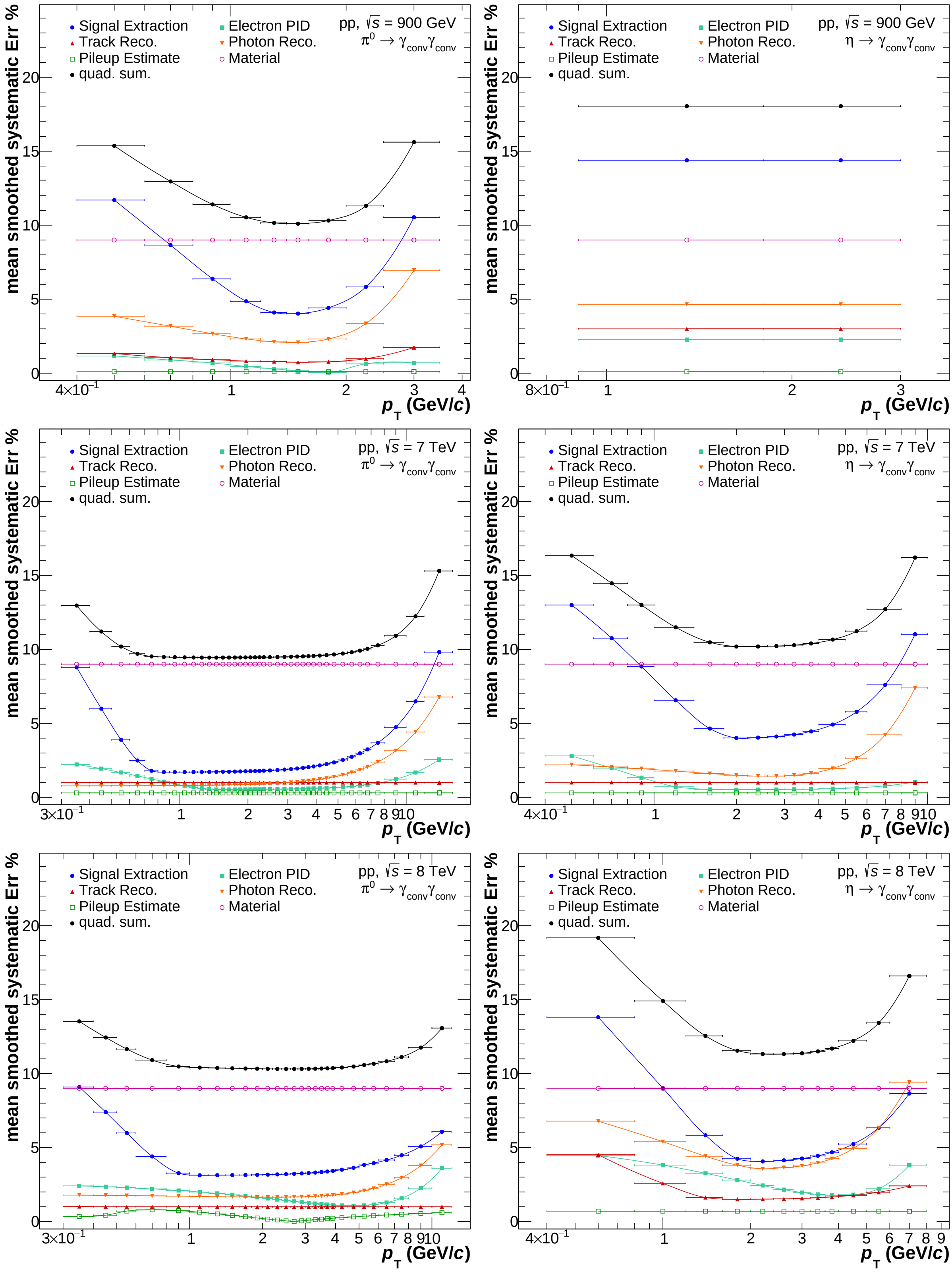

Figure 6.12: Visualization of the smoothed systematic errors for the π^0 and η meson measurement at the three presented center-of-mass energies. Indicated with colored points are the individual error sources whereas the final systematic uncertainty is represented with the black points.

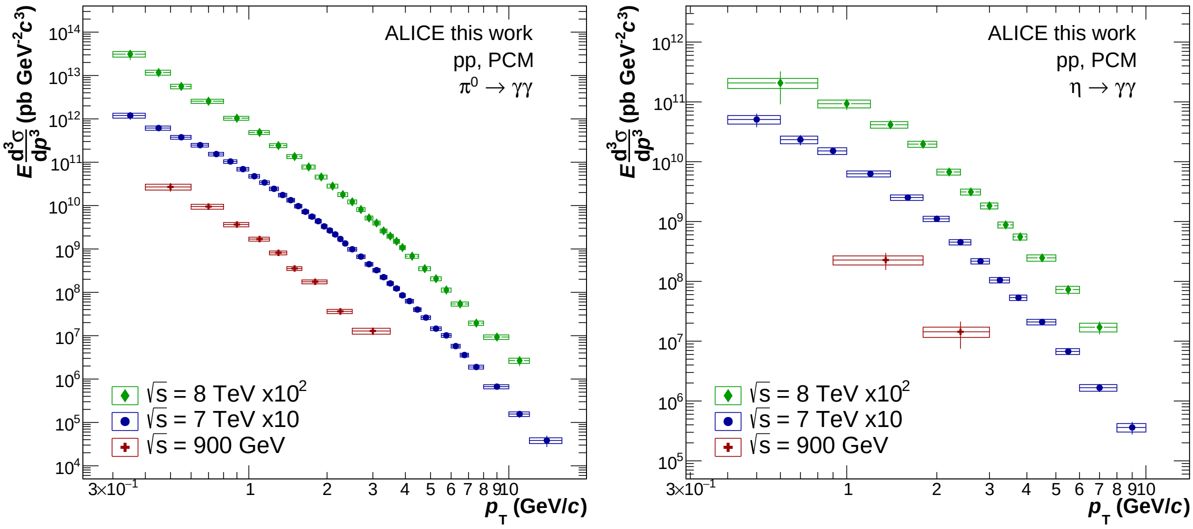

Figure 6.13: Differential invariant cross sections of the π^0 and η mesons in pp collisions at different energies as a function of the transverse momentum. The data is from PCM only and includes the systematic uncertainties.

6.4 Fully Corrected Neutral Meson Cross Sections

In this section all corrections which were explained in Section 6.2 are applied to the π^0 and η meson raw yield. At first the pileup correction is applied to the raw yield. Afterwards, the secondaries are subtracted to obtain the number of events $N^{\pi^0(\eta)}$ for the following formula. The resulting quantities from this are then the fully corrected invariant π^0 and η meson cross sections and are calculated the following way:

$$E\frac{\mathrm{d}^3\sigma}{\mathrm{d}p^3} = \frac{1}{2\pi}\frac{1}{p_\mathrm{T}}\frac{\sigma_\mathrm{MB}}{N_\mathrm{evt.}}\frac{1}{\epsilon_{\mathrm{reco},\ \pi^0(\eta)}}\frac{1}{A_{\pi^0(\eta)}}\frac{1}{\mathrm{BR}}\frac{N^{\pi^0(\eta)}}{\Delta y \Delta p_\mathrm{T}}. \tag{24}$$

The components of this formula are given as:

p_T represents the bin-shift corrected transverse momentum of the given bin

σ_MB is the minimum trigger cross section that was given for each center-of-mass energy in Section 4.3 and is either from the V0OR (900 GeV and 7 TeV) or the V0AND (8TeV) minimum bias trigger

$N_\mathrm{evt.}$ is the number of events that are used for normalization as shown in Table 2

ϵ_reco and $A_{\pi^0(\eta)}$ are the reconstruction efficiency and the acceptance as shown in Figure 6.10 that are obtained from the Monte Carlo simulations

BR is the branching ratio of the decay $\pi^0 \rightarrow \gamma\gamma$ and $\eta \rightarrow \gamma\gamma$. It is given in Table 13 for both mesons

$N^{\pi^0(\eta)}$ is the number of reconstructed π^0 or η mesons within the rapidity range Δy and the transverse momentum bin Δp_T

The calculated fully corrected invariant cross sections for both mesons and the three center-of-mass energy measurements are shown in Figure 6.13.

$\sqrt{s}$	system	p_{T} reach for π^0 (GeV/c)	p_{T} reach for η (GeV/c)
900 GeV	PCM	0.4 – 3.5	0.9 – 3.0
	PHOS	0.6 – 7.0	N/A
7 TeV	PCM	0.3 – 16.0	0.4 – 10.0
	EMCal	0.6 – 25.0	3.0 – 35.0
	PCM-EMCal	0.8 – 16.0	1.0 – 12.0
	PHOS	0.8 – 25.0	1.0 – 20.0
8 TeV	PCM	0.3 – 12.0	0.4 – 8.0
	EMCal	1.2 – 20.0	2.0 – 35.0
	PCM-EMCal	0.8 – 35.0	1.2 – 25.0
	PHOS	1.0 – 35.0	N/A

Table 11: Transverse momentum reach for both neutral mesons for each center-of-mass energy measurement and each reconstruction method.

6.4.1 Comparison to other Reconstruction Methods

The neutral mesons in this thesis are measured using the photon conversion method where the photons are reconstructed from their conversion products using the TPC and the Inner Tracking System. However, this method is only one of a variety of possible reconstruction methods. Other measurements, for example, include the Electromagnetic Calorimeter (EMCal) or the Photon Spectrometer (PHOS) to reconstruct the decay products of the neutral mesons.
Each of the different reconstruction methods has its advantages as well as disadvantages depending on the transverse momentum. Whereas only the PCM method can reach down to very low p_{T}, the calorimeters are superior at very high transverse momentum. In the following, the spectra obtained with the PCM method are compared with the other reconstruction methods. In addition, the combination of the different methods is explained.

The neutral mesons at $\sqrt{s} = 8$ TeV have been measured with PCM [77], PHOS [78], EMCal [79] as well as the hybrid method PCM-EMCal [80]. In addition, the EMCal measurement also incorporates the L0 and L1 triggered data from this data set. This allows a maximum transverse momentum reach for both neutral mesons up to 35 GeV/c. The combination of the measurements as well as additional comparisons are explained in more detail in the combination Analysis Note [81].

Neutral mesons at $\sqrt{s} = 7$ TeV have been measured with the same reconstruction methods as in 8 TeV: PCM [82], PHOS [83], EMCal [83], PCM-EMCal [84]. The EMCal measurement, however, is based on a different $\sqrt{s} = 7$ TeV data set (LHC11c/d) where additional EMCal sectors were available and therefore the acceptance for the analysis is increased.

For the lowest center-of-mass energy of 900 GeV there are only two reconstruction methods available: PCM and PHOS [85]. The rather low statistics in this dataset also makes the reconstruction of the η meson using PCM very challenging and impossible for the PHOS measurement.

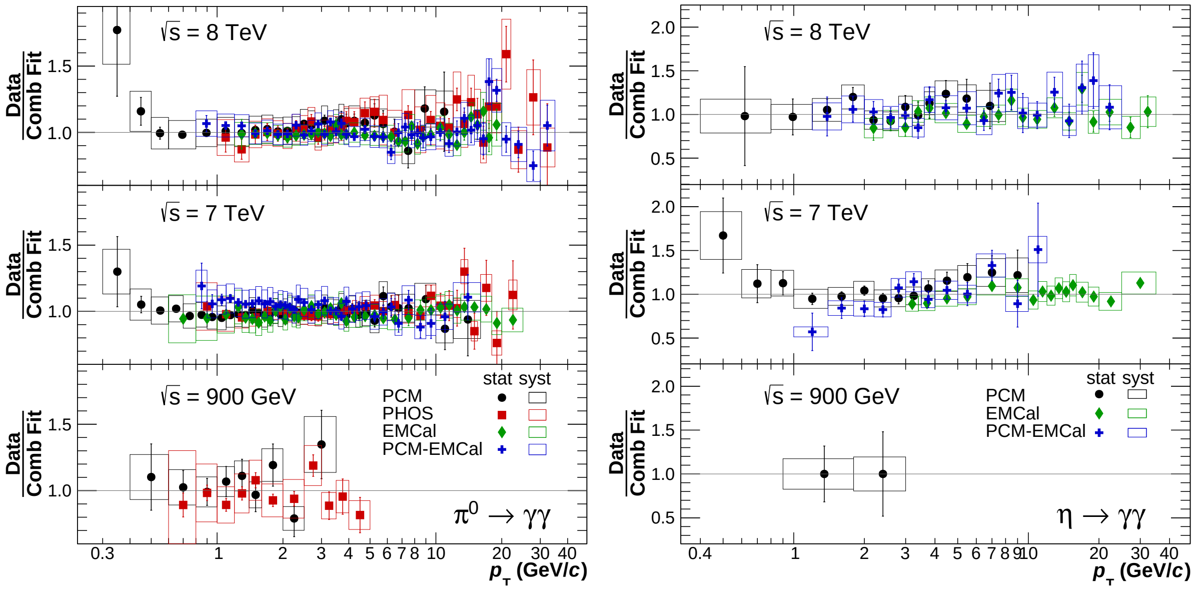

Figure 6.14: Ratios of the differential invariant cross sections of the π^0 and η mesons to the combined spectrum in pp collisions at different energies and for each reconstruction method used in the combination.

An overview of the transverse momentum reach of each reconstruction method for all three data sets is shown in Table 11.
For the combination of the spectra it is important to account for possible correlations in the uncertainties as each spectrum provides its own statistical and systematical uncertainties. However, the statistical uncertainties are assumed to be uncorrelated between the different methods. This can be assumed as it is very unlikely that all conversion products of the same neutral meson are measured in the EMCal, PHOS and TPC at the same time. Due to different acceptances as well as a focus on different decay kinematics, this assumption for the combination can be used. However, the systematical uncertainties are correlated between the PCM and EMCal-based measurements but not with the PHOS measurement as it has no common uncertainty with the other three systems. The calculation of the correlations using a correlation matrix that links the PCM and EMCal systematics with the PCM-EMCal hybrid methods uncertainties is explained in great detail in the $\sqrt{s}$ = 8 TeV combination Analysis Note [81] and will not be further explained here. The combination of the spectra is based on the standard Best Linear Unbiased Estimate (BLUE) algorithm [86] and yields the combination of the spectra in a common binning as well as the systematics accounted for correlations.

The ratio of every available reconstruction method to a TCM fit to the combined spectra is shown in Figure 6.14. The fit itself will be explained in the next section. The good agreement between the presented PCM method and the other reconstruction methods is worth noting. In addition, it can be seen that the PCM measurement provides for each combination the low p_{T} points as it is the only method that can reach very low in transverse momentum.

Two Component Model Fit

$\sqrt{s}$	Meson	A_e (pb GeV$^{-2}c^3$)	T_e (GeV)	A (pb GeV$^{-2}c^3$)	T (GeV)	n	χ^2/ndf
900 GeV	π^0	$(0.6\pm1.2)\times10^{9}$	0.551 ± 0.135	$(1.2\pm0.8)\times10^{11}$	0.354 ± 0.081	3.091 ± 0.789	2.12
7 TeV	π^0	$(2.9\pm0.2)\times10^{11}$	0.180 ± 0.004	$(2.1\pm0.2)\times10^{10}$	0.659 ± 0.012	3.098 ± 0.009	1.57
	η	$(2.1\pm3.1)\times10^{10}$	0.164 ± 0.105	$(3.7\pm1.6)\times10^{9}$	0.753 ± 0.086	2.920 ± 0.112	0.82
8 TeV	π^0	$(8.2\pm1.5)\times10^{11}$	0.136 ± 0.008	$(4.0\pm0.4)\times10^{10}$	0.591 ± 0.012	3.036 ± 0.008	1.92
	η	$(0.15\pm1.4)\times10^{9}$	0.665 ± 0.064	$(3.6\pm1.4)\times10^{9}$	0.753 ± 0.013	3.002 ± 0.027	1.27

Tsallis Fit

$\sqrt{s}$	Meson	C (pb)	T (MeV)	n	χ^2/ndf
900 GeV	π^0	$(10.16\pm1.61)\times10^{10}$	0.119 ± 0.010	7.372 ± 0.336	1.39
7 TeV	π^0	$(18.18\pm0.22)\times10^{10}$	0.135 ± 0.001	6.730 ± 0.015	2.93
	η	$(16.94\pm1.57)\times10^{9}$	0.240 ± 0.017	7.468 ± 0.392	0.81
8 TeV	π^0	$(23.95\pm0.53)\times10^{10}$	0.124 ± 0.001	6.552 ± 0.019	3.97
	η	$(25.18\pm2.69)\times10^{9}$	0.186 ± 0.008	6.745 ± 0.083	2.54

Table 12: Parameters of the TCM and Tsallis fits to the π^0 and η meson differential invariant yields.

6.4.2 Comparison to Theory

The combined spectra from the last section carry the whole physics information about the neutral mesons. In addition, the combined spectrum shows a perfect agreement with the PCM measurement as seen in Figure 6.14. Therefore, the combined spectra are used for comparisons to theory calculations in this section. For the comparison, the spectra are fitted with several functions whose sole purpose is the parametrization of the spectra in order to compare them to theory. The parametrizations include a Tsallis function, that was introduced in Section 6.2.4 as well as a two-component model (TCM) function that was proposed in [87]. The TCM function is a combination of a Boltzmann part at low transverse momentum and a power-law part at high p_{T}. This allows the function to describe the spectra over the full transverse momentum range. The functional form of the TCM is given by:

$$E\frac{\mathrm{d}^3\sigma}{\mathrm{d}p^3} = A_e \exp\left(-\frac{E_{\mathrm{T,kin}}}{T_e}\right) + A\left(1+\frac{p_{\mathrm{T}}^2}{T^2 n}\right)^{-n} \tag{25}$$

Here, $E_{\mathrm{T,kin}} = \sqrt{p_{\mathrm{T}}^2 + m^2} - M$ stands for the transverse kinetic energy of the meson with mass m. The parameters A and A_e represent normalization factors and T, T_e and n are free parameters.

The Tsallis function with the free parameters C, n and T is given as:

$$E\frac{\mathrm{d}^3\sigma}{\mathrm{d}p^3} = \frac{C}{2\pi}\frac{(n-1)(n-2)}{nT(nT+m(n-2))}\left(1+\frac{m_{\mathrm{T}}-m}{nT}\right)^{-n}, \tag{26}$$

An overview of the fit parameters for each fit function to the combined neutral meson spectra is given in Table 12.
The theory comparisons are done with NLO pQCD calculations using MSTW [88] parton distribution functions together with DSS14 [89] fragmentation functions for the neutral

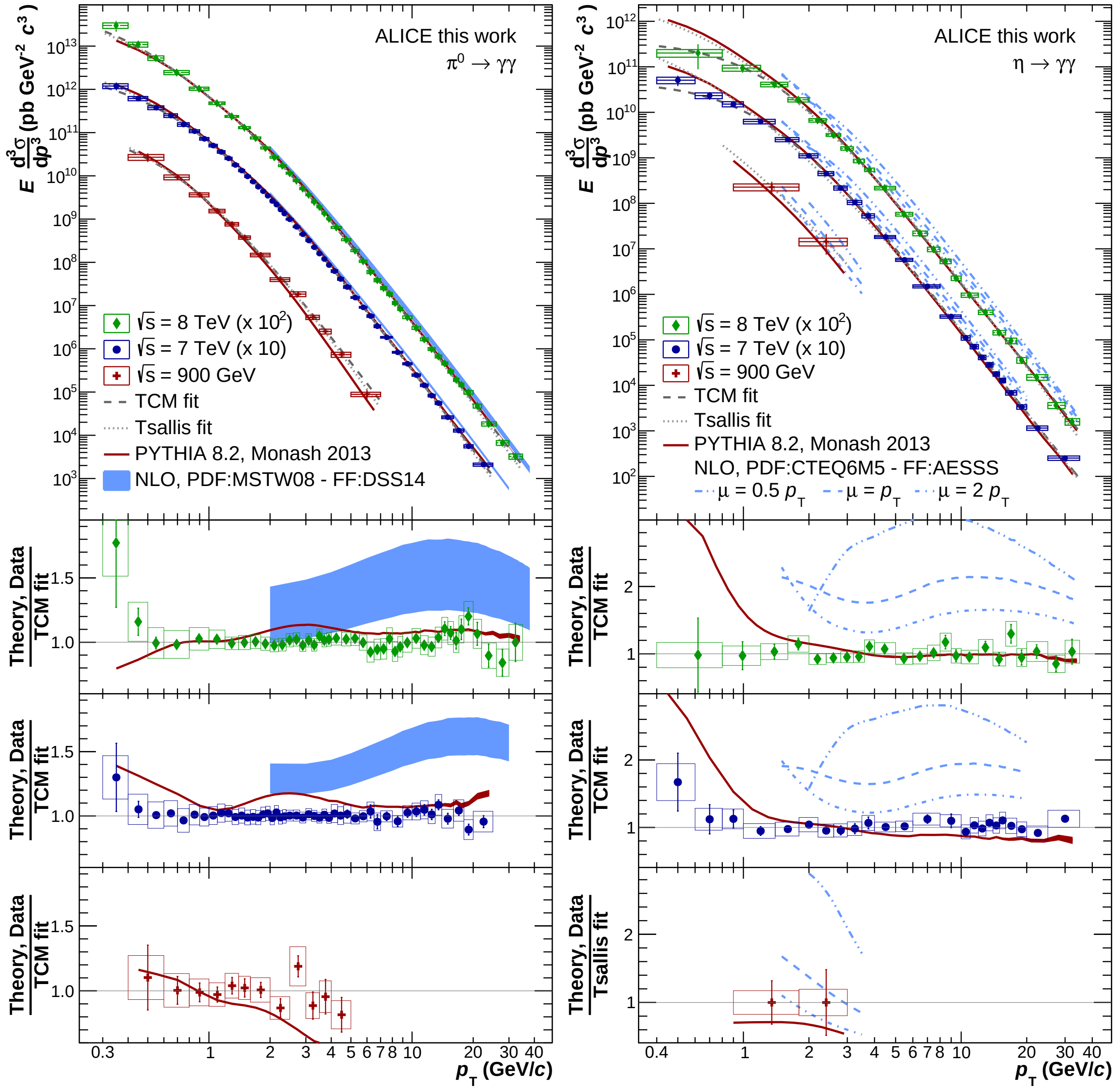

Figure 6.15: Differential invariant cross sections of the π^0 and η mesons in pp collisions at different energies as a function of the transverse momentum. The spectra are the combined measurements using the available reconstruction methods. Ratios of the spectra to their TCM fit as well as the ratio of the theory predictions to this fit are shown in the lower half.

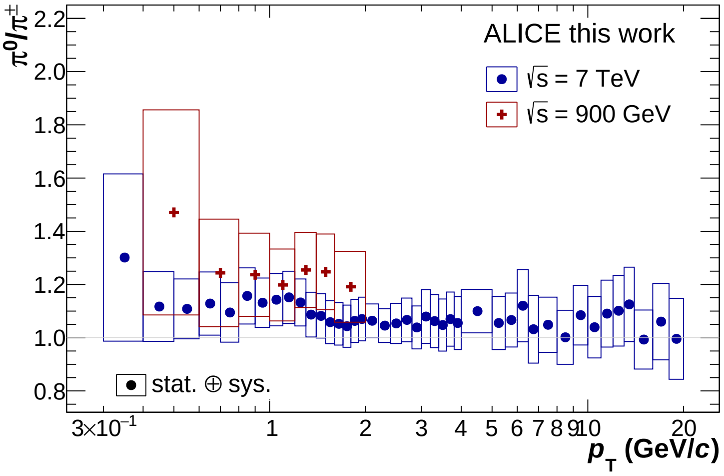

Figure 6.16: Comparison of the combined neutral pion measurements at $\sqrt{s} = 0.9$ and 7 TeV to the charged pion spectra. The error boxes represent the quadratic sum of statistical and systematical uncertainties of the measurements. The charged pion spectrum for this comparison is the average of the spectra of both charges.

pions and with AESSS [90] fragmentation functions for the η meson. For all NLO pQCD calculations, the same value range for μ of $0.5p_\mathrm{T} < \mu < 2p_\mathrm{T}$ is used for the factorization, renormalization and fragmentation. The ratios of pQCD calculations and data to the two-component function is shown in Figure 6.15 to check for the agreement between theory and actual measured result. It can be seen that for every value of μ the pQCD calculations overestimate the data by a significant amount.

Furthermore, a comparison to PYTHIA8.210 [91] with the Monash 2013 tune [92] is made for all measurements. As the measured data is, due to the applied correction, assumed to be clean of contaminations of long-lived strange particle decays (e.g. K^0_S and Λ), these decays were not included in the PYTHIA simulations. It can be seen that the Monash 2013 tune calculation is able to reproduce the $\sqrt{s} = 8$ TeV measurement very well over a wide transverse momentum range. The same behavior can be observed for the $\sqrt{s} = 7$ TeV measurement of both neutral mesons down to a transverse momentum of about 1.5 GeV/c. Due to the rather large uncertainties for the $\sqrt{s} = 900$ GeV measurements, the agreement between data and PYTHIA calculation is given within the uncertainties. However, it seems that for this center-of-mass energy the calculations assume a stronger falling spectrum.

6.4.3 Comparison to Charged Pions

The charged and neutral pion productions are expected to be similar due to isospin symmetry. In order to check for the agreement between the spectra, the averaged spectrum between both charges of the charged pions are compared to the measured π^0 yields. The resulting ratios for two center-of-mass energies is shown in Figure 6.16 where the uncertainties are the quadratic sum of the statistical and systematical uncertainties. For the $\sqrt{s} = 900$ GeV comparison, the published measurements from ALICE [72] are used. Despite the large uncertainties, a slight offset in the ratio towards a higher neutral pion yield can be seen.

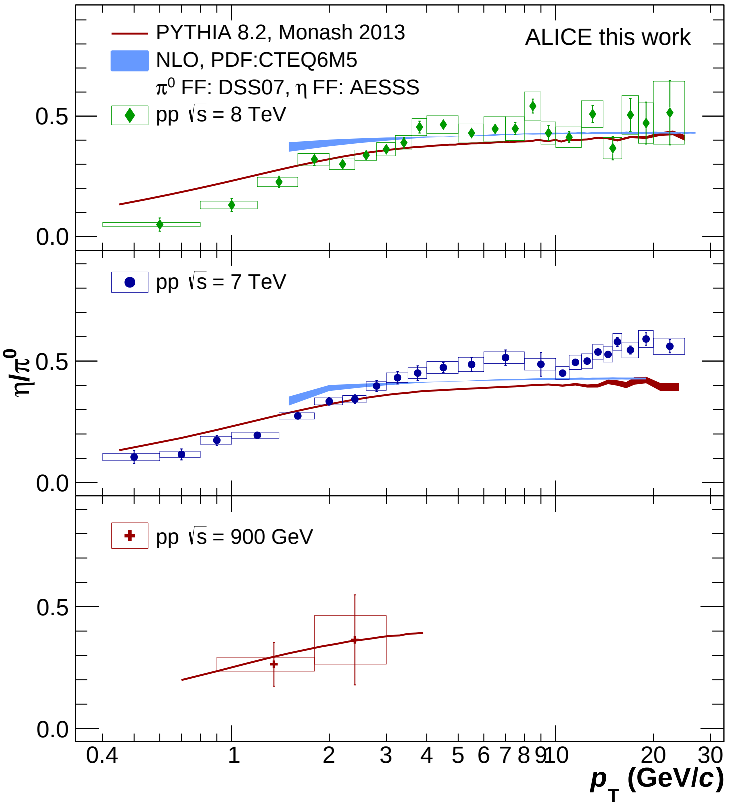

Figure 6.17: η/π^0 ratio in pp collisions at different energies as a function of the transverse momentum. The data is from the combined measurements at the respective center-of-mass energies and includes the systematic uncertainties. Theory calculations from PYTHIA8.2 with the Monash 2013 tune as well as pQCD NLO calculations for $0.5p_{\mathrm{T}} < \mu < 2p_{\mathrm{T}}$ are shown for comparison.

The comparison at $\sqrt{s} = 7$ TeV covers a very wide transverse momentum range as the charged pions spectra in the published ALICE measurements [93] have been measured up to 20 GeV/c. A good agreement between charged and neutral pions can be observed over the full transverse momentum range which provides additional proof for a good measurement of the π^0 mesons.

For the highest center-of-mass energy measurement at $\sqrt{s} = 8$ TeV no charged pion measurement is currently published. Therefore no comparison could be done for the neutral pions.

6.5 η/π^0 Ratio

The η/π^0 ratio provides additional insights into the particle production mechanisms. One property of this ratio is the cancellation of systematic uncertainties between both measurements as those uncertainties have the same influence on both spectra. Most important is the material budget uncertainty of 9% for PCM that cancels out as both spectra rely on the same Monte Carlo simulation. The η/π^0 ratios for all three center-of-mass energy measurements are shown in Figure 6.17 including the systematic uncertainties. The data points are the combination of the different reconstruction methods. The characteristic asymptotic behavior of the ratio can be observed with its increase in p_{T} until the flattening at $p_{\mathrm{T}} \approx 4$ GeV/c. This behavior is visible for the $\sqrt{s} = 7$ and 8 TeV measurement whereas the $\sqrt{s} = 900$ GeV measurements lacks data points as well as statistics. While the NLO calculations were not able to describe the π^0 and η spectra themselves, they do a much better job at describing the η/π^0 ratio. In addition, the PYTHIA8.2 calculation is shown for all three center-of-mass energy measurements with a fairly good agreement down to 1.5 GeV/c.

7 Direct Photon Analysis

In this chapter, the identified photon candidates from Section 5.4 are corrected to obtain the inclusive primary photons and in the end the direct photon signal. As introduced in Section 2.4, the direct photons are an important probe for the early collision stages. However, their extraction depends largely on a good understanding of the decay photons as well as a perfect correction of the inclusive photon yield.

7.1 Inclusive Photons

The fully corrected inclusive photon yield is obtained from the identified photon candidates by applying several corrections to the raw photon yield shown in Figure 7.1. The raw yield is normalized by the number of events given in Table 2. The following sections cover the corrections of the photon candidates, the systematic error evaluation and the final inclusive photon spectrum as well as the inclusive γ/π^0 ratio.

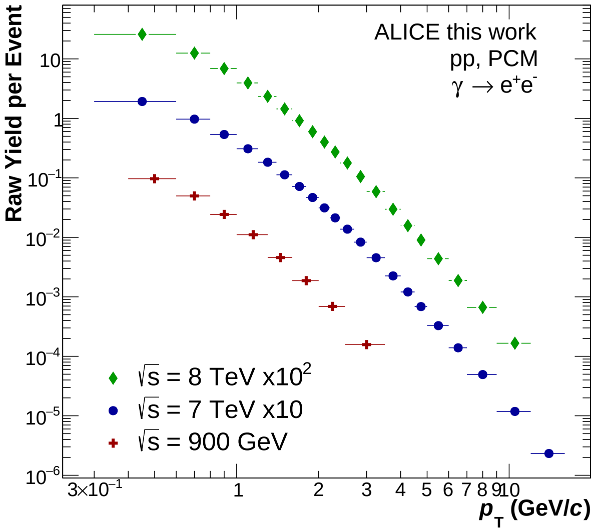

Figure 7.1: Inclusive photon raw yield per event for the three center-of-mass energy measurements.

7.1.1 Inclusive Spectrum Corrections

The corrections of the inclusive photon raw yield include the detection efficiency, the resolution, secondary decay photons, the conversion probability and out-of-bunch pileup. Most correction factors are obtained from the Monte Carlo simulations due to the additional information they provide. However, for the secondary photons a data driven approach using a cocktail simulation is used. In the following part, each correction will be explained in detail:

7.1.1.1 Out-Of-Bunch Pileup

The necessity of the out-of-bunch pileup correction was already discussed in Section 6.2.1 and will not be further mentioned in this section. Instead the focus is set on how the

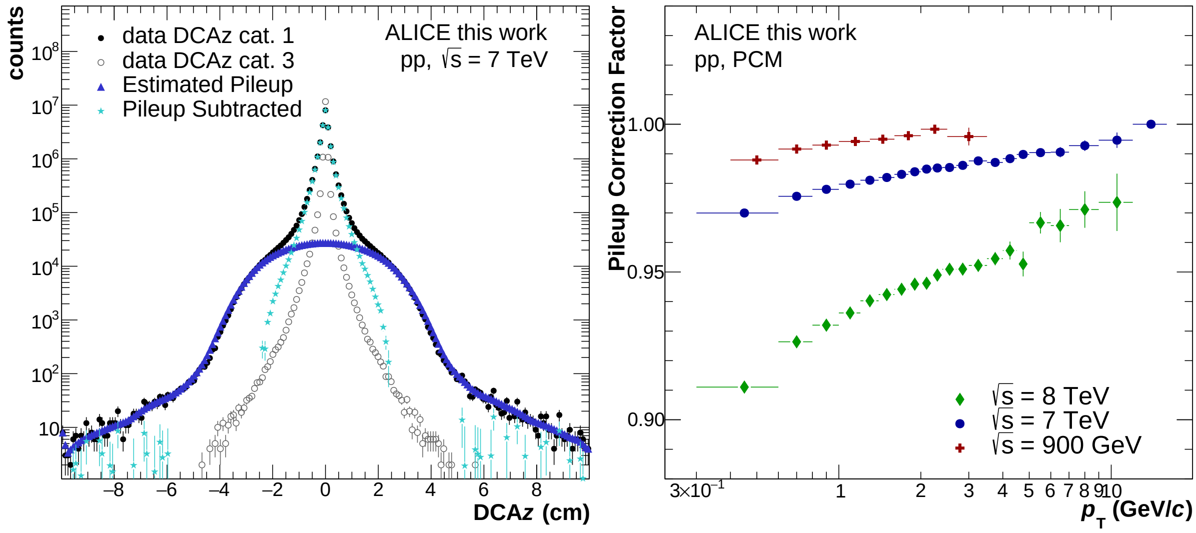

Figure 7.2: Left: Transverse momentum integrated DCAz distribution of category 1 and category 3 track pairs including the background fit. **Right:** Out-of-bunch pileup correction factor for the three center-of-mass energy photon measurements.

correction factor is obtained for the photons. The three established photon categories based on their track information provided by TPC or ITS are the same as before; category 1 where both tracks are TPC only based, category 2 where additional information for one track is provided by the ITS and category 3 where both tracks are based on both, ITS and TPC. The last category is expected to not show any pileup contribution due to the good primary vertex resolution and therefore rejection of pileup events. Both other categories, however, will show pileup contributions as their photon conversion points are shifted in z-direction due to the additional drift time the out-of-bunch pileup events have. Similar to the neutral meson pileup estimation the DCAz distribution is used as it shows this shift of conversion points as a broadening of the legs of the distribution.
The p_{T} integrated DCAz distributions for the category 1 and category 3 photons is shown in Figure 7.2. The broadening of the distribution legs towards larger DCAz is visible. In addition, the background description using the "ShowBackground" function as well as the pileup subtracted DCAz distribution are shown. The function nicely describes the background and serves as the pileup estimation under the peak. The pileup subtracted distribution that is given by the light blue points shows a much sharper peak without the wide legs. For comparison, the category 3 distribution is also shown in Figure 7.2. This shows that the DCAz distribution without pileup should be very narrow around DCA$z = 0$. The remaining difference between the pileup subtracted peak and the category 3 peak is due to the much better tracking resolution of the ITS detector system compared to the TPC only vertex reconstruction.

The pileup correction factor is calculated by comparing the pileup subtracted distributions from category 1 and category 2 to their original distributions. As there is no pileup expected for category 3, no pileup estimation is made for it. The correction factor is calculated with the following formula:

$$F_{\text{pileup}}(p_{\mathrm{T}}) = \frac{\gamma^{\text{cat 1}}_{\text{subtracted}}(p_{\mathrm{T}}) + \gamma^{\text{cat 2}}_{\text{subtracted}}(p_{\mathrm{T}}) + \gamma^{\text{cat 3}}_{\text{all}}(p_{\mathrm{T}})}{\gamma^{\text{cat 1}}_{\text{all}}(p_{\mathrm{T}}) + \gamma^{\text{cat 2}}_{\text{all}}(p_{\mathrm{T}}) + \gamma^{\text{cat 3}}_{\text{all}}(p_{\mathrm{T}})} \tag{27}$$

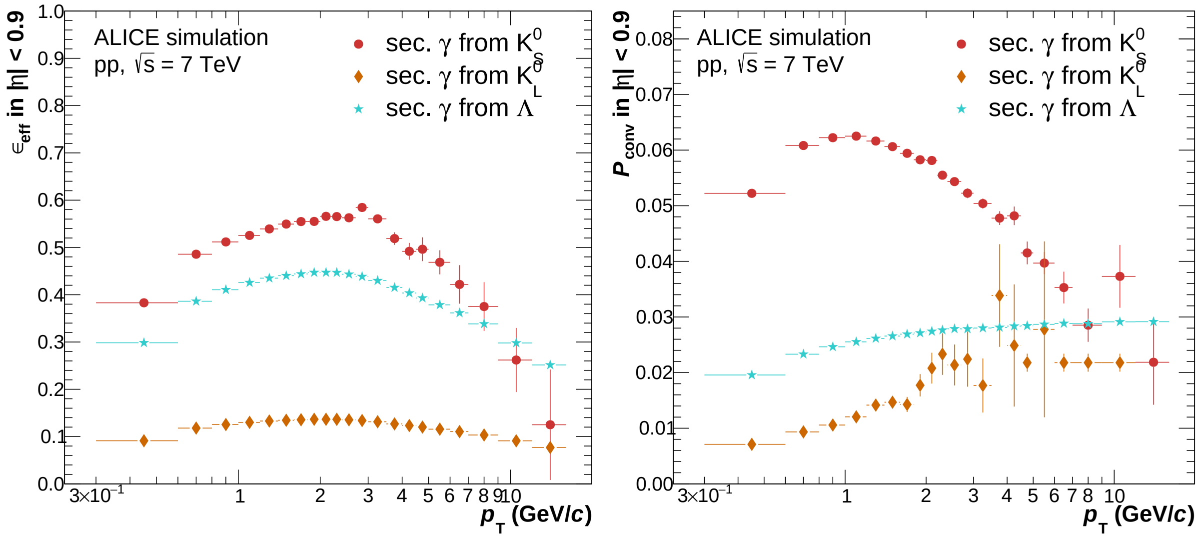

Figure 7.3: Left: Reconstruction efficiency for secondary photons coming from K^0_S, K^0_L and Λ decays. **Right:** Conversion probabilities of the secondary photons from K^0_S, K^0_L and Λ decays. Both plots show the points obtained from the $\sqrt{s} = 7$ TeV Monte Carlo simulation.

Here, the subscript "subtracted" stands for the pileup subtracted photons in the respective categories. The calculated out-of-bunch pileup correction factors for the three center-of-mass energy measurements are shown in Figure 7.2. This shows the expected behavior of the correction factor with increasing interaction rate as the $\sqrt{s} = 8$ TeV correction factor is the largest reaching up to 9% at low p_{T}. The correction in the $\sqrt{s} = 900$ GeV measurement on the other hand is with $\approx 1\%$ very small.

7.1.1.2 Secondary Decay Photons

The secondary correction for the inclusive photons follows a similar approach as for the neutral pion secondaries. In case of the photons, secondaries are considered to be all those photons that do not originate from the primary vertex or from primary particles. A large portion of these photons comes from the decay $K^0_S \rightarrow \pi^0\pi^0 \rightarrow 4\gamma$. Additional sources are secondary photons coming from the weak decays of K^0_L and Λ. However, they are strongly suppressed due to their long lifetime and therefore the improbability of the reconstruction of their decay products in the TPC.

For the correction the same cocktail decay simulation as for the neutral pion secondary correction is used. For this, the measured K^0_S, K^0_L and Λ spectra, as explained in Section 6.2.2.1 are used as input. The mother particles are then produced flat in p_{T} and afterwards the particle decays are simulated using PHYTHIA 6.4. The resulting mother and daughter spectra are then weighted with the parametrized input spectra which leads to the secondary photon distributions being obtained as fully corrected spectra. As the secondaries need to be subtracted from the raw yield, the detector response is folded onto the spectra using the reconstruction efficiencies and conversion probabilities for the secondary photons that are obtained from the full Monte Carlo simulations. Efficiency and conversion probability calculations are explained in Section 7.1.1.4 and Section 7.1.1.5 respectively. The resolution correction for the secondary spectra is obtained from the

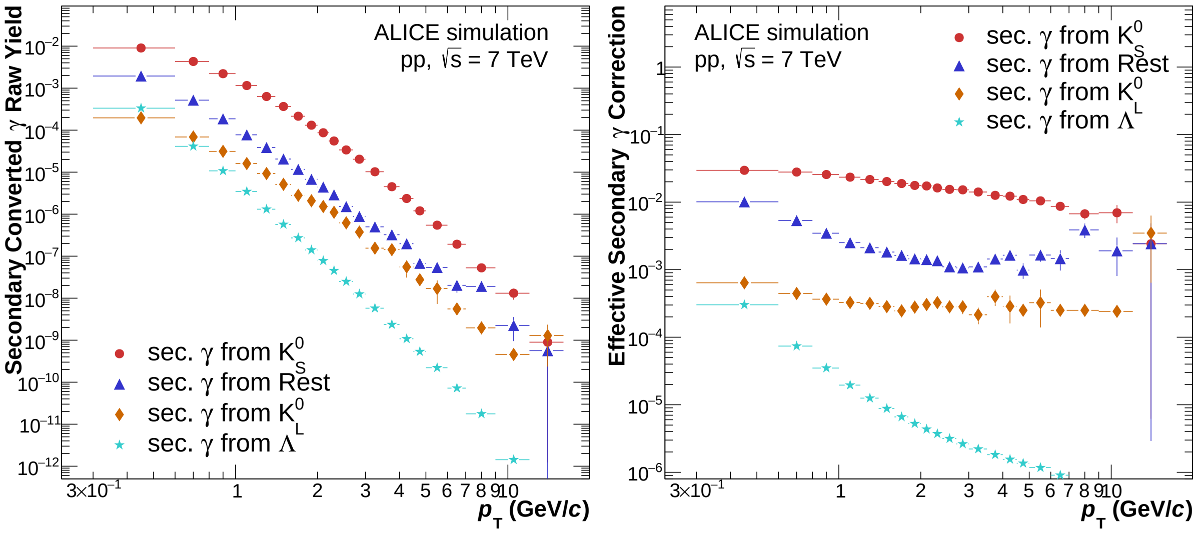

Figure 7.4: Left: Raw yields for secondary photons coming from K^0_S, K^0_L and Λ decays. **Right:** Fractions of secondary photons from K^0_S, K^0_L and Λ decays to the measured raw photon spectrum. Points shown are obtained from the $\sqrt{s} = 7$ TeV simulations.

Monte Carlo simulations and included in the efficiency correction.
However, the limited statistics of the Monte Carlo simulations do not allow the extraction of the efficiencies and conversion probabilities for the K^0_L and Λ until the maximum transverse momentum necessary. Therefore, the efficiencies in Monte Carlo for both particles are fitted. The fit is then used to obtain a scaled down version of the primary reconstruction efficiency. This can be done as the shape of the primary efficiency and secondary efficiencies is assumed to be similar. The conversion probability is assumed to level out towards large transverse momenta and is therefore fitted with a constant in the high p_{T} region. The constant value is then assumed for all transverse momentum bins that are not described due to the limited Monte Carlo simulation statistics. The smoothed reconstruction efficiencies as well as the plateau in conversion probabilities obtained from Monte Carlo can be seen in Figure 7.3. The same quantities for the other center-of-mass energy measurements can be found in the appendix in Figure C.11. Both figures illustrate the strong difference between K^0_S and K^0_L due to the different decay lengths. The much larger decay length of the K^0_L results in a much smaller reconstruction efficiency and conversion probability as it is very unlikely that the K^0_L decays inside or in front of the TPC. In addition, this has the consequence that for the late decays there is much less material for the conversions of the photons and therefore a smaller conversion probability.

In order to obtain the raw secondary photon spectra for the correction, the decay simulation spectra need to be multiplied with their reconstruction efficiencies as well as their conversion probabilities. The resulting raw secondary photon yields from K^0_S, K^0_L and Λ are then subtracted from the measured photons. Figure 7.4 shows the secondary photon raw yield as well as the fraction of secondary photons from the different sources to the measured photon raw yield for the $\sqrt{s} = 7$ TeV measurement. The same quantities from the two other center-of-mass energy measurements can be found in the appendix in Figure C.12. This shows that the secondary photons from K^0_S decays are the most significant source whereas the other particles contribute at least one order of magnitude less to the

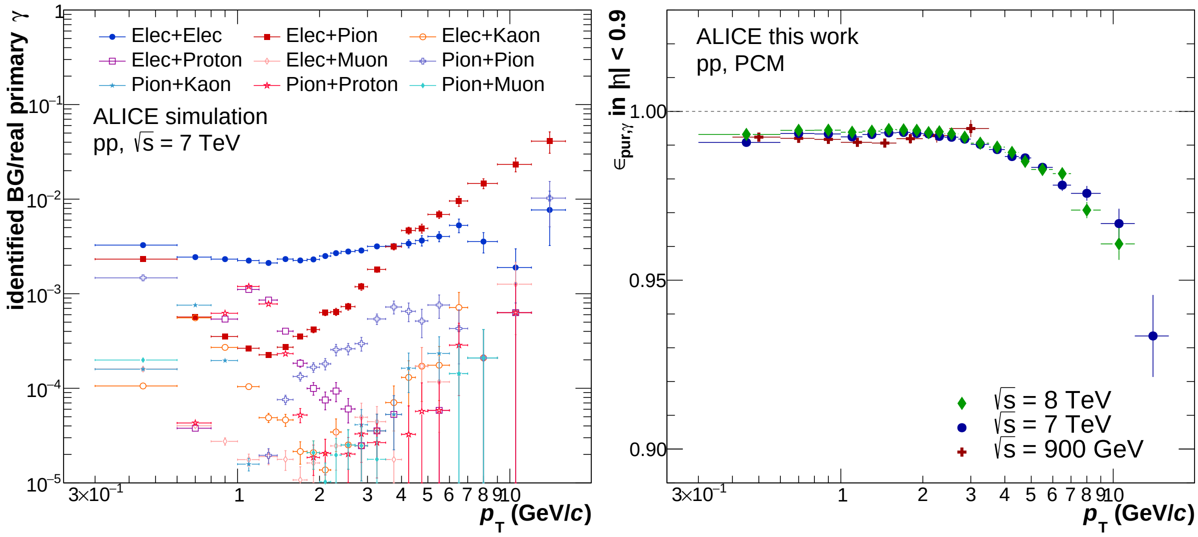

Figure 7.5: Left: Monte Carlo based ratio of different photon background sources to the real primary photons at $\sqrt{s} = 7$ TeV. The pairs contain both possible charge combinations. **Right:** Photon purity for the three center-of-mass energy measurements.

total photon yield. The category "Rest" is similar to the neutral pion secondary correction and contains mostly material interactions. It is obtained directly from the Monte Carlo simulations which include the full detector simulation.

7.1.1.3 Purity

The fraction of real photons to the identified V^0 sample is defined as the photon purity. It therefore serves as a measure for the contamination of the photon sample. The photon selection cuts remove as much of the contamination as possible while still maintaining a large efficiency. A nearly perfect purity would only be achievable by sacrificing a lot of statistics which is not reasonable for this measurement. The remaining contamination after the cut applications is mostly composed of random track combinations where the tracks originate from two different secondary vertices. Having passed the selection cuts, those track pairs show a similar topology as the photon conversion pairs and are mostly composed of random e^+e^- pairs, electron pairs or pion-pion pairs.

Using the additional information provided by the Monte Carlo simulations it is possible to visualize the different sources of the photon background. For this, the MC based ratio of identified background sources to the real primary photons is shown in Figure 7.5. It shows that the dominant contribution at low transverse momentum is made of false e^+e^- pairs, whereas towards higher p_T the electron-pion contamination takes over.

The purity is calculated for each center-of-mass energy spectrum after the secondaries from the last section have been subtracted. The calculation is fully based on Monte Carlo spectra and done using the following formula:

$$\epsilon_{\mathrm{pur},\,\gamma}(p_\mathrm{T}) = \frac{\gamma^{\mathrm{MC,\,true}}_{\mathrm{rec.\ prim.}}(p_\mathrm{T})}{\gamma^{\mathrm{MC,\,all}}_{\mathrm{rec}}(p_\mathrm{T}) - \gamma^{\mathrm{MC,\,true}}_{\mathrm{rec.\ sec.}}(p_\mathrm{T})} \tag{28}$$

For this, the photon spectra are reconstructed from the MC simulation and in addition they are validated to be true photons. The ratio therefore compares the true primary pho-

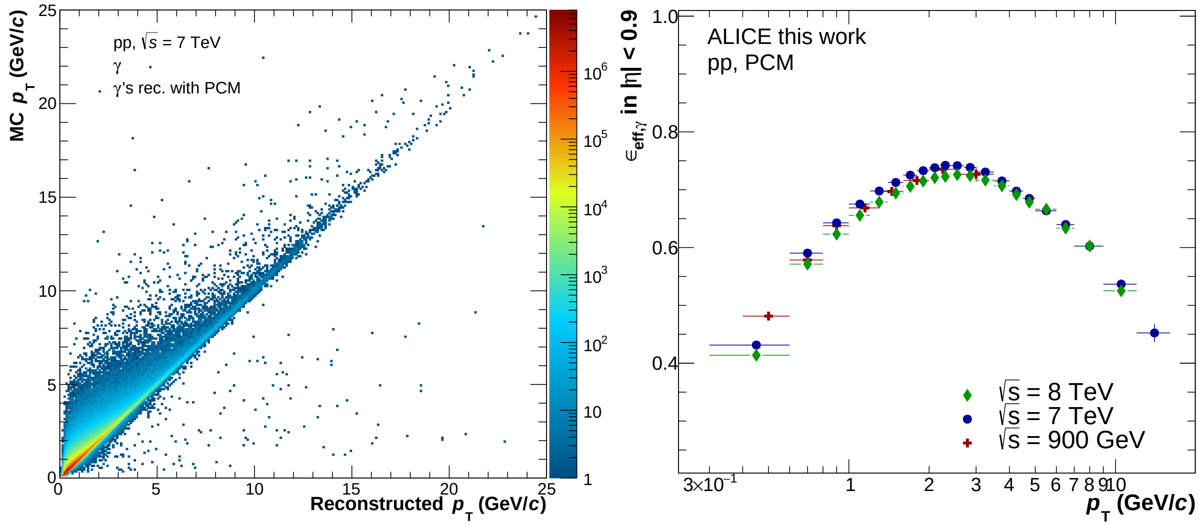

Figure 7.6: Left: The detector response matrix from the $\sqrt{s} = 7$ TeV Monte Carlo simulation. **Right:** Reconstruction efficiencies for the three center-of-mass energy measurements.

tons of the reconstructed spectrum to all reconstructed photons without the secondaries. This allows the purity to estimate the contamination in the reconstructed spectrum based on the Monte Carlo simulation. The purities of all three center-of-mass energy measurements are shown in Figure 7.5. For all measurements a 99% purity until 3 GeV/c in transverse momentum can be observed. Above 3 GeV/c the contamination from electron-pion pairs strongly increases which leads to a decrease in purity down to 94%.

7.1.1.4 Efficiency

The reconstruction efficiency corrects the measured spectrum for the loss of conversion pairs due to limited reconstruction and detector performance. In addition, it corrects for differences in the particle transverse momentum distributions in data and Monte Carlo. Such differences arise from limited detector resolution and electron bremsstrahlung. The efficiency correction is therefore applied in two steps; first the transverse momentum of the photons is converted to the real photon momentum by using Bayesian unfolding with the detector response. After that, the reconstruction efficiency is applied to correct for the remaining detector effects.

The unfolding for the conversion of measured p_T to the true transverse momentum is done using the detector response matrix which is shown in Figure 7.6. The matrix shows the effect of bremsstrahlung with the shift of points towards p_T^{MC}. As a consequence of the bremsstrahlung the photons are reconstructed with a lower momentum than they were actually produced. For the unfolding itself the RooUnfold package [94, 95] is used. With this package it is possible to use a Bayesian approach instead of the direct inversion of the response matrix which is a strongly statistically limited method. Instead the detector response is unfolded in several iterations where the initial distribution is given as the true transverse momentum from Monte Carlo and each subsequent iteration uses the last distribution as input.

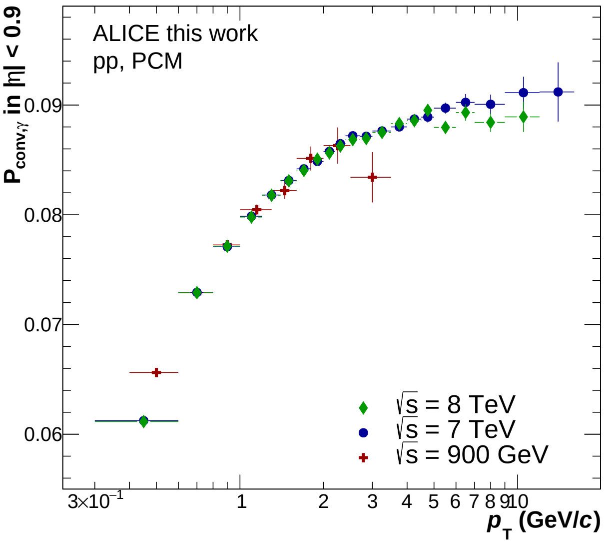

Figure 7.7: Photon conversion probabilities obtained from Monte Carlo simulations for the three measurements inside the pseudorapidity range of $|\eta| < 0.9$.

The reconstruction efficiency is then calculated as a function of the true transverse momentum by dividing the reconstructed Monte Carlo validated photon spectrum by all conversion photons from the simulation. This will also include the detector material conversion in the efficiency. The calculation is as follows:

$$\epsilon_{\text{eff, }\gamma}(p_{\text{T}}^{\text{true}}) = \frac{\gamma_{\text{rec. prim}}^{\text{MC, true}}(p_{\text{T}}^{\text{true}})}{\gamma_{\text{all prim}}^{\text{MC, conv}}(p_{\text{T}}^{\text{true}})} \tag{29}$$

Figure 7.6 shows the reconstruction efficiencies for all three center-of-mass energy measurements obtained from the unfolding method. Similar to the neutral meson efficiencies the drop towards low p_{T} is due to the conversion products either not reaching the TPC or them not passing a minimum radial distance inside the TPC. The decrease at high transverse momentum comes from dead areas in the TPC where the conversion products cannot be reconstructed as they do not bend enough in the magnetic field due to their high momentum.

7.1.1.5 Conversion Probability

The PCM measurements are based on the conversion of the photons into e^+e^- pairs. However, the probability for the conversion in the detector depends on the amount of material that can be crossed by the photons. For this analysis, the most amount of material with small radiation lengths is given by the beam pipe as well as the Inner Tracking System. The TPC gas, however, has a very long radiation length and therefore most conversions will happen in front of the TPC. Calculation of the conversion probability is fully based on the Monte Carlo simulations and also depends on how well the detector material is reproduced in the simulation. It is calculated with the following formula:

$$P_{\text{conv, }\gamma}(p_{\text{T}}^{\text{true}}) = \frac{\gamma_{\text{prim}}^{\text{MC, conv}}(p_{\text{T}}^{\text{true}})}{\gamma_{\text{prim}}^{\text{MC, all}}(p_{\text{T}}^{\text{true}})} \tag{30}$$

The conversion probability is therefore the ratio of converted photons to all photons in

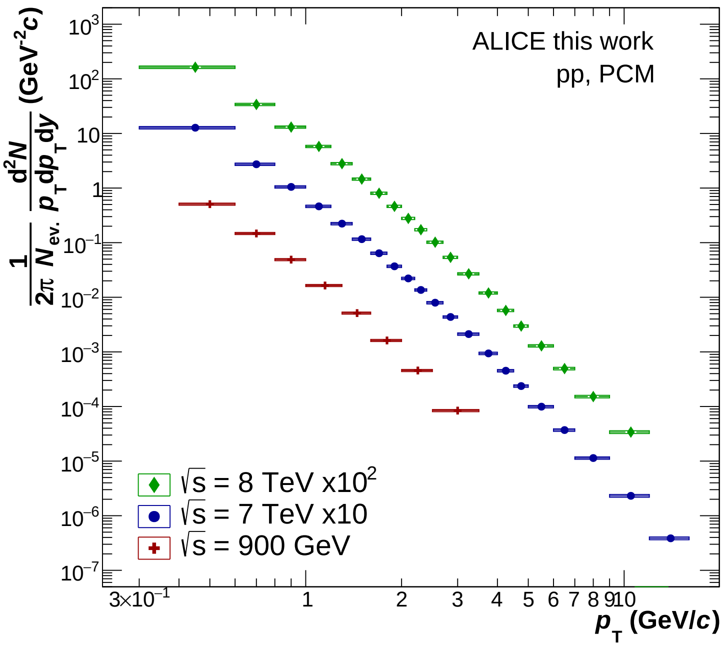

Figure 7.8: Fully corrected primary inclusive photon yields including systematic uncertainties for the three center-of-mass energy measurements.

the given pseudorapidity range. Figure 7.7 shows the calculated conversion probabilities for all three center-of-mass energy measurements. It can be seen that for large transverse momenta it levels out to about 9% whereas towards low p_T a drop in probability is visible. This drop originates from the increasing importance of Compton scattering at low photon energies.

7.1.2 Inclusive Photon Spectrum

The application of all corrections on the raw photon spectrum results in the fully corrected primary inclusive photon spectrum. At first, the pileup correction is applied to the inclusive photon raw yield. Afterwards, the secondary photons are subtracted and on the resulting yield the remaining corrections are applied. They include the correction for efficiency, detector response, purity as well as the conversion probability. The correction is calculated with the following formula:

$$\gamma^{\mathrm{incl}}_{\mathrm{corr}}(p_\mathrm{T}) = \left(F_{\mathrm{pileup}}(p_\mathrm{T}) \times \gamma^{\mathrm{incl}}_{\mathrm{raw}}(p_\mathrm{T}) - \sum_{\mathrm{K0_S,K0_L,\Lambda,Rest}} \gamma^{\mathrm{sec}}_{\mathrm{raw}}(p_\mathrm{T}) \right) \times \frac{\epsilon_{\mathrm{pur}}(p_\mathrm{T})}{\epsilon_{\mathrm{eff}}(p_\mathrm{T})} \times \frac{1}{P_{\mathrm{conv}}(p_\mathrm{T})} \tag{31}$$

The resulting spectrum is therefore the p_T dependence of all primary photons which were produced in the pseudorapidity region of $|\eta| < 0.9$ and 2π in azimuth. The invariant yield can now be obtained by normalizing to the number of events and the following formula:

$$E\frac{\mathrm{d}^3N_\gamma}{\mathrm{d}p^3} = \frac{\mathrm{d}^3N_\gamma}{p_\mathrm{T}\mathrm{d}p_\mathrm{T}\mathrm{d}y\mathrm{d}\phi} = \frac{1}{2\pi N_{\mathrm{event}}} \frac{\gamma^{\mathrm{incl}}_{\mathrm{corr}}(p_\mathrm{T})}{\Delta y \Delta p_\mathrm{T}} \tag{32}$$

The number of events for the normalization is given in Table 2 and the fully corrected primary inclusive photon yields are shown in Figure 7.8 for the three center-of-mass energy

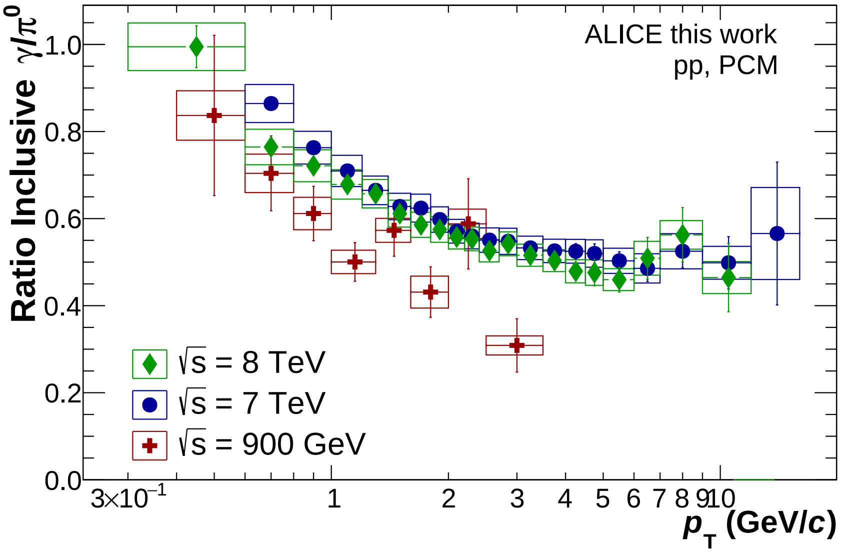

Figure 7.9: Inclusive γ/π^0 ratio including systematic uncertainties for the three center-of-mass energy measurements.

measurements including systematic uncertainties. An overview of the detailed systematic uncertainties is provided in the appendix in Figure C.14, Figure C.15 and Figure C.16 for all photon related measurements. The transverse momentum reach is the same as for the neutral pions and ranges from a minimum of 0.3 GeV/c up to 16 GeV/c for the $\sqrt{s} = 7$ TeV measurement.

In addition, the inclusive ratio of neutral pions and photons can be calculated. This ratio will be important for the direct photon extraction in the next section. The γ/π^0 ratios for the three center-of-mass energy measurements are shown in Figure 7.9 including the systematic uncertainties.

7.2 Direct Photon Extraction

This section introduces the decay photon cocktail as well as the direct photon excess ratio and spectrum. For the direct photon extraction all results from the previous section are required as input, including their systematic uncertainties. A general introduction to direct photons has been given in Section 2.4 and this section will further explain the extraction method.

7.2.1 Decay Photon Cocktail

In order to extract the direct photons it is mandatory to subtract the contribution from electromagnetic decays from the inclusive sample. As it is not possible to determine the decay photons from data, a decay simulation is used which is based on the parametrizations of a multitude of different measured particle spectra [96]. Measurements of kaons, charged pions, lambda baryons and protons have been performed at each of the three center-of-mass energies in ALICE and are used in addition the the neutral meson measurements from this analysis for the generation of the cocktail. An overview of the mother particles included in the decay photon cocktail simulation is shown in Table 13, including the relevant branching ratios for decays into photons which are taken from the PDG [97]. As the cocktail is also used for the determination of the secondary contribution of the neutral pions, the relevant branching ratios for the decays from K^0_S, K^0_L and Λ are also included in the table. However, several cocktail ingredients have not been measured directly and are therefore produced from transverse mass (m_{T}) scaling from the π^0 parametrization for mesons and the proton parametrization for baryons. Transverse mass scaling exploits the fact that the spectra of different particle species are only shifted by a constant factor when expressed as a function of $m_{\mathrm{T}} = \sqrt{p_{\mathrm{T}}^2 + m^2}$, where m denotes the particle's mass. With this it is possible to calculate the spectrum of any meson or baryon of species X, based on the neutral pion or proton parametrization using the following formula:

$$E\frac{\mathrm{d}^3N^X}{\mathrm{d}p^3} = C_{m_{\mathrm{T}}} \cdot P_{\pi^0/p}(m_{\mathrm{T}}) \tag{33}$$

Here, $C_{m_{\mathrm{T}}}$ denotes the constant scaling factor that has to be determined experimentally and is listed in Table 13. It originates from the constant ratio factor of the particle spectra at high transverse momentum and is obtained from measurements or PYTHIA simulations. The parametrization of the neutral pion or proton spectrum is given by $P_{\pi^0/p}$ as a function of transverse mass of particle X.

While the neutral meson spectra are measured in this thesis and taken as input for the cocktail simulation, other spectra are taken from external sources. The proton spectra are taken from the corresponding publication for each center-of-mass energy [72–74]. However, for the $\sqrt{s} = 8$ TeV case there are no publications on proton production available and therefore an extrapolated spectrum using the 2.76 TeV and 7 TeV spectra as proxies is used [77]. The proton itself is no direct source for decay photons or secondary particles, but it is used as the reference spectrum for the m_{T} scaling of the Δ^0, Δ^+ and Σ^0 baryons.

7.2.1.1 Input Spectra Parametrization

The parametrization of the input spectra is of great importance for a reliable decay photon cocktail. It is necessary as the particle spectra only provide a limited transverse momentum reach towards low and high p_{T}. The fit functions used to describe the spectra are chosen to best describe the observed spectrum over the full measured transverse momentum range and hence do not necessarily employ physical models for the description.

The neutral pion spectrum is ideally described by a modified Hagedorn function is used as it describes the measured spectrum the best possible way. This function was proposed by the PHENIX collaboration and is given by:

$$E\frac{\mathrm{d}^3N}{\mathrm{d}p^3} = A \cdot \left[exp\left(ap_{\mathrm{T}} + bp_{\mathrm{T}}^2\right) + \frac{p_{\mathrm{T}}}{p_0} \right]^{-n} \tag{34}$$

This functional form is also used for the description of the measured charged pion, K^0_S, K^0_L, Λ and proton spectra with the only difference being the multiplication with transverse momentum to improve the high p_{T} tail description.

particle	mass (MeV)	C_{m_T}	measurement			decay	branching ratio
			900 GeV	7 TeV	8 TeV		
π^0	134.98	-	– this thesis –			$\gamma\gamma$	9.882×10^{-01}
						$e^+e^-\gamma$	1.174×10^{-02}
η	547.85	-	– this thesis –			$\gamma\gamma$	3.941×10^{-01}
						$\pi^0\gamma\gamma$	2.560×10^{-04}
						$\pi^+\pi^-\gamma$	4.220×10^{-02}
						$e^+e^-\gamma$	6.899×10^{-03}
						$\mu^+\mu^-\gamma$	3.090×10^{-04}
η'	957.66	0.40	m_T scaling			$\rho^0\gamma$	2.908×10^{-01}
						$\omega\gamma$	2.746×10^{-02}
						$\gamma\gamma$	2.198×10^{-02}
						$\mu^+\mu^-\gamma$	1.080×10^{-04}
ω	782.65	-	[98]			$\pi^0\gamma$	8.350×10^{-02}
						$\eta\gamma$	4.600×10^{-04}
						$\pi^0\pi^0\gamma$	7.000×10^{-05}
ρ^0	775.49	1.00	m_T scaling			$\pi^+\pi^-\gamma$	9.900×10^{-03}
						$\pi^0\gamma$	6.000×10^{-04}
						$\eta\gamma$	3.000×10^{-04}
						$\pi^0\pi^0\gamma$	4.500×10^{-05}
ρ^+	775.49	1.00	m_T scaling			$\pi^+\gamma$	4.500×10^{-04}
ρ^-	775.49	1.00	m_T scaling			$\pi^-\gamma$	4.500×10^{-04}
ϕ	1019.46	-	[99]			$\eta\gamma$	1.310×10^{-02}
						$\pi^0\gamma$	1.273×10^{-03}
						$\pi^+\pi^-\gamma$	4.100×10^{-05}
						$\pi^0\pi^0\gamma$	1.130×10^{-04}
						$\pi^0\eta\gamma$	7.300×10^{-05}
						$\eta'\gamma$	6.300×10^{-05}
						$\mu^+\mu^-\gamma$	1.400×10^{-05}
Δ^0	1232.00	1.00	m_T scaling of proton			$n\gamma$	6.000×10^{-03}
Δ^+	1232.00	1.00	m_T scaling of proton			$p\gamma$	6.000×10^{-03}
Σ^0	1192.64	0.49	m_T scaling of proton			$\Lambda\gamma$	$1.000 \times 10^{+00}$
K^0_S	497.61	-	[72]	[100]	[74, 100]	$\pi^+\pi^-\gamma$	1.787×10^{-03}
						$\pi^0\pi^0$	3.065×10^{-01}
K^0_L	497.61	-	[72]	[100]	[74, 100]	$\pi^\pm e^\mp \nu\gamma$	3.988×10^{-03}
						$\pi^\pm \mu^\mp \nu\gamma$	4.920×10^{-04}
						$\pi^+\pi^-\gamma$	4.200×10^{-05}
						$\gamma\gamma$	5.500×10^{-04}
						$\pi^0\pi^0\pi^0$	1.946×10^{-01}
						$\pi^+\pi^-\pi^0$	1.250×10^{-01}
						$\pi^0\pi^0$	8.630×10^{-04}
Λ	1115.68	-	[101]	[100]	[74, 100]	$n\gamma$	8.400×10^{-04}
						$n\pi^0$	3.580×10^{-01}

Table 13: Mother particles included in decay simulation.

For the η meson a Tsallis function [75] as introduced in Section 6.2.4 is used as it provides the best possible spectrum description.

7.2.1.2 Particle Decay Simulation

The decay particle spectra are obtained from a decay simulation of randomly generated mother particles from the list of mother particles given in Table 13. The generation of the mother particles is done flat in the transverse momentum range of $0\ \mathrm{GeV}/c \leq p_\mathrm{T} \leq 50\ \mathrm{GeV}/c$ and for the rapidity range of $|y| < 1.0$ as well as the full azimuth of $0 < \phi < 2\pi$. The parametrizations are then applied as a weight on the transverse momentum spectrum to reduce statistical fluctuations and improve the reach towards higher transverse momenta. For each decay simulation a total of one million events with 1000 particles per species and event are generated. This ensures that there are no contributions to statistical uncertainties coming from the decay photons or secondary neutral pions.
The spectra for all generated mother particles from the decay simulation at $\sqrt{s} = 7$ TeV as well as the ratio of the mother particle spectra to the neutral pion or proton spectrum are shown in Figure 7.10. The neutral pion is the most dominant mother particle at low transverse momenta. However, towards high p_T the contributions from the transverse mass scaled spectra with $C_{m_\mathrm{T}} = 1$, i.e. the ρ^0 and $\rho^\pm$, become similar to the neutral pion. In addition, the ratio plot visualizes the effect of the m_T scaling on the spectra as they approach the value of C_{m_T} towards high transverse momentum.

The PYTHIA 6.4 decayer is used to simulate the decays of the generated mother particles. For this, the branching ratios as listed in Table 13 are used and the full decay chain for each particle is simulated. This allows the cocktail to be used for the secondary correction as well as the extraction of the decay photon spectrum. However, in the case of the decay photons, only the direct decays from primary particles are used. In order to use the decay spectra for the analysis, the rapidity range is cut after the decay simulation to the range used in the analysis. This ensures that particles on the edges of the fiducial zone are correctly accounted for and that they are included in the cocktail.

The decay photon spectra are obtained from the PYTHIA decayer where the input parametrizations are used as weights. All spectra are shown in Figure 7.11 for the different decay photon sources. In addition, the fraction of the decay photons from the different sources to the full decay photon cocktail is also shown in the figure. With a fraction of about 80% the neutral pion is the dominant source of decay photons followed by the η meson with $\approx 10\%$ contribution. The ω and η' also contribute a non-negligible amount to the decay photon cocktail, whereas the remaining particles make at least one order of magnitude less impact on the total decay photons.

For the calculation of the direct photon excess ratio in the next section, not only the decay photon cocktail is used. Instead, it is normalized by the generated neutral pion spectrum. It is therefore important that the neutral pions are correctly simulated in the cocktail as an increased pion yield would translate into an increase of the decay photon yield. This would distort the direct photon spectrum in case the cocktail neutral pion spectrum shows significant differences to the measured neutral pion spectrum that

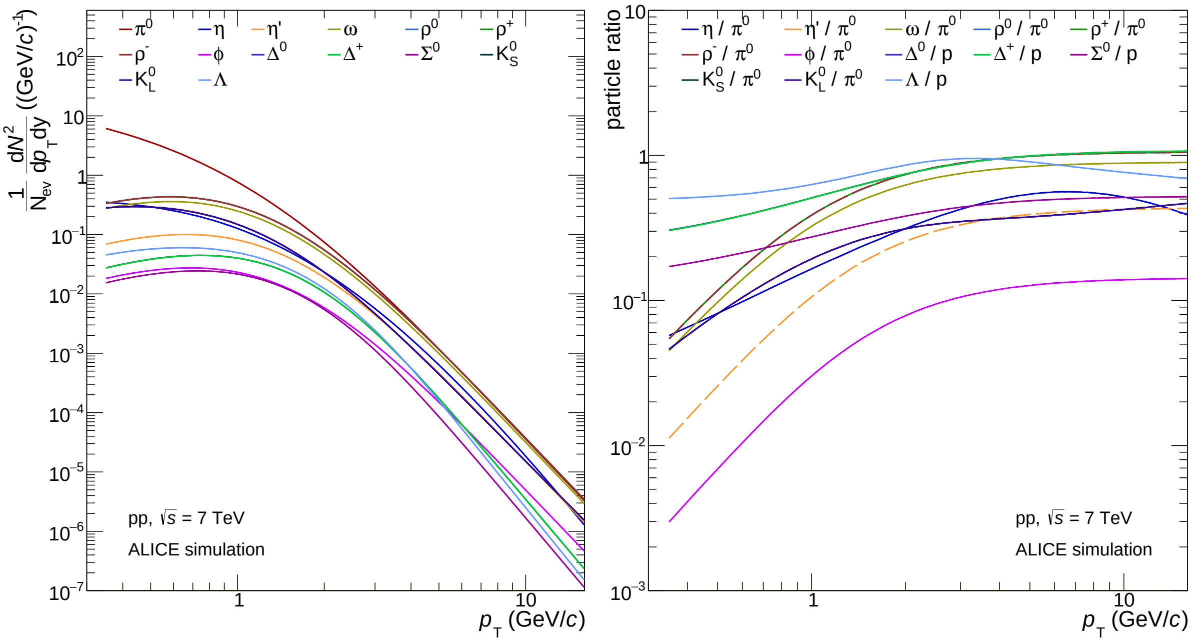

Figure 7.10: Left: Mother particle spectra from the decay simulation at $\sqrt{s} = 7$ TeV. **Right:** Ratio of the mother particle spectra to the neutral pion or proton spectrum.

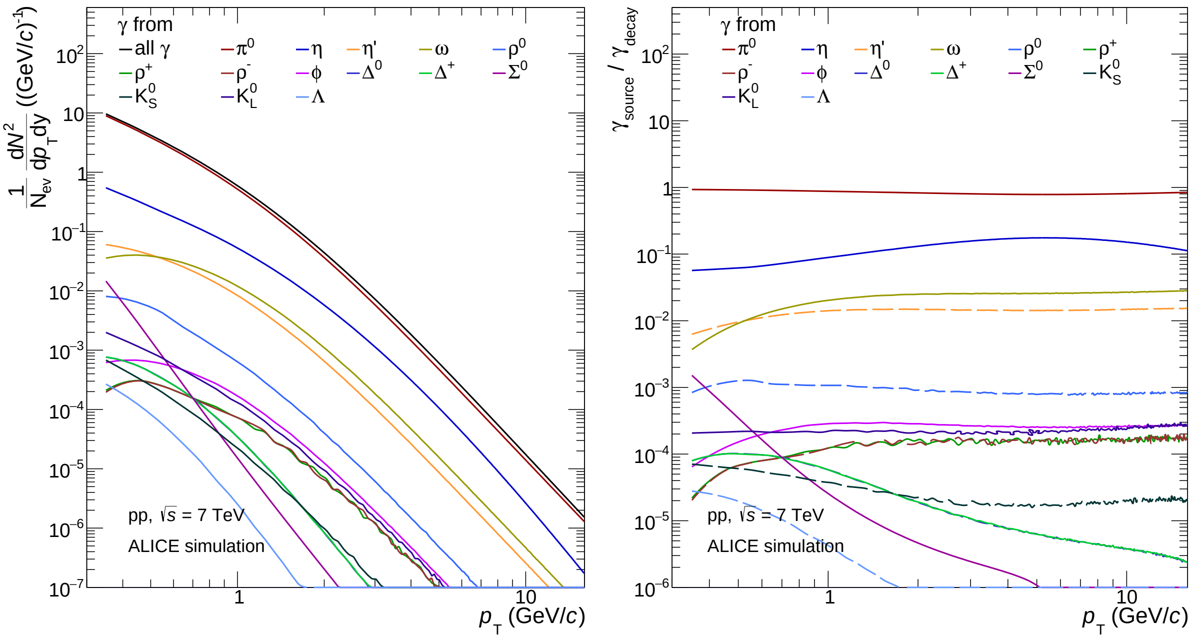

Figure 7.11: Left: Decay photon spectra from the cocktail simulation at $\sqrt{s} = 7$ TeV. **Right:** Fraction of the decay photon sources to the full decay photon cocktail.

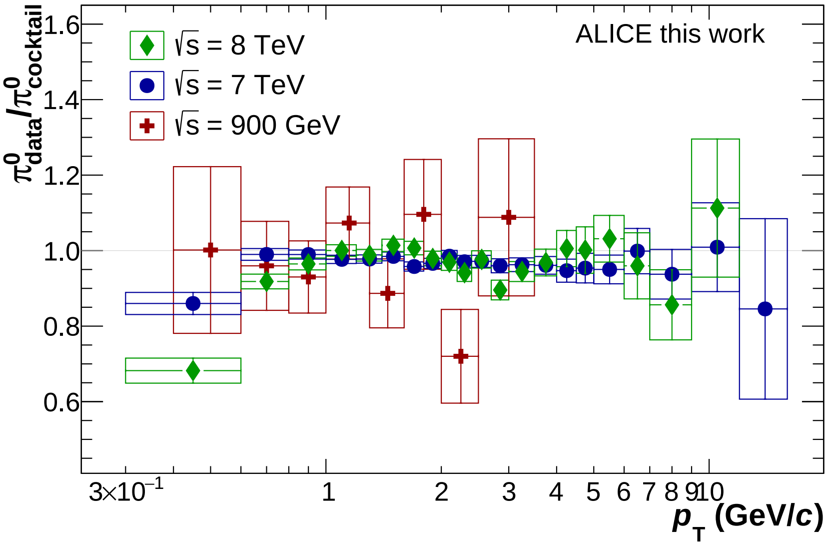

Figure 7.12: Comparison of the measured and the generated neutral pion spectrum for the three center-of-mass energy measurements and cocktail simulations.

is used as input for the cocktail. In Figure 7.12 both neutral pion spectra, measured and generated, are shown together for the three center-of-mass energy measurements and cocktail simulations. Differences at low and high p_{T} come from the lower statistics in these bins for the measured spectrum and therefore a possible difference due to the fitting for the cocktail input parametrization. Differences in the decay photon spectrum as well as the generated neutral pion spectrum due to the input parametrizations are accounted for in the systematic uncertainties of the direct photon excess ratio in the next section.

7.2.2 Direct Photon Excess Ratio and Spectrum

The direct photon excess ratio provides the information, whether an excess of direct photons is observed in the inclusive sample. The ratio compares the ratio of the measured photon signal to the measured neutral pion spectrum to the same ratio obtained from the cocktail simulation. An excess ratio above unity would therefore indicate the contribution of photons that do not originate from particle decays. These photons can originate either from soft or hard processes as explained in Section 2.4.
The excess ratio, which is a double ratio, is used as it provides partial cancellation of systematic uncertainties especially for the constant material budget uncertainty of 4.5%. The double ratio is given as:

$$R_\gamma = \frac{(\gamma_{\mathrm{inc}}(p_{\mathrm{T}})/\pi^0(p_{\mathrm{T}}))_{\mathrm{meas}}}{(\gamma_{\mathrm{dec}}(p_{\mathrm{T}})/\pi^0(p_{\mathrm{T}}))_{\mathrm{sim}}} \approx \frac{\gamma_{\mathrm{inc}}(p_{\mathrm{T}})}{\gamma_{\mathrm{dec}}(p_{\mathrm{T}})}. \tag{35}$$

Here, $\gamma_{\mathrm{inc}}(p_{\mathrm{T}})$ represents the inclusive photon transverse momentum distribution which includes both, direct and decay photons. The decay photon spectrum from the cocktail simulation is given by $\gamma_{\mathrm{dec}}(p_{\mathrm{T}})$ and $\pi^0(p_{\mathrm{T}})$ represents the neutral pion spectra. By definition, $R_\gamma > 1$ implies a direct photon excess signal. Figure 7.13 shows the excess ratio calculated from the inclusive γ/π^0 and the cocktail-based γ/π^0 ratio for all three center-of-mass energy measurements including systematic uncertainties. Within the uncertainties no significant excess above unity is observed. In addition, the data is consistent

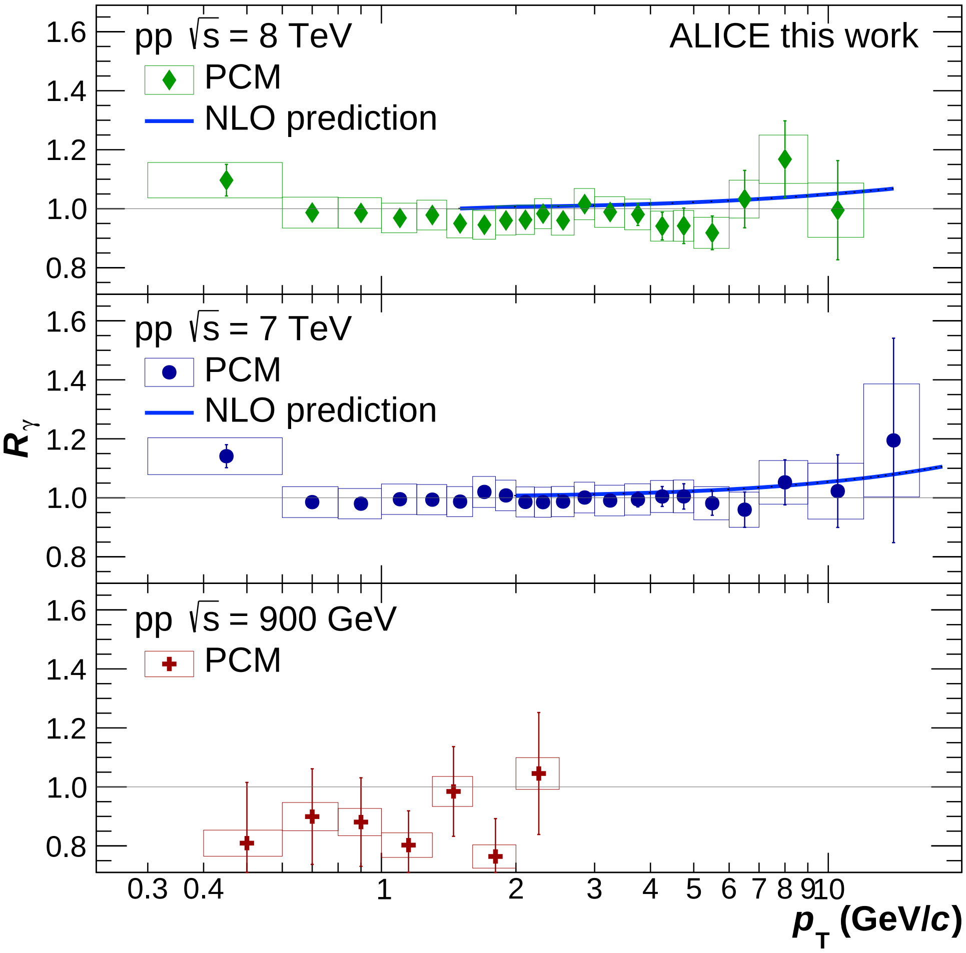

Figure 7.13: Direct photon excess ratio for the three center-of-mass energy measurements including systematic uncertainties and pQCD NLO predictions.

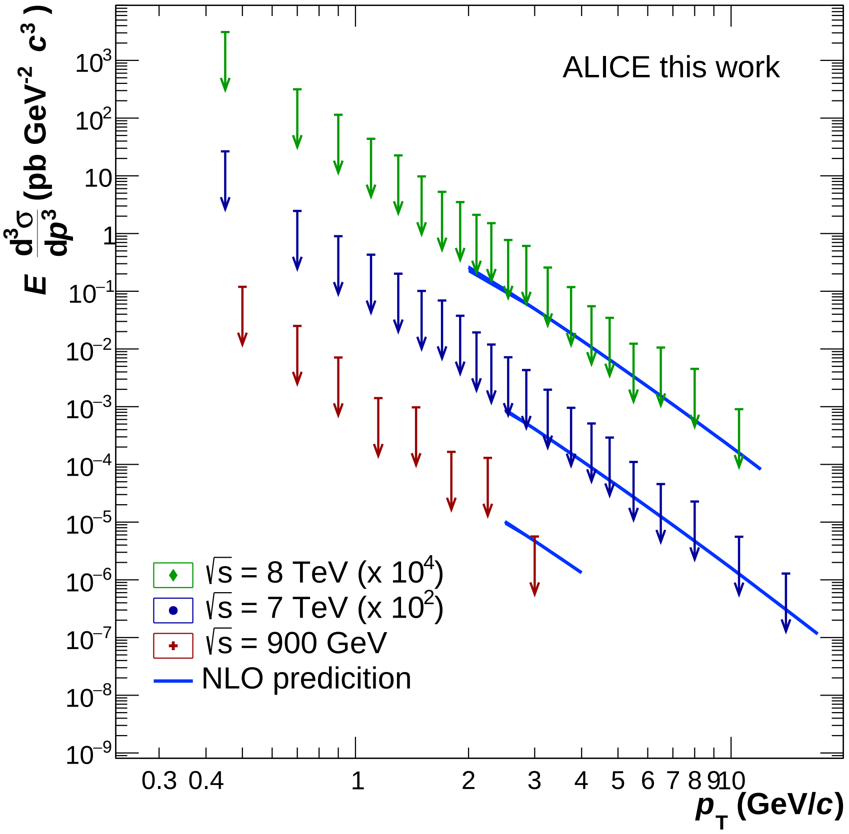

Figure 7.14: Calculated direct photon upper limits for all three center-of-mass energy measurements including the pQCD NLO predictions.

with the NLO calculations, despite the rise at high p_T not being visible due to the large uncertainties.
The calculation of the direct photon spectrum is then done using the measured R_γ and the measured inclusive spectrum with the following formula:

$$\gamma_\mathrm{dir}(p_\mathrm{T}) = \gamma_\mathrm{inc}(p_\mathrm{T}) - \gamma_\mathrm{dec}(p_\mathrm{T}) = \gamma_\mathrm{inc}(p_\mathrm{T}) \cdot \left(1 - R_\gamma^{-1}(p_\mathrm{T})\right) \tag{36}$$

Due to the large uncertainties that can be seen in Figure 7.13 on R_γ it is not possible to give distinct points for the direct photon spectrum. Instead upper limits are calculated which represent a 95% confidence level based on the combined statistical and systematic uncertainties for the direct photon spectrum. This calculation employs a Gaussian distribution around the central values of R_γ with the width being the quadratic sum of statistical and systematical uncertainty. The upper limits are then the R_γ value at which the section of the Gaussian with $R_\gamma > 1$ is given with a 95 percentile fraction. This can also be expressed as:

$$\int_1^K G(x|\mu, \sigma)\mathrm{d}x = 95\% \tag{37}$$

Here, K stands for the value of the upper limit, μ is the mean of the Gaussian which is given by the central values of R_γ and $\sigma = \sqrt{\sigma^2_\mathrm{stat} + \sigma^2_\mathrm{sys}}$ being the width of the Gaussian. The calculated upper limits are shown in Figure 7.14 for all three center-of-mass energies including the NLO predictions at high transverse momentum.

It can therefore be concluded that the statistical and systematical limitations of the dataset and the analysis itself are too large to observe a significant excess of prompt photons. In addition, a thermal photon signal is not expected to be visible in proton-proton data which is consistent with the measurements shown in this analysis.

8 Summary and Outlook

The measurements of the π^0 and η meson invariant cross section spectra as well as the direct photon spectra in proton-proton collisions at $\sqrt{s} = 0.9$, 7 and 8 TeV have been presented. For this, data taken by ALICE in 2010 was used for the $\sqrt{s} = 900$ GeV and $\sqrt{s} = 7$ TeV measurements and data collected in 2012 for the $\sqrt{s} = 8$ TeV analysis. A thorough quality assurance was performed for both datasets on a run-wise basis. In addition, a cocktail simulation was produced which uses parametrized measured spectra as input and provides the full description of the secondary particles as well as the decay photons for this analysis.

The neutral meson measurement was based on the two photon decay channel where the photons are reconstructed using the electron-positron pairs originating from their conversions due to material interactions. For the reconstruction of the e^+ and e^- tracks, information from the Time Projection Chamber as well as the Inner Tracking System of ALICE was used. The meson signal was obtained by calculating the invariant mass of every possible photon pair. Underlying combinatorial background was removed using the event mixing method and the remaining signal was fitted with a Gaussian distribution together with an exponential and a linear function to describe the peak as well as the bremsstrahlung tail as well as remaining background under the peak. From the background subtracted invariant mass distributions the raw yield was determined via bin counting in an asymmetric window around the peak position to incorporate the bremsstrahlung tail on the left side of the peak. This window ranged from -11σ to 4σ for the neutral pion and -8σ to 3σ for the η meson.
The raw yield was then corrected for out-of-bunch pileup, secondary neutral pions as well as acceptance and efficiency. The correction factors were obtained by using the Monte Carlo simulations as well as the cocktail simulations. On the corrected spectra the systematic uncertainties were evaluated via detailed cut and parameter variations. For both mesons, the systematic uncertainty is dominated by the material budget with a 9% contribution to the total error.
The corrected spectra have then been compared to and combined with different reconstruction methods. A perfect agreement between PCM and the other methods has been found and the combined spectra were compared to theoretical models as well as charged pions. The theoretical models failed to describe the transverse momentum dependence of the individual neutral meson spectra but showed good agreement in the η/π^0 ratio.

The direct photon measurement was also performed using the photon conversion method and therefore the reconstruction via electron-positron pairs from TPC and ITS based tracks. Corrections were applied similar to the neutral mesons and systematic uncertainties were also evaluated on the corrected spectra. The systematic uncertainty on the inclusive photon spectrum was found to be approximately flat 5% over the full transverse momentum range and dominated by the material budget uncertainty of 4.5%. Using the measured inclusive photon and π^0 meson spectrum as well as the cocktail based decay photon and neutral pion spectrum is was possible to calculate the direct photon excess ratio. The ratio showed no significant excess above unity within the given uncertainties but was found to be consistent with NLO calculations. Upper limits for the direct photon spectrum were calculated using the combined statistical and systematical uncertainties on R_γ and showed an agreement with the NLO calculations.

Improvements to the $\sqrt{s} = 8$ TeV measurement could be made by including EMCal-triggered data as a cross-check as well as an extension of the transverse momentum reach. In addition, the cocktail simulation could be improved by optimizing the input parametrizations and by including more measured spectra instead of using m_T scaling. Furthermore, as the material budget uncertainty is the largest error contribution for all measurements a new approach using weights can be tested in order to possibly reduce its contribution [102]. The weights approach uses the well known TPC gas properties to calibrate the remaining detector parts in radial bins. Additionally, the full combination of the neutral meson measurements at $\sqrt{s} = 7$ TeV including the systematic error correlations is planned and will provide the full description of the spectra at this center-of-mass energy.

A Appendix

The appendix provides supplementary figures to the analysis. It will contain a complete list of runs used in the analysis, detailed transverse momentum invariant mass bins for each data set and Monte Carlo simulation as well as DCAz bins for the out-of-bunch pileup correction. Detailed systematics for the neutral meson and direct photon analysis as well as an overview of the acronyms used in the analysis.

B Run Numbers for the Analysis

LHC10c_900GeV, LHC14j4c_900GeV
118506, 118507, 118512, 118518, 118556, 118558, 118560, 118561, 121039, 121040
LHC10b, LHC14j4b
114786, 114798, 114918, 114920, 114924, 114931, 115186, 115193, 115310, 115318, 115322, 115328, 115335, 115345, 115393, 115399, 115401, 116079, 116081, 116102, 116288, 116402, 116403, 116562, 116571, 116574, 116643, 116645, 117048, 117050, 117052, 117053, 117059, 117060, 117063, 117092, 117099, 117109, 117112, 117116, 117220, 117222
LHC10c, LHC14j4c
119159, 119161, 119163, 119841, 119842, 119844, 119845, 119846, 119849, 119853, 119856, 119859, 119862, 120067, 120069, 120072, 120073, 120076, 120079, 120244, 120503, 120504, 120505, 120616, 120617, 120671, 120741, 120750, 120758, 120820, 120821, 120822, 120823, 120824, 120825, 120829
LHC10d, LHC14j4d
122374, 122375, 124751, 125083, 125085, 125097, 125100, 125133, 125134, 125139, 125140, 125156, 125186, 125295, 125296, 125630, 125632, 125842, 125843, 125847, 125848, 125849, 125850, 125851, 125855, 126004, 126007, 126008, 126073, 126078, 126081, 126082, 126088, 126090, 126097, 126158, 126160, 126167, 126168, 126283, 126284, 126285, 126351, 126352, 126359, 126403, 126404, 126405, 126406, 126407, 126408, 126409, 126422, 126424, 126425, 126432
LHC10e, LHC14j4e
128366, 128452, 128494, 128495, 128498, 128503, 128504, 128505, 128506, 128582, 128590, 128592, 128594, 128596, 128605, 128609, 128611, 128615, 128621, 128677, 128678, 128777, 128778, 128819, 128820, 128823, 128824, 128833, 128834, 128835, 128836, 128843, 128850, 128853, 128855, 128913, 129042, 129512, 129513, 129514, 129515, 129516, 129519, 129520, 129521, 129523, 129524, 129525, 129527, 129528, 129536, 129540, 129586, 129587, 129599, 129639, 129641, 129647, 129650, 129651, 129652, 129653, 129659, 129666, 129723, 129726, 129729, 129734, 129735, 129736, 129738, 129742, 129744, 129959, 129960, 129961, 129962, 129966, 130149, 130151, 130157, 130158, 130168, 130172, 130178, 130342, 130343, 130354, 130356, 130358, 130360, 130375, 130480, 130481, 130517, 130519, 130520, 130524, 130526, 130601, 130608, 130609, 130620, 130621, 130623, 130628, 130696, 130704, 130793, 130795, 130798, 130799, 130834, 130840, 130842, 130844, 130847, 130848, 130850
LHC10f, LHC14j4f
133006, 133007, 133010, 133327, 133329, 133330, 133414, 133563, 133670, 133762, 133800, 133920, 133969, 133982

Table 14: Runs used for the $\sqrt{s} = 900$ GeV and $\sqrt{s} = 7$ TeV neutral meson and direct photon analysis.

LHC12a, LHC15h1a1, LHC15h2a
176701, 176704, 176730, 176749, 176752, 176753, 176854, 176859, 176924, 176926, 176927, 176929, 177157, 177160, 177167, 177173, 177180, 177182
LHC12b, LHC15h1b, LHC15h2b
177580, 177592, 177597, 177612, 177620, 177624, 177671, 177798, 177799, 177804, 177858, 177861, 177864, 177869, 177942
LHC12c, LHC15h1c, LHC15h2c
179618, 179621, 179639, 179802, 179803, 179858, 179859, 179917, 179918, 179920, 180000, 180042, 180044, 180127, 180129, 180130, 180131, 180133, 180199, 180200, 180500, 180501, 180515, 180561, 180564, 180567, 180569, 180719, 180720, 182017, 182018, 182022, 182106, 182110, 182111, 182207, 182289, 182295, 182297, 182299, 182300, 182302, 182322, 182323, 182325, 182624, 182684, 182687, 182692, 182728, 182729, 182730, 182740, 182741, 182744
LHC12d, LHC15h1d, LHC15h2d
184132, 184135, 184137, 184138, 184208, 184215, 184687, 184784, 184786, 185029, 185031, 185116, 185126, 185132, 185134, 185157, 185160, 185164, 185189, 185196, 185203, 185206, 185208, 185217, 185221, 185282, 185284, 185288, 185289, 185291, 185292, 185296, 185300, 185302, 185349, 185350, 185351, 185356, 185360, 185361, 185362, 185363, 185371, 185375, 185461, 185474, 185575, 185578, 185580, 185581, 185582, 185583, 185687, 185738, 185768, 185776, 185778, 185784, 186163, 186164, 186167, 186205
LHC12f, LHC15h1f, LHC15h2f
188101, 188093, 187849, 187796, 187791, 187785, 187753, 187749, 187739, 187698, 187697, 187695, 187656, 187633, 187627, 187624, 187623, 187561, 187560, 187537, 187536, 187510, 187508, 187489, 187488, 187487, 187486, 187485, 187484, 187343, 187341, 187340, 187339, 187203, 187202, 187201, 187149, 187143, 187136, 187084, 187047, 186992, 186990, 186989, 186987, 186969, 186967, 186966, 186965, 186938, 186937, 186857, 186853, 186851, 186845, 186844, 186838, 186815, 186809, 186807, 186692, 186690, 186668
LHC12h, LHC15h1h, LHC15h2h
189122, 189146, 189183, 189228, 189229, 189231, 189306, 189310, 189315, 189316, 189350, 189351, 189352, 189353, 189396, 189397, 189400, 189402, 189406, 189407, 189409, 189410, 189411, 189473, 189474, 189522, 189523, 189526, 189577, 189603, 189605, 189606, 189610, 189612, 189615, 189616, 189621, 189659, 189696, 189697, 189698, 189734, 189735, 189736, 189737, 190150, 190209, 190210, 190212, 190214, 190215, 190216, 190303, 190305, 190307, 190337, 190338, 190340, 190341, 190342, 190386, 190388, 190389, 190390, 190392, 190393, 190416, 190417, 190418, 190421, 190425, 190867, 190895, 190898, 190903, 190904, 190968, 190970, 190974, 190975, 190979, 190981, 190983, 190984, 191031, 191129, 191227, 191229, 191230, 191231, 191234, 191244, 191245, 191247, 191248, 191445, 191450, 191451, 192000, 192004, 192072, 192073, 192075, 192095, 192121, 192128, 192136, 192140, 192141, 192172, 192174, 192177, 192194, 192197, 192199, 192200, 192201, 192202, 192205, 192246, 192347, 192348, 192349, 192415, 192417, 192453, 192461, 192468, 192471, 192492, 192499, 192505, 192510, 192535, 192537, 192542, 192548, 192551, 192585, 192602, 192610, 192633, 192645, 192646, 192648, 192658, 192675, 192676, 192688, 192707, 192708, 192709, 192711, 192729, 192731, 192732
LHC12i, LHC15h1i, LHC15h2i
193701, 193698, 193693, 193194, 193193, 193192, 193189, 193188, 193187, 193156, 193155, 193153, 193151, 193148, 193097, 193094, 193093, 193092, 193051, 193049, 193047, 193014, 193011, 193010, 193008, 193007, 193005, 193004, 193000, 192824, 192822, 192820, 192779, 192778, 192775, 192772

Table 15: Runs used for the $\sqrt{s} = 8$ TeV neutral meson and direct photon analysis.

C Supplementary Figures

C.1 Electron nσ dE/dx Distributions

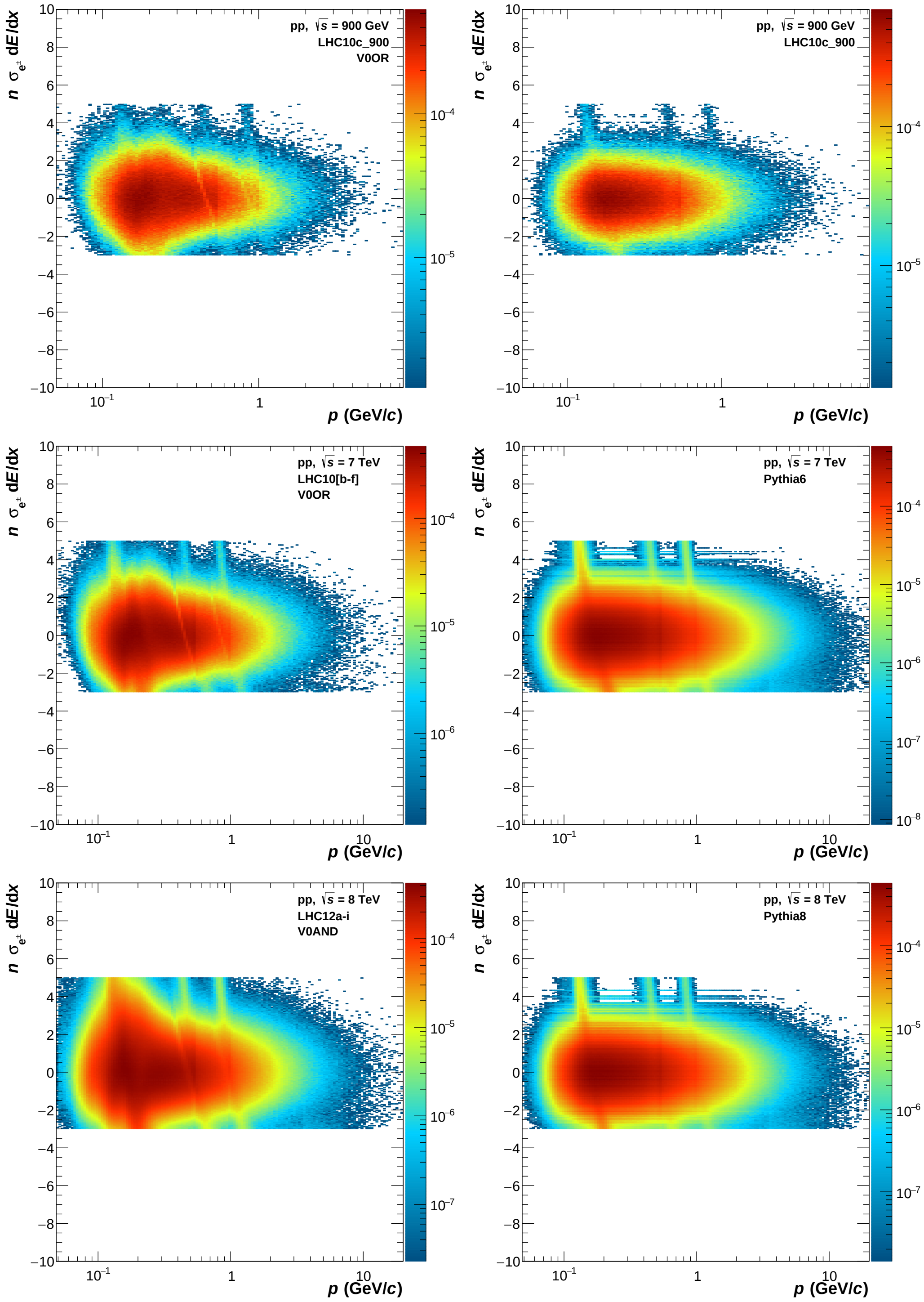

Figure C.1: dE/dx nσ plot for electrons for the three center-of-mass energy measurement data sets and Monte Carlo simulations after all electron selection cuts.

C.2 Signal Extraction in p_T Bins

C.2.1 900 GeV Data and MC Invariant Mass p_T Bins

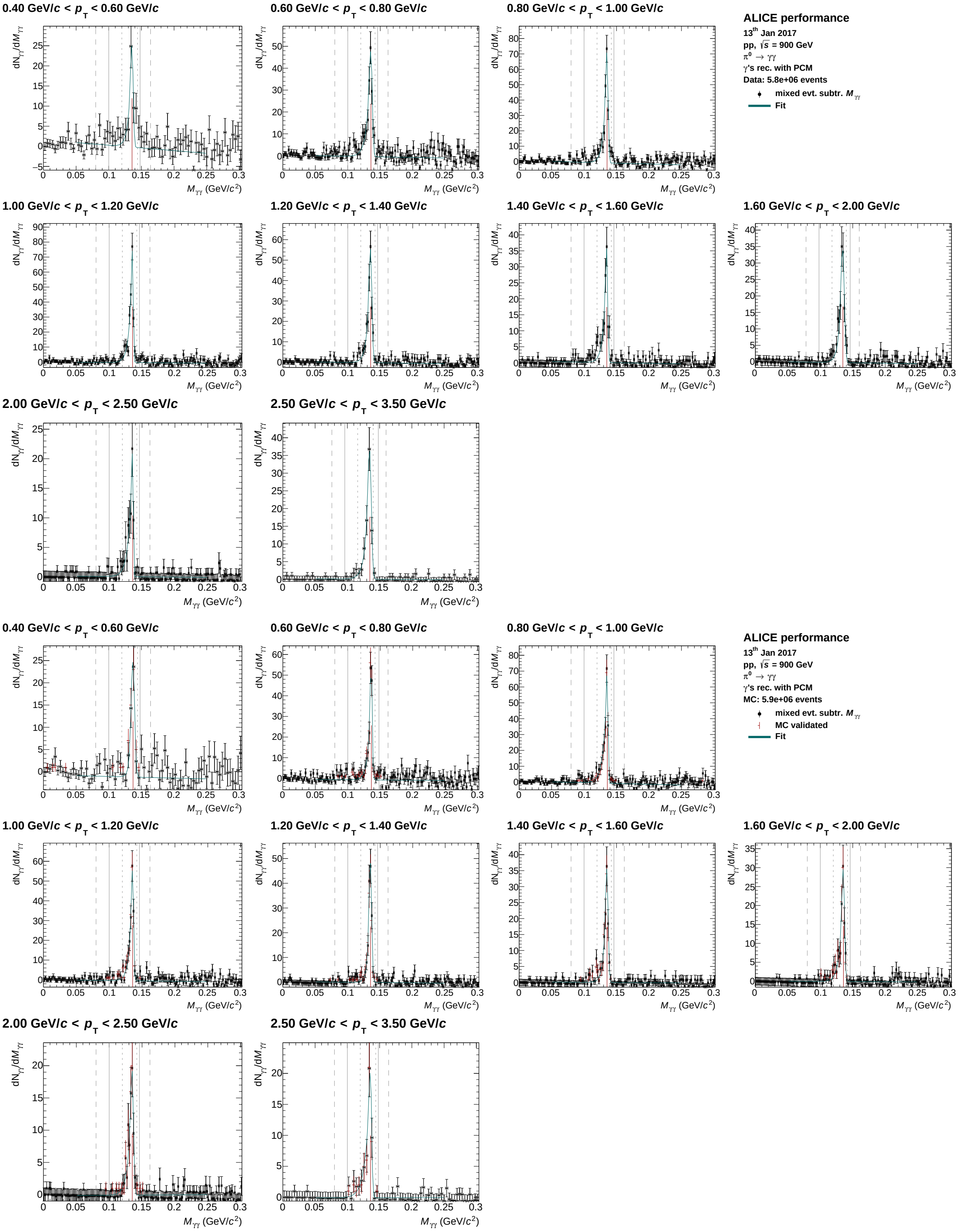

Figure C.2: Top: Invariant mass of the reconstructed photon pairs around the π^0 mass $M_{\gamma\gamma}$ in p_T bins from 0.4 to 3.5 GeV/c for the 900 GeV runs of the period LHC10c. **Bottom:** The invariant mass bins of the LHC14j4c 900 GeV Monte Carlo simulation around the π^0 mass.

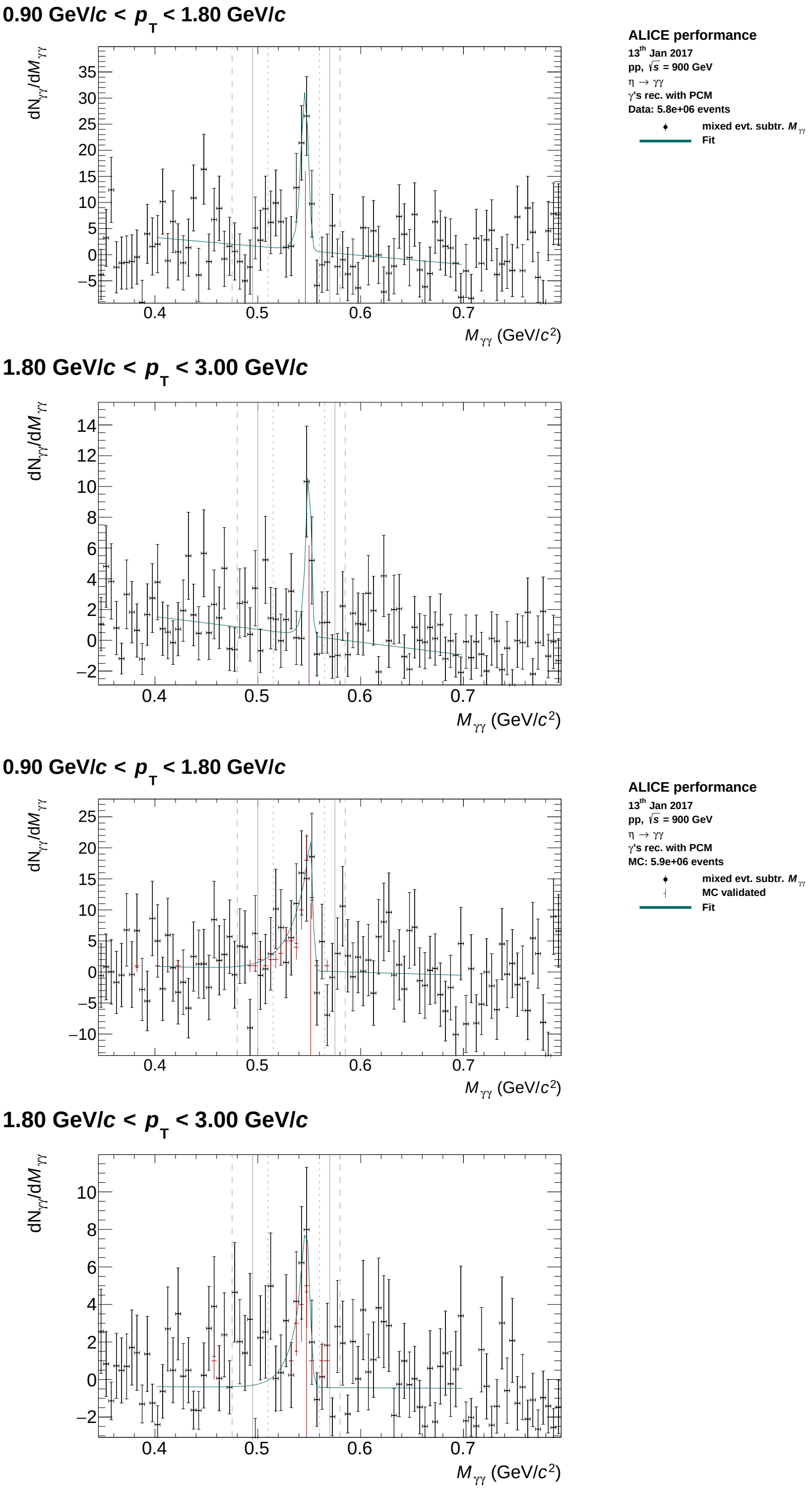

Figure C.3: Top: Invariant mass of the reconstructed photon pairs around the η mass $M_{\gamma\gamma}$ in p_{T} bins from 0.9 to 3. GeV/c for the 900 GeV runs of the period LHC10c. **Bottom:** The invariant mass bins of the LHC14j4c 900 GeV Monte Carlo simulation around the η mass.

C.2.2 7 TeV Data and MC Invariant Mass p_{T} Bins

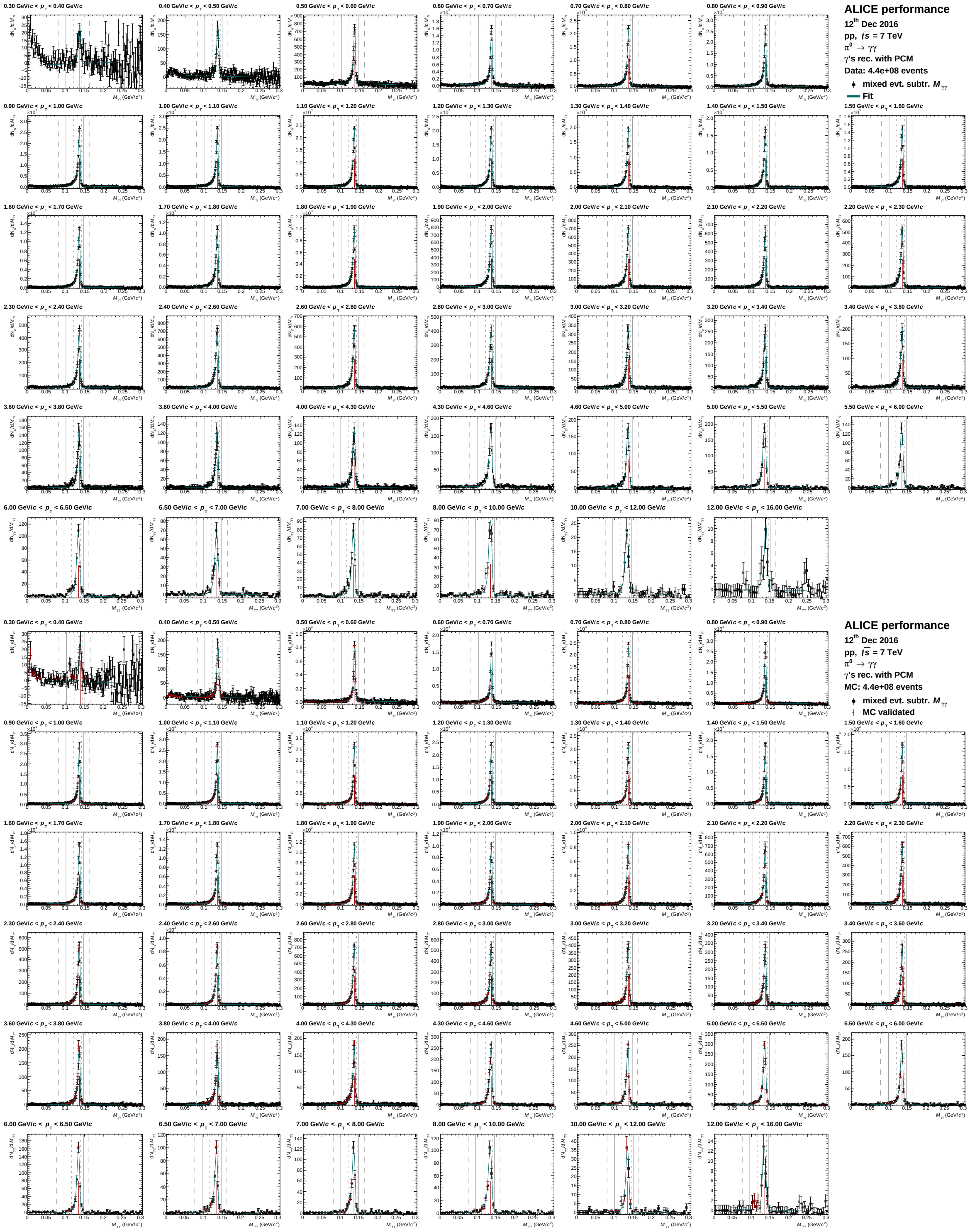

Figure C.4: Top: Invariant mass of the reconstructed photon pairs around the π^0 mass $M_{\gamma\gamma}$ in p_{T} bins from 0.3 to 16 GeV/c for the merged 7 TeV data periods LHC10[b-f]. **Bottom:** The invariant mass bins of the merged Pythia 6 Monte Carlo simulation periods LHC14j4[b-f] around the π^0 mass.

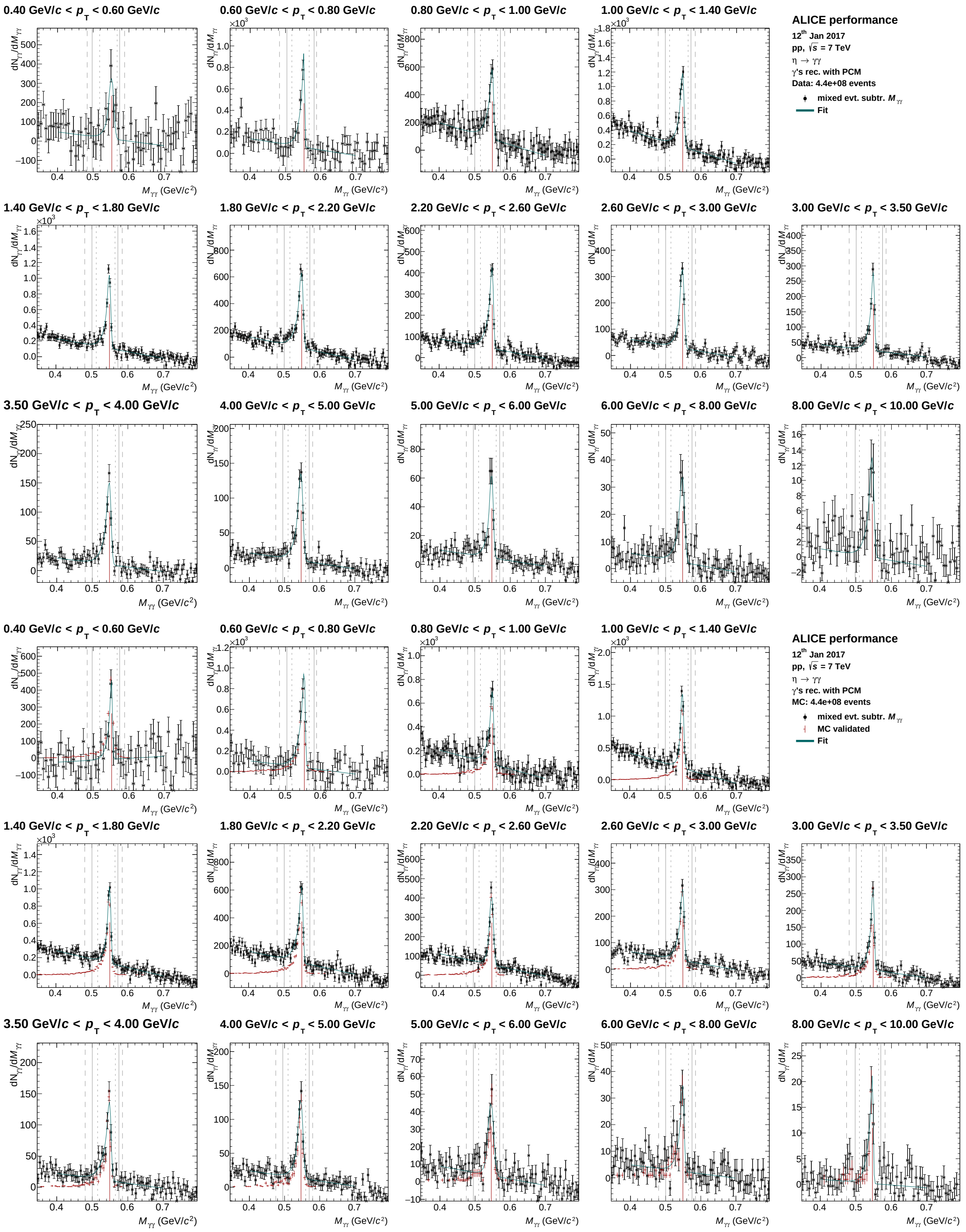

Figure C.5: Top: Invariant mass of the reconstructed photon pairs around the η mass $M_{\gamma\gamma}$ in p_{T} bins from 0.4 to 10 GeV/c for the merged 7 TeV data periods LHC10[b-f]. **Bottom:** The invariant mass bins of the merged Pythia 6 Monte Carlo simulation periods LHC14j4[b-f] around the η mass.

C.2.3 8 TeV Data and MC Invariant Mass p_T Bins

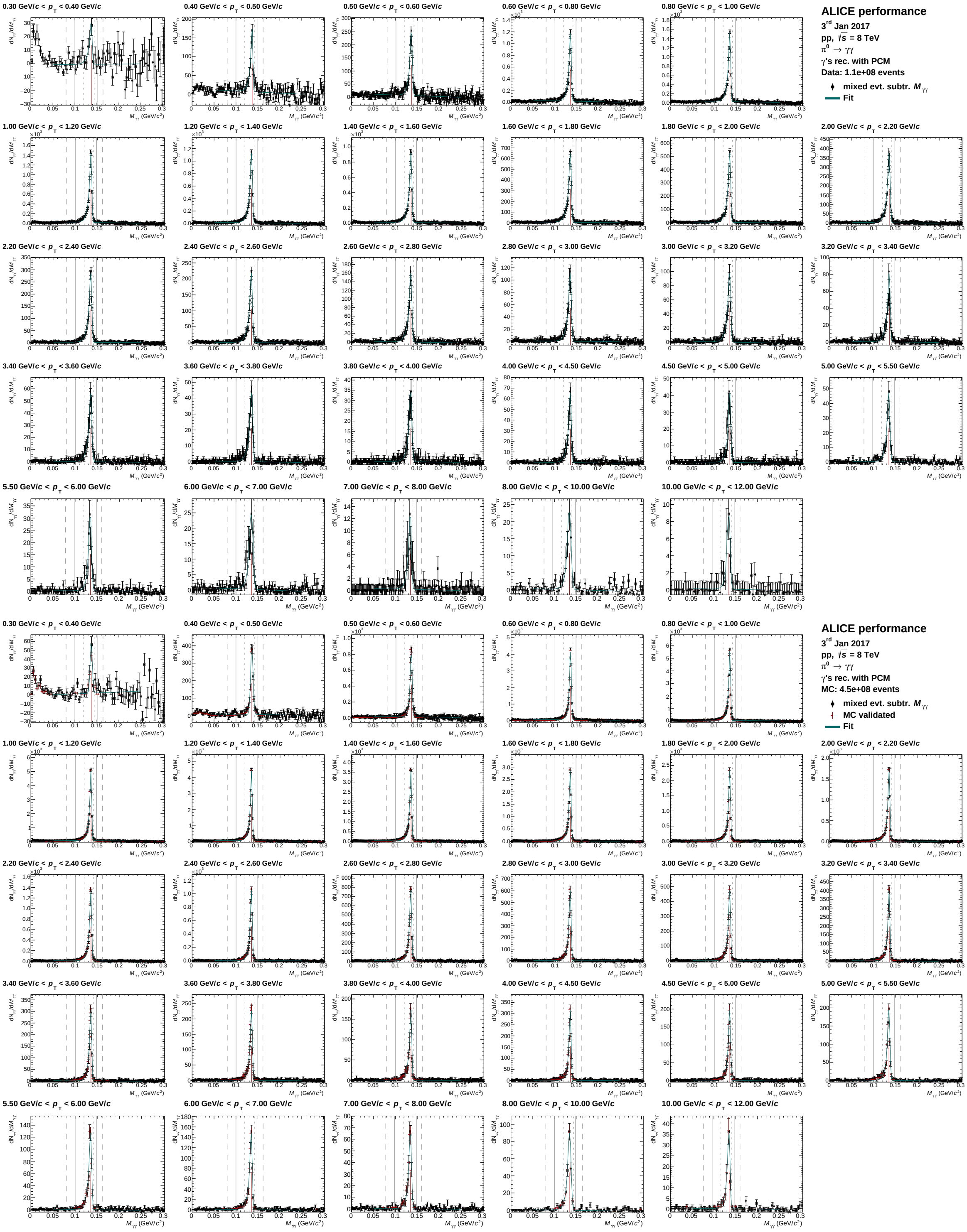

Figure C.6: Top: Invariant mass of the reconstructed photon pairs around the π^0 mass $M_{\gamma\gamma}$ in p_T bins from 0.3 to 12 GeV/c for the merged 7 TeV data periods LHC12[a-i]. **Bottom:** The invariant mass bins of the merged Pythia 6 and Phojet Monte Carlo simulation periods LHC15h1[a1-i] and LHC15h2[a-i] around the π^0 mass.

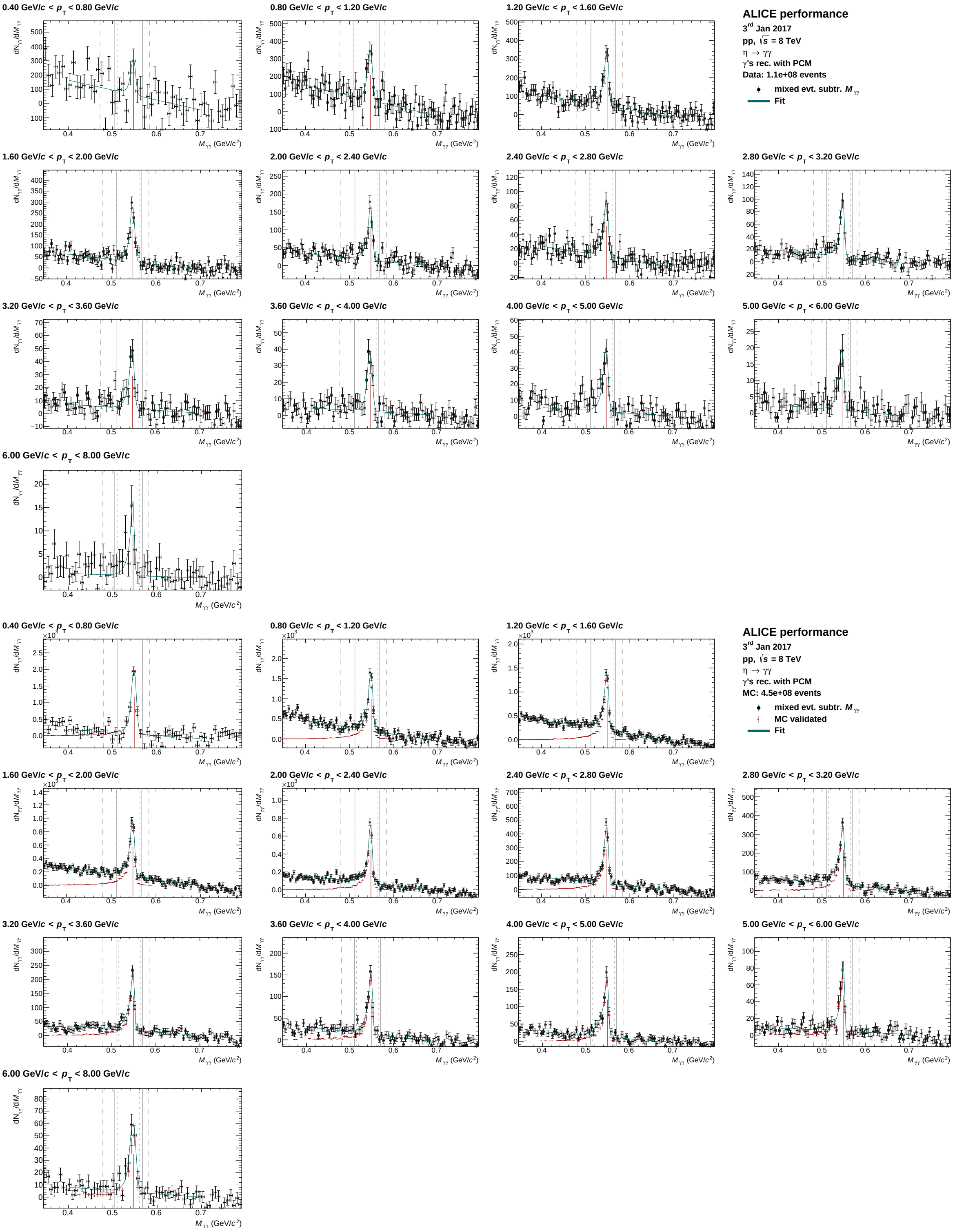

Figure C.7: Top: Invariant mass of the reconstructed photon pairs around the η mass $M_{\gamma\gamma}$ in p_T bins from 0.4 to 8.0 GeV/c for the merged 8 TeV data periods LHC12[a-i]. **Bottom:** The invariant mass bins of the merged Pythia 8 and Phojet Monte Carlo simulation periods LHC15h1[a1-i] and LHC15h2[a-i] around the η mass.

C.3 DCAz Bins

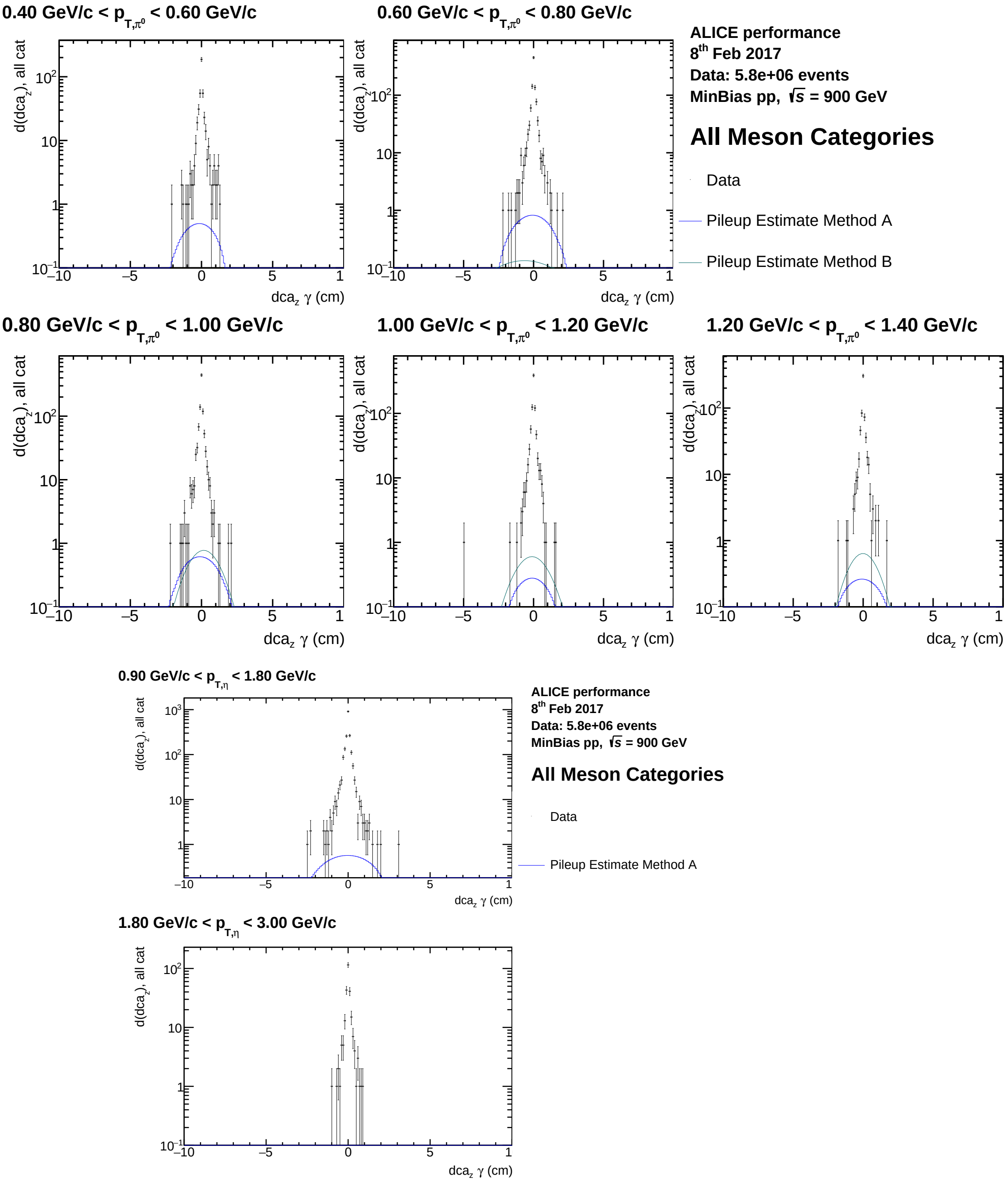

Figure C.8: **Top:** *dca_z* distribution of photons from the $\sqrt{s} = 900$ GeV period LHC10c_900GeV for which the photon pair is in the invariant mass windows of 0.12 GeV/c $< M_{\gamma\gamma} <$ 0.145 GeV/c in different transverse momentum bins. **Bottom:** *dca_z* distribution of photons from LHC10c_900GeV for which the photon pair is in the invariant mass windows of 0.54 GeV/c $< M_{\gamma\gamma} <$ 0.56 GeV/c in different transverse momentum bins. The black points represent the measured data, while the blue line shows the background estimate via the ShowBackground function.

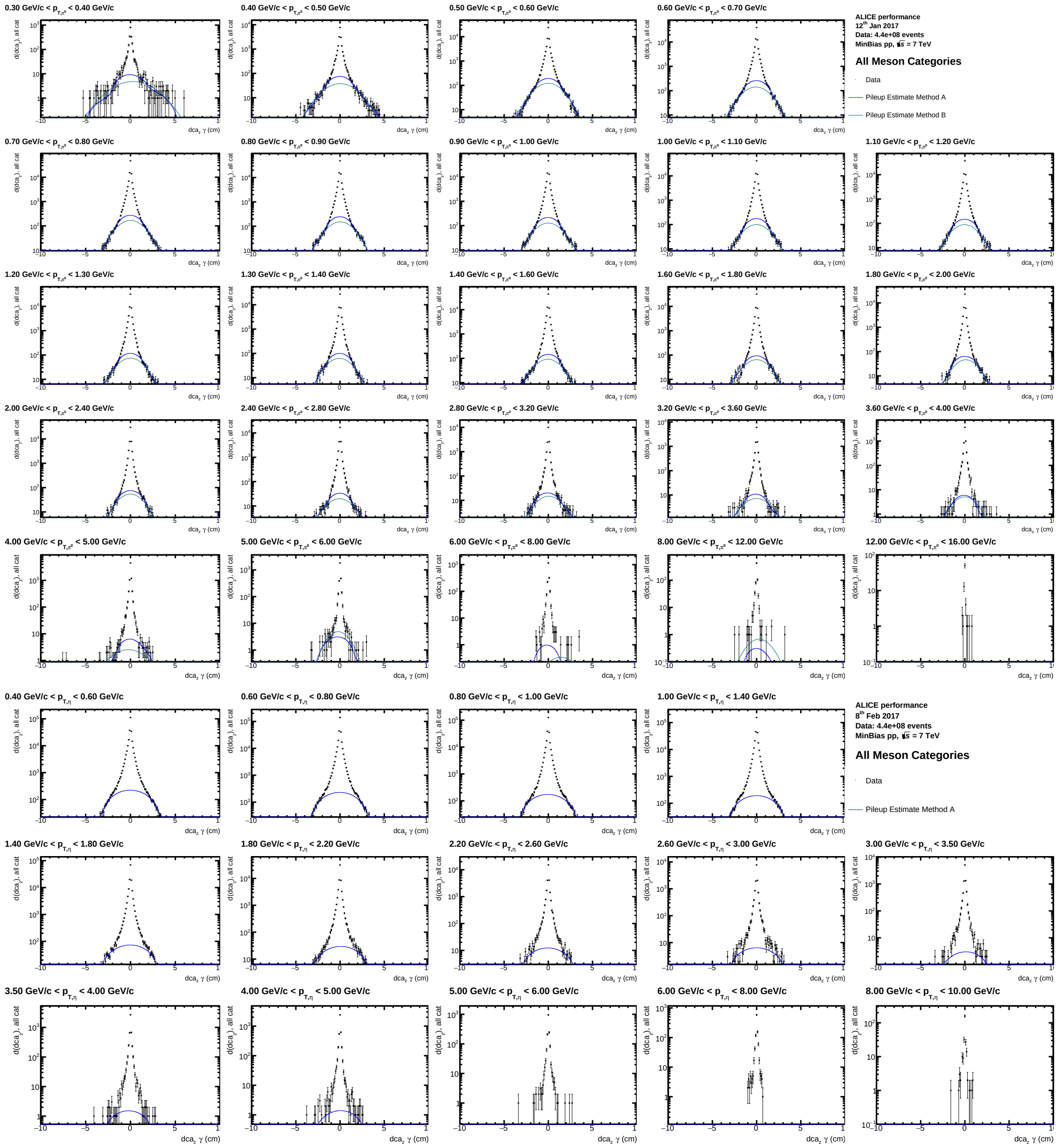

Figure C.9: Top: dca_z distribution of photons from the $\sqrt{s} = 7$ TeV periods LHC10[b-f] for which the photon pair is in the invariant mass windows of 0.12 GeV/c < $M_{\gamma\gamma}$ < 0.145 GeV/c in different transverse momentum bins. **Bottom:** dca_z distribution of photons from LHC10[b-f] for which the photon pair is in the invariant mass windows of 0.54 GeV/c < $M_{\gamma\gamma}$ < 0.56 GeV/c in different transverse momentum bins. The black points represent the measured data, while the blue line shows the background estimate via the ShowBackground function.

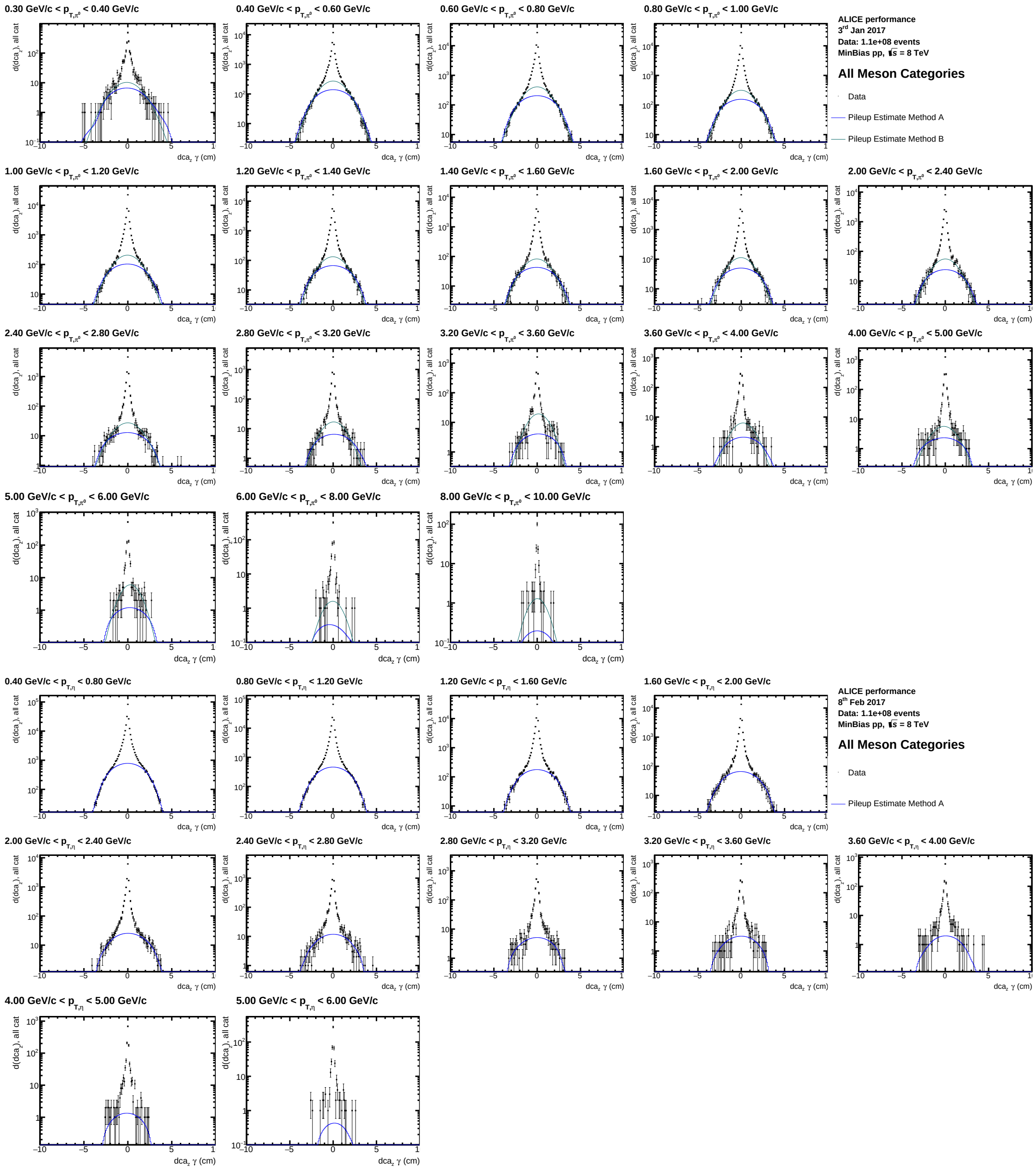

Figure C.10: Top: dca_z distribution of photons from the $\sqrt{s} = 8$ TeV periods LHC12[a-i] for which the photon pair is in the invariant mass windows of 0.12 GeV/c $< M_{\gamma\gamma} <$ 0.145 GeV/c in different transverse momentum bins. **Bottom:** dca_z distribution of photons from LHC12[a-i] for which the photon pair is in the invariant mass windows of 0.54 GeV/c $< M_{\gamma\gamma} <$ 0.56 GeV/c in different transverse momentum bins. The black points represent the measured data, while the blue line shows the background estimate via the ShowBackground function.

C.4 Secondary Photon Efficiencies and Conversion Probabilities

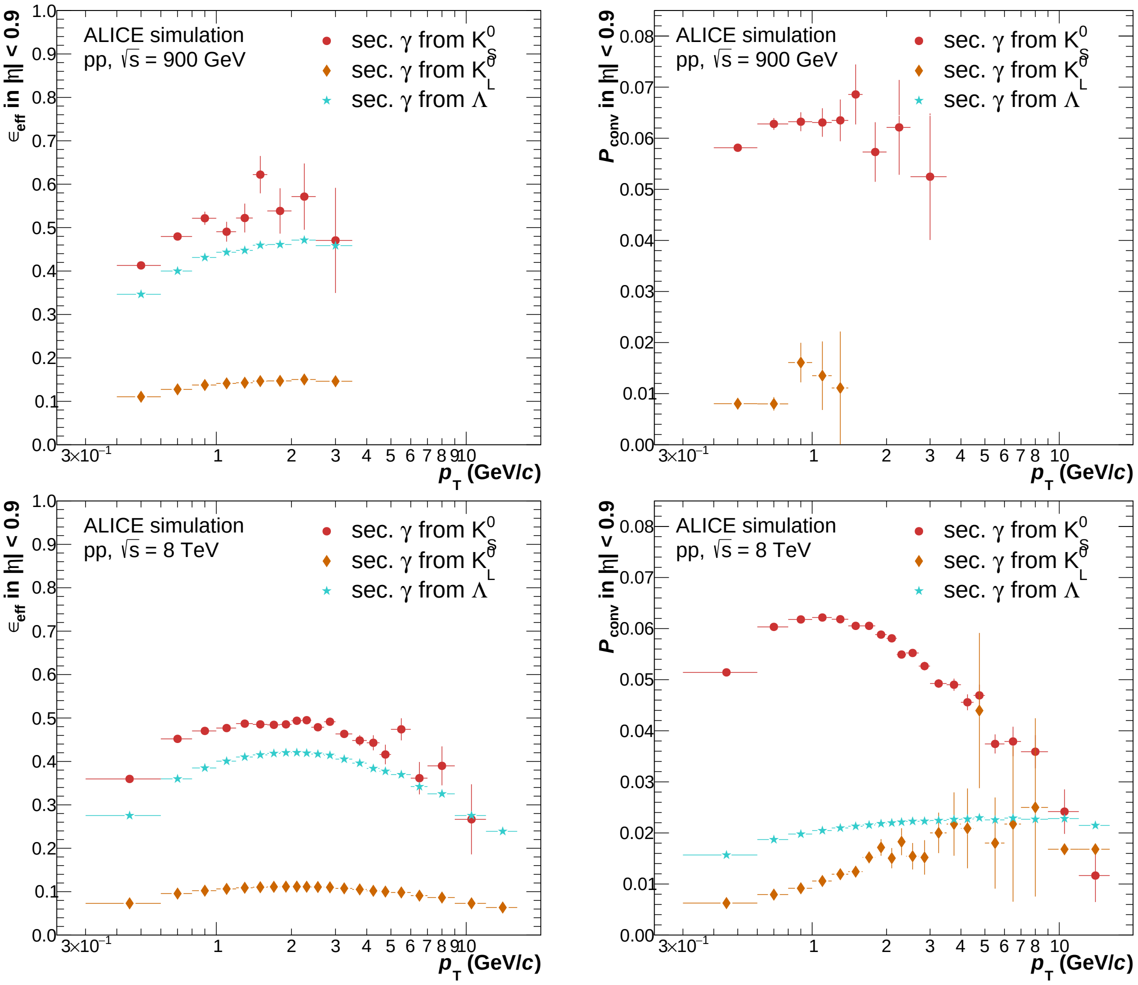

Figure C.11: Left: Reconstruction efficiency for secondary photons coming from K^0_S, K^0_L and Λ decays. **Right:** Conversion probabilities of the secondary photons originating from K^0_S, K^0_L and Λ decays. **Top** plots show the points obtained from the $\sqrt{s} = 900$ GeV Monte Carlo and decay simulation and **bottom** plots show the $\sqrt{s} = 8$ TeV points.

C.5 Secondary Photon Raw Yield

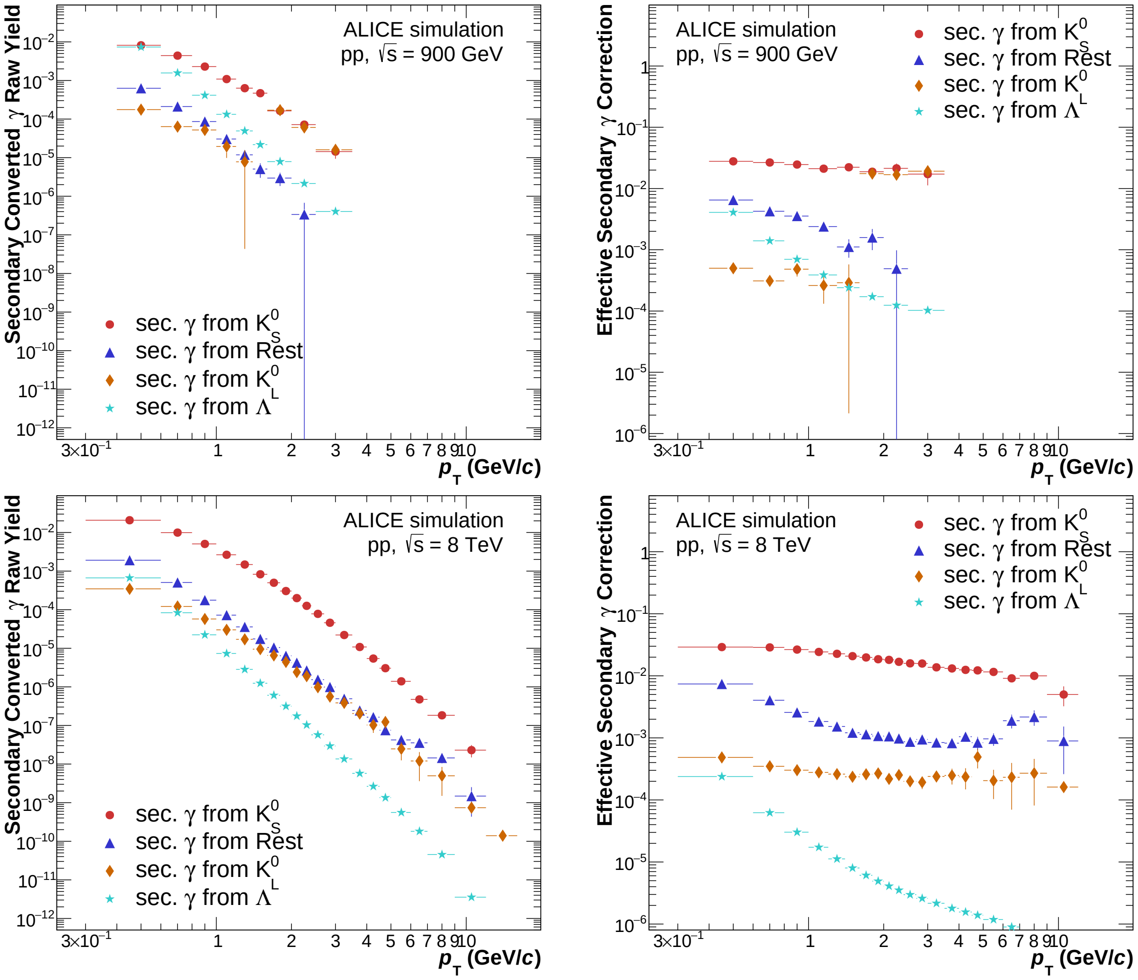

Figure C.12: Left: Raw yields for secondary photons coming from K^0_S, K^0_L and Λ decays. **Right:** Fractions of secondary photons from K^0_S, K^0_L and Λ decays to the measured raw photon spectrum. **Top** plots show the points obtained from the $\sqrt{s} = 900$ GeV Monte Carlo and decay simulation and **bottom** plots show the $\sqrt{s} = 8$ TeV points.

C.6 Detailed Systematic Uncertainties

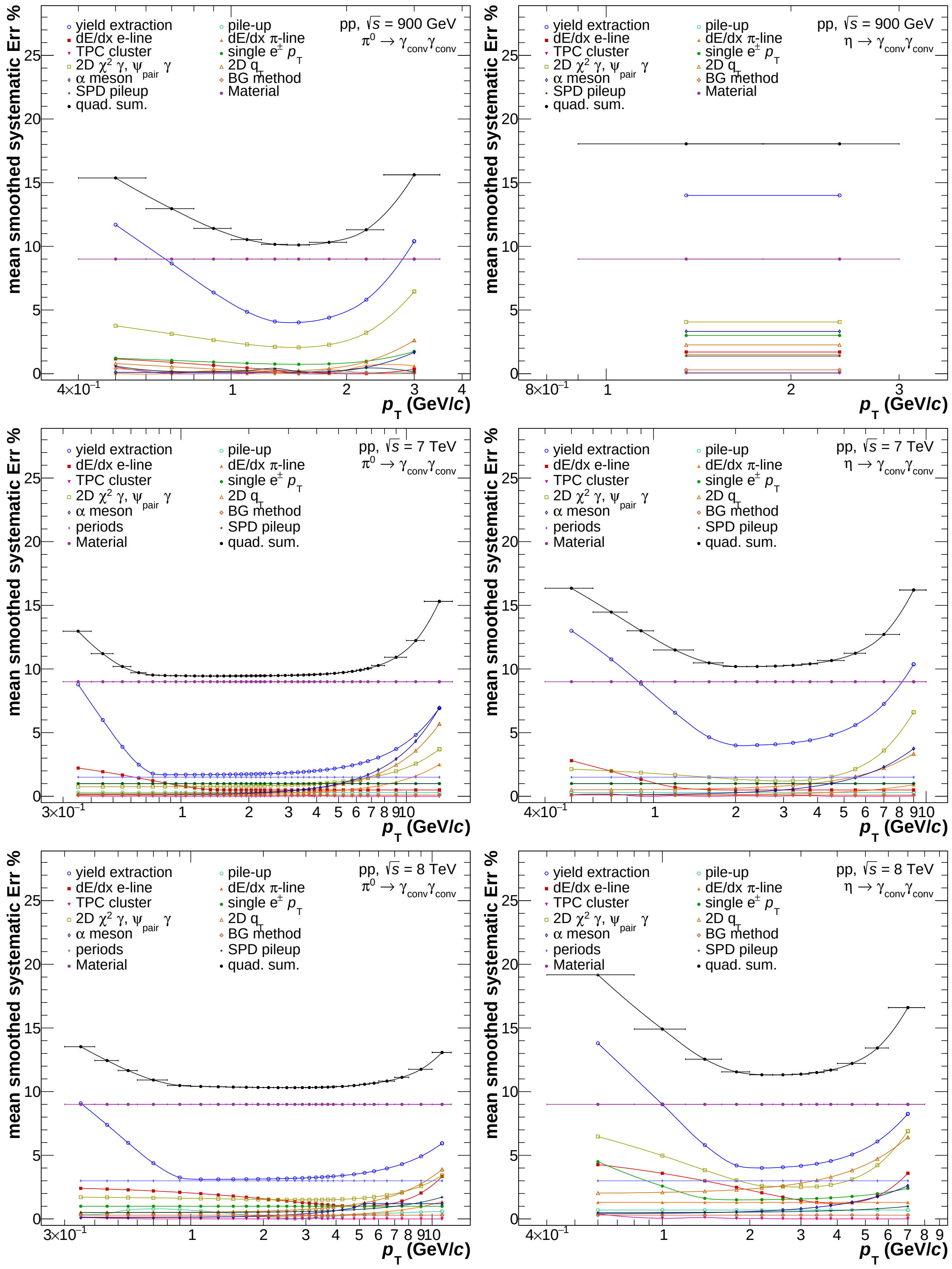

Figure C.13: Visualization of the detailed systematic uncertainties for the neutral meson measurements at the three presented center-of-mass energies. Indicated with colored points are the individual error sources whereas the final systematic uncertainty is represented with the black points.

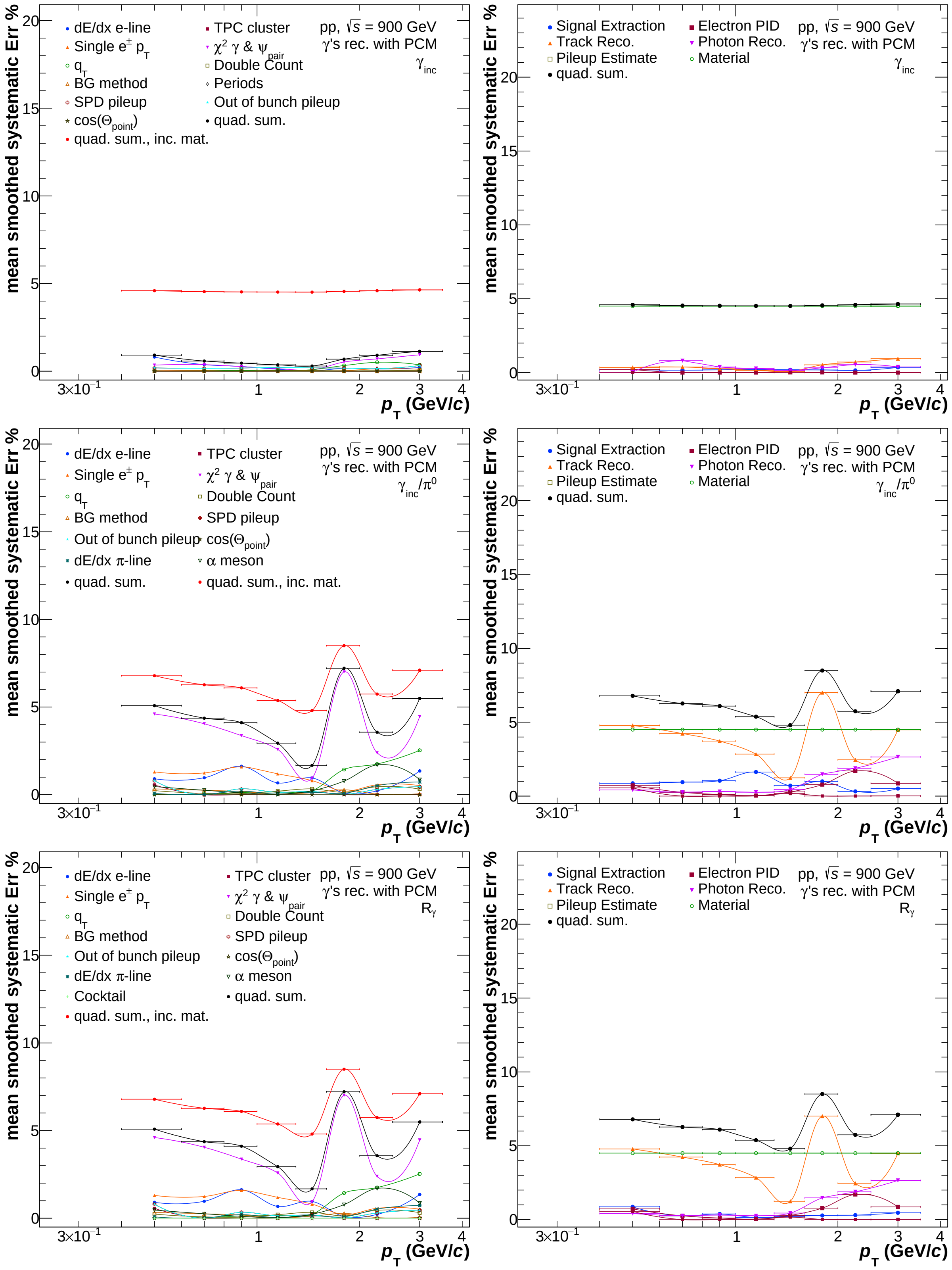

Figure C.14: Left: Detailed systematic uncertainty contributions from all sources. **Right:** Combined systematic uncertainties in different categories. Points shown for the $\sqrt{s}$ = 900 GeV inclusive photons, the γ/π^0 ratio and the double ratio R_γ from top to bottom.

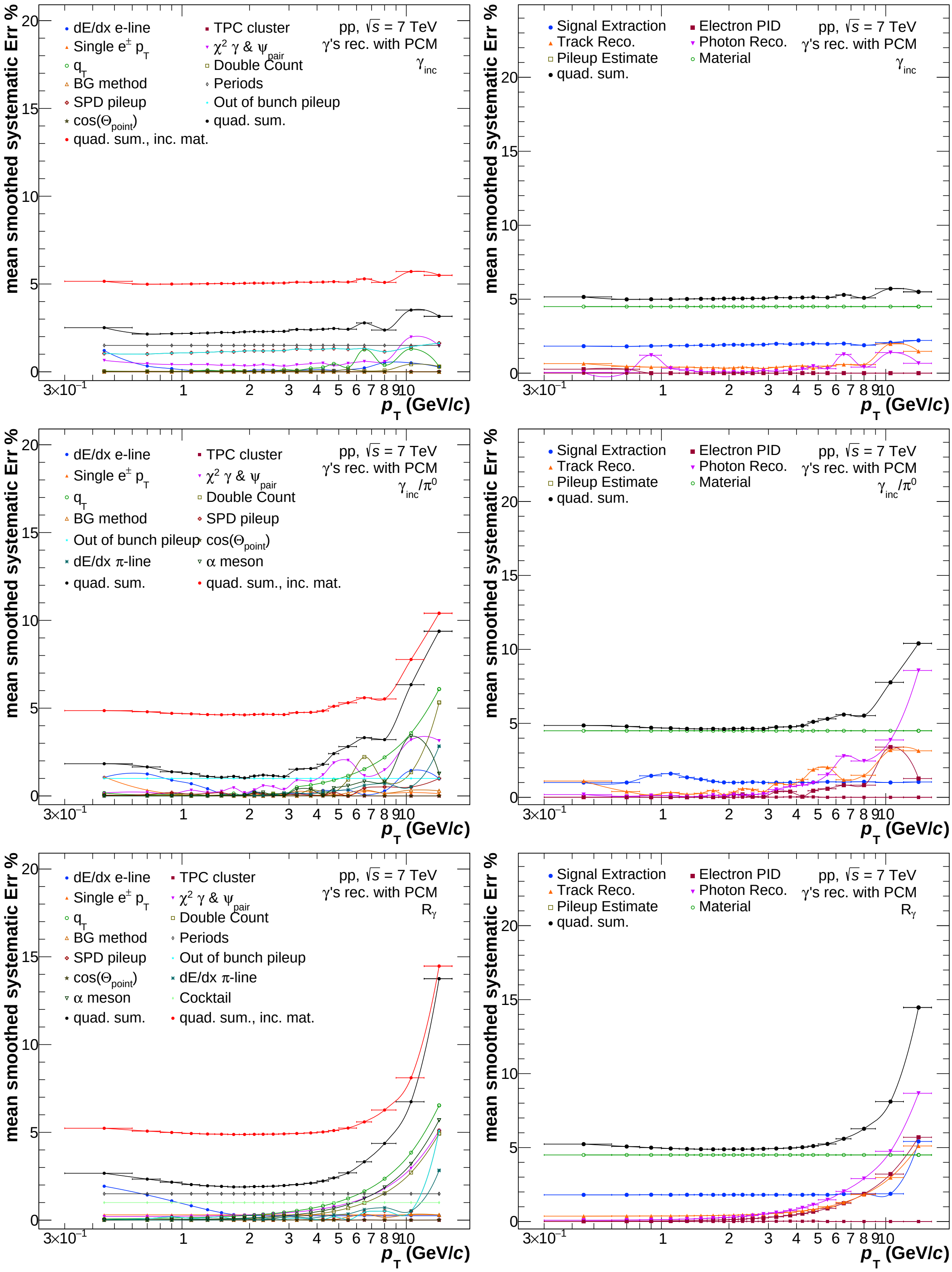

Figure C.15: Left: Detailed systematic uncertainty contributions from all sources. **Right:** Combined systematic uncertainties in different categories. Points shown for the $\sqrt{s} = 7$ TeV inclusive photons, the γ/π^0 ratio and the double ratio R_γ from top to bottom.

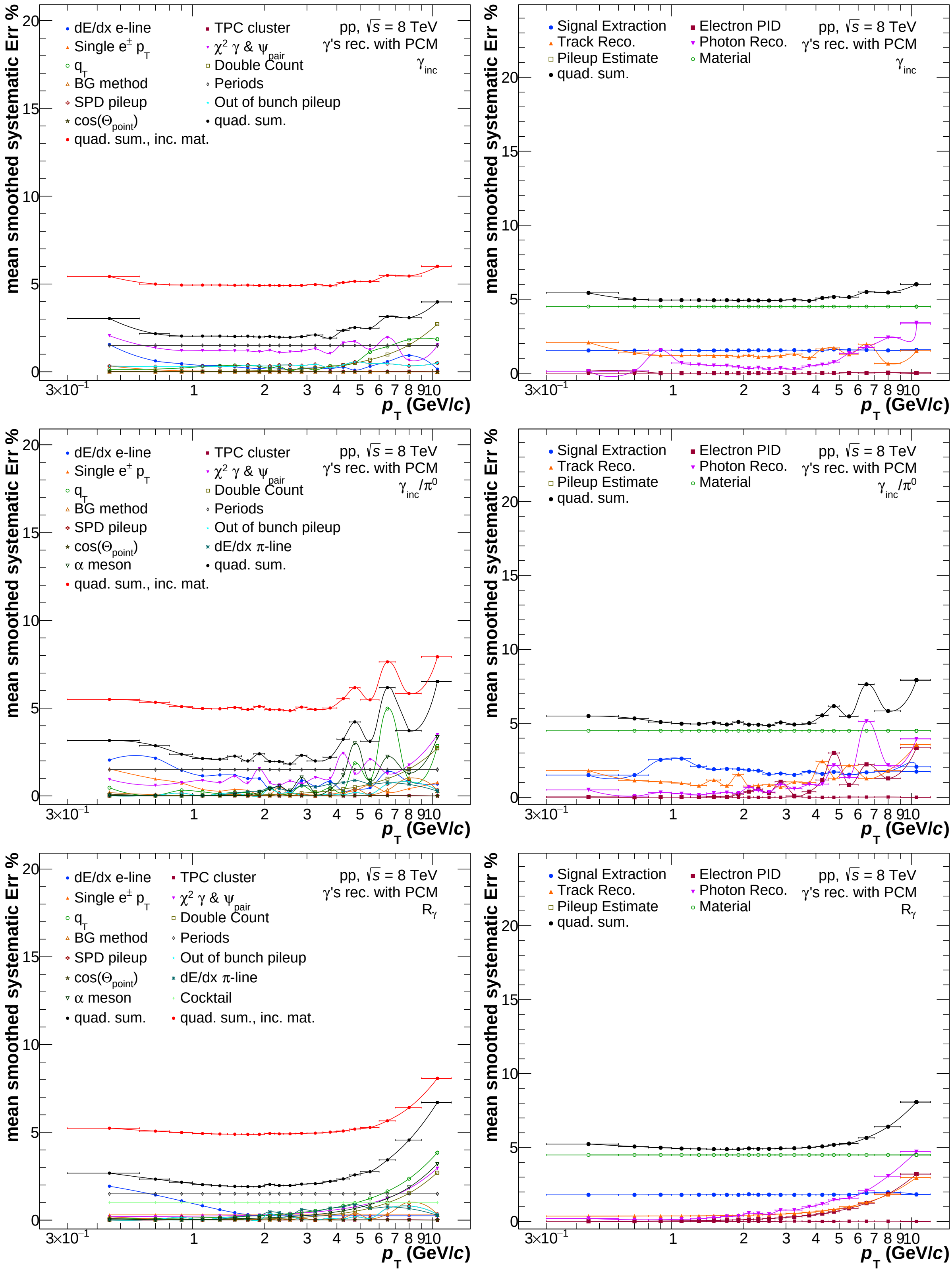

Figure C.16: Left: Detailed systematic uncertainty contributions from all sources. **Right:** Combined systematic uncertainties in different categories. Points shown for the $\sqrt{s} = 8$ TeV inclusive photons, the γ/π^0 ratio and the double ratio R_γ from top to bottom.

D Acronyms and Technical Terms

ACORDE	ALICE cosmic ray detector
ALICE	A Large Ion Collider Experiment
ATLAS	A Toroidal LHC Apparatus
CERN	European Organization for Nuclear Research
CMS	Compact Muon Solenoid experiment
DCA	distance of closest approach
DPM	Dual Parton Model
EMCal	Electromagnetic Calorimeter
FWHM	full width at half maximum
HMPID	High Momentum Particle Identification Detector
ITS	Inner Tracking System
LEP	Large Electron Positron Collider
LHC	Large Hadron Collider
LHCb	LHC beauty experiment
LINACS	Linear Accelerators
LO	Leading Order
LQCD	Lattice QCD
MB	Minimum Bias
MC	Monte Carlo
PHOS	Photon Spectrometer
PCM	Photon Conversion Method
PID	particle identification
PS	Proton Synchrotron
PSB	Proton Synchrotron Booster
QA	Quality Assurance
QCD	Quantum Chromodynamics
QED	Quantum Electrodynamics

QFT	Quantum Field Theory
QGP	Quark-Gluon Plasma
SDD	Silicon Drift Detector
SM	Standard Model
SPD	Silicon Pixel Detector
SPS	Super Proton Synchrotron
SSD	Silicon Strip Detector
TOF	Time-Of-Flight detector
TPC	Time Projection Chamber
TRD	Transition Radiation Detector
V^0	Unknown Particle

References

[1] C.P. Burgess and G.D. Moore. "The standard model: A primer". In: (2007).

[2] P. W. Higgs. "Broken Symmetries and the Masses of Gauge Bosons". In: *Phys.Rev.Lett.* 13 (1964), pp. 508–509. DOI: `10.1103/PhysRevLett.13.508`.

[3] F. Englert and R. Brout. "Broken Symmetry and the Mass of Gauge Vector Mesons". In: *Phys.Rev.Lett.* 13 (1964), pp. 321–323. DOI: `10.1103/PhysRevLett.13.321`.

[4] K. Nakamura et al. "Review of particle physics". In: *J.Phys.* G37 (2010), p. 075021. DOI: `10.1088/0954-3899/37/7A/075021`.

[5] E. M. Henley and A. L. Garcia. "Subatomic Physics". In: *World Scientific* (2007).

[6] R. Aaij et al. "Observation of $J/\psi p$ Resonances Consistent with Pentaquark States in $\Lambda_b^0 \to J/\psi K^- p$ Decays". In: *Phys. Rev. Lett.* 115 (7 2015), p. 072001. DOI: `10.1103/PhysRevLett.115.072001`. URL: `http://link.aps.org/doi/10.1103/PhysRevLett.115.072001`.

[7] H.D. Politzer. "Reliable Perturbative Results for Strong Interactions?" In: *Phys.Rev.Lett.* 30 (1973), pp. 1346–1349. DOI: `10.1103/PhysRevLett.30.1346`.

[8] Francis Halzen and Alan Martin. *Quarks & Leptons: An introductory course in modern particle physics.* New York, USA: John Wiley & Sons, 1984.

[9] R. K. Ellis, W. J. Stirling, and B.R. Webber. *QCD and collider physics.* Vol. 8. Cambridge University Press, 1996, pp. 1–435. DOI: `ISBN:978-0521545891`.

[10] Leonardo Giusti et al. "The QCD chiral condensate from the lattice". In: *Nucl. Phys.* B538 (1999), pp. 249–277. DOI: `10.1016/S0550-3213(98)00659-2`. arXiv: `hep-lat/9807014 [hep-lat]`.

[11] C.P. Burgess. "Goldstone and Pseudo-Goldstone Bosons in Nuclear, Particle and Condensed-Matter Physics". In: (1998). eprint: `arXiv:hep-th/9808176v3`.

[12] G. Aad {\it et al.} [ATLAS Collaboration]. "Observation of a new particle in the search for the Standard Model Higgs boson with the ATLAS detector at the LHC". In: *Physics Letters B* 716.1 (2012), pp. 1–29. ISSN: 03702693. DOI: `10.1016/j.physletb.2012.08.020`. arXiv: `1207.7214`. URL: `http://arxiv.org/abs/1207.7214`.

[13] Kirti Ranjan. "Observation of a new boson at the LHC with the CMS Experiment". In: *Nuclear Physics B - Proceedings Supplements* 251-252 (2014), pp. 129–134. ISSN: 09205632. DOI: `10.1016/j.nuclphysbps.2014.04.022`. arXiv: `1207.7235`.

[14] S. Datta J. van der Heide C. Jung F. Karsch O. Kaczmarek E. Laermann R. D. Mawhinney C. Miao P. Petreczky K. Petrov C. Schmidt T. Umeda M. Cheng N. H. Christ. "The transition temperature in QCD". In: *Phys.Rev* D74:054507,2006 (2006). DOI: `10.1103/PhysRevD.74.054507`. arXiv: `hep-lat/0608013 [hep-lat]`.

[15] R. Hagedorn. "Statistical thermodynamics of strong interactions at high-energies". In: *Nuovo Cim. Suppl.* 3 (1965), pp. 147–186.

[16] R. J. Fries and B. Müller. “Heavy ions at LHC: Theoretical issues”. In: *Eur.Phys.J.* C34 (2004), S279–S285. DOI: `10.1140/epjcd/s2004-04-026-6`. arXiv: `nucl-th/0307043 [nucl-th]`.

[17] Y. Aoki et al. “The QCD transition temperature: results with physical masses in the continuum limit II.” In: *JHEP* 0906 (2009), p. 088. DOI: `10.1088/1126-6708/2009/06/088`. arXiv: `0903.4155 [hep-lat]`.

[18] M. Cheng et al. “The Transition temperature in QCD”. In: *Phys.Rev.* D74 (2006), p. 054507. DOI: `10.1103/PhysRevD.74.054507`. arXiv: `hep-lat/0608013 [hep-lat]`.

[19] F. Karsch, E. Laermann, and A. Peikert. “The Pressure in two flavor, (2+1)-flavor and three flavor QCD”. In: *Phys. Lett.* B478 (2000), pp. 447–455. DOI: `10.1016/S0370-2693(00)00292-6`. arXiv: `hep-lat/0002003 [hep-lat]`.

[20] F. Karsch. “Lattice QCD at high temperature and density”. In: *Lect.Notes Phys.* 583 (2002), pp. 209–249. arXiv: `hep-lat/0106019 [hep-lat]`.

[21] Dirk H. Rischke. “The Quark gluon plasma in equilibrium”. In: *Prog. Part. Nucl. Phys.* 52 (2004), pp. 197–296. DOI: `10.1016/j.ppnp.2003.09.002`. arXiv: `nucl-th/0305030 [nucl-th]`.

[22] Mark G. Alford et al. “Color superconductivity in dense quark matter”. In: *Rev. Mod. Phys.* 80 (2008), pp. 1455–1515. DOI: `10.1103/RevModPhys.80.1455`. arXiv: `0709.4635 [hep-ph]`.

[23] A. Bazavov et al. “Equation of state in (2+1)-flavor QCD”. In: *Phys. Rev.* D90 (2014), p. 094503. DOI: `10.1103/PhysRevD.90.094503`. arXiv: `1407.6387 [hep-lat]`.

[24] Szabolcs Borsanyi et al. “The QCD equation of state with dynamical quarks”. In: *JHEP* 11 (2010), p. 077. DOI: `10.1007/JHEP11(2010)077`. arXiv: `1007.2580 [hep-lat]`.

[25] X.-F. Chen et al. “Suppression of high p_T hadrons in $Pb+Pb$ Collisions at LHC”. In: *Phys.Rev.* C84 (2011), p. 034902. DOI: `10.1103/PhysRevC.84.034902`. arXiv: `1102.5614 [nucl-th]`.

[26] K. Adcox et al. “Suppression of Hadrons with Large Transverse Momentum in Central $Au+Au$ Collisions at $\sqrt{s_{\mathrm{NN}}} = 130\mathrm{GeV}$”. In: *Phys. Rev. Lett.* 88 (2 2001), p. 022301. DOI: `10.1103/PhysRevLett.88.022301`. URL: `http://link.aps.org/doi/10.1103/PhysRevLett.88.022301`.

[27] A. Adare et al. “Suppression pattern of neutral pions at high transverse momentum in Au+Au collisions at $\sqrt{s_{\mathrm{NN}}} = 200$ GeV and constraints on medium transport coefficients”. In: *Phys. Rev. Lett.* 101 (2008), p. 232301. DOI: `10.1103/PhysRevLett.101.232301`. arXiv: `0801.4020 [nucl-ex]`.

[28] J. et al. (Particle Data Group) Beringer. “Review of Particle Physics”. In: *Phys. Rev. D* 86 (1 2012), p. 010001. DOI: `10.1103/PhysRevD.86.010001`. URL: `http://link.aps.org/doi/10.1103/PhysRevD.86.010001`.

[29] B. M. K. Nefkens and J. W. Price. “The Neutral decay modes of the eta meson”. In: *Phys. Scripta* T99 (2002), pp. 114–122. DOI: `10.1238/Physica.Topical.099a00114`. arXiv: `nucl-ex/0202008 [nucl-ex]`.

[30] L. D. McLerran and T. Toimela. “Photon and dilepton emission from the quark-gluon plasma: Some general considerations”. In: *Phys. Rev. D* 31 (3 1985), pp. 545–563. DOI: `10.1103/PhysRevD.31.545`. URL: `http://link.aps.org/doi/10.1103/PhysRevD.31.545`.

[31] Cinzia De Melis. “The CERN accelerator complex. Complexe des accélérateurs du CERN”. In: (2016). General Photo. URL: `http://cds.cern.ch/record/2119882`.

[32] (ed.) Evans L. and (ed.) Bryant P. “LHC Machine”. In: *JINST* 3 (2008), S08001. DOI: `10.1088/1748-0221/3/08/S08001`.

[33] Michael Benedikt et al. *LHC Design Report*. Geneva: CERN, 2004. URL: `https://cds.cern.ch/record/823808`.

[34] ATLAS Collaboration. “The ATLAS Experiment at the CERN Large Hadron Collider”. In: *Journal of Instrumentation* (2008). URL: `stacks.iop.org/1748-0221/3/i=08/a=S08003`.

[35] S. Chatrchyan et al. “The CMS experiment at the CERN LHC”. In: *JINST* 3 (2008), S08004. DOI: `10.1088/1748-0221/3/08/S08004`.

[36] LHCb Collaboration. “The LHCb Detector at the LHC”. In: *JINST* 3:S08003 (2008).

[37] Betty Bezverkhny Abelev et al. “Performance of the ALICE Experiment at the CERN LHC”. In: *Int. J. Mod. Phys.* A29 (2014), p. 1430044. DOI: `10.1142/S0217751X14300440`. arXiv: `1402.4476 [nucl-ex]`.

[38] K. Aamodt et al. “The ALICE experiment at the CERN LHC”. In: *JINST* 3 (2008), S08002. DOI: `10.1088/1748-0221/3/08/S08002`.

[39] B. Alessandro et al. “ALICE: Physics performance report, volume II”. In: *Journal of Physics G: Nuclear and Particle Physics* 32 (2006), pp. 1295–2040.

[40] ALICE Collaboration. “The ALICE Experiment at the CERN LHC”. In: *Journal of Instrumentation* 08 S08003 (2008).

[41] P Cortese et al. *ALICE forward detectors: FMD, TO and VO: Technical Design Report*. Technical Design Report ALICE. Submitted on 10 Sep 2004. Geneva: CERN, 2004. URL: `https://cds.cern.ch/record/781854`.

[42] E. Abbas et al. “Performance of the ALICE VZERO system”. In: *JINST* 8 (2013), P10016. DOI: `10.1088/1748-0221/8/10/P10016`. arXiv: `1306.3130 [nucl-ex]`.

[43] G. Dellacasa et al. “ALICE technical design report of the inner tracking system (ITS)”. In: (1999).

[44] J. Alme et al. “The ALICE TPC, a large 3-dimensional tracking device with fast readout for ultra-high multiplicity events”. In: *Nucl.Instrum.Meth.* A622 (2010), pp. 316–367. DOI: `10.1016/j.nima.2010.04.042`. arXiv: `1001.1950`.

[45] C. Garabatos. “The ALICE TPC”. In: *Nuclear Instruments and Methods in Physics Research A* 535 (Dec. 2004), pp. 197–200. DOI: `10.1016/j.nima.2004.07.127`.

[46] *Root webpage*. URL: `http://root.cern.ch/`.

[47] *AliRoot-Software*. ALICE Collaboration. URL: `http://git.cern.ch/pubweb/AliRoot.git`.

[48] *AliPhysics-Software.* ALICE Collaboration. URL: `http://git.cern.ch/pubweb/AliPhysics.git`.

[49] *Clang: a C language family frontend for LLVM.* URL: `http://clang.llvm.org/`.

[50] T. Sjöstrand, S. Mrenna, and P. Z. Skands. "PYTHIA 6.4 Physics and Manual". In: *JHEP* 0605 (2006), p. 026. DOI: `10.1088/1126-6708/2006/05/026`. arXiv: `hep-ph/0603175 [hep-ph]`.

[51] T. Sjöstrand, S. Mrenna, and P. Z. Skands. "A Brief Introduction to PYTHIA 8.1". In: *Comput.Phys.Commun.* 178 (2008), pp. 852–867. DOI: `10.1016/j.cpc.2008.01.036`. arXiv: `0710.3820 [hep-ph]`.

[52] T. Sjöstrand. "PYTHIA 8 Status Report". In: (2008), pp. 726–732. arXiv: `0809.0303 [hep-ph]`.

[53] R. Engel. "PHOJET manual". In: *University of Siegen preprint* (1995), pp. 95–05.

[54] R. Brun et al. "GEANT3". In: (1987).

[55] S. Agostinelli et al. "GEANT4: A Simulation toolkit". In: *Nucl.Instrum.Meth.* A506 (2003), pp. 250–303. DOI: `10.1016/S0168-9002(03)01368-8`.

[56] *Run condition table.* URL: `https://alimonitor.cern.ch/configuration/`.

[57] R. Engel, J. Ranft, and S. Roesler. "Hard diffraction in hadron hadron interactions and in photoproduction". In: *Phys.Rev.* D52 (1995), pp. 1459–1468. DOI: `10.1103/PhysRevD.52.1459`. arXiv: `hep-ph/9502319 [hep-ph]`.

[58] B. Andersson, S. Mohanty, and F. Söderberg. "Recent developments in the Lund model". In: (2002). arXiv: `hep-ph/0212122 [hep-ph]`.

[59] A. Capella et al. "Dual parton model". In: *Phys.Rept.* 236 (1994), pp. 225–329. DOI: `10.1016/0370-1573(94)90064-7`.

[60] DESY Armen Buniatian. "Large Transverse Energies and Jets in Hard Photoproduction at HERA". In: (1995).

[61] P. Aurenche et al. "Multiparticle production in a two-component dual parton model". In: *Phys. Rev. D* 45 (1 1992), pp. 92–105. DOI: `10.1103/PhysRevD.45.92`. URL: `http://link.aps.org/doi/10.1103/PhysRevD.45.92`.

[62] B. Abelev et al. "Measurement of inelastic, single- and double-diffraction cross sections in proton–proton collisions at the LHC with ALICE". In: *Eur. Phys. J. C* (2012). arXiv: `1208.4968 [hep-ex]`.

[63] ALICE Collaboration. "ALICE luminosity determination for pp collisions at $sqrts = 8$ TeV". In: (2017). URL: `https://aliceinfo.cern.ch/Notes/node/583`.

[64] E Bruna et al. "Vertex reconstruction for proton-proton collisions in ALICE". In: (2009). URL: `https://cds.cern.ch/record/1225497`.

[65] J. Podolanski and R. Armenteros. "ANALYSIS OF V-EVENTS". In: *Phil. Mag.* 7 (1954).

[66] S. Gorbunov and I. Kisel. *AliKF Package.* URL: `{http://alisoft.cern.ch/viewvc/branches/v4-18-Release/STEER/AliKFParticle.h}`.

[67] T. Dahms. “Measurement of photons via conversion ppair with the PHENIX experiment at RHIC”. MA thesis. Stony Brook University, May 2005.

[68] Betty Bezverkhny Abelev et al. “Neutral pion production at midrapidity in pp and Pb-Pb collisions at $\sqrt{s_{NN}} = 2.76$ TeV”. In: (2014). arXiv: `1405.3794 [nucl-ex]`.

[69] K. Aamodt. “Photon, π^0 and η measurements in proton-proton collisions at $\sqrt{s} =$ 7 TeV with the ALICE TPC at the LHC”. PHD thesis. University of Oslo, 2011.

[70] K. Koch. “Measurement of π^0 and η mesons with photon conversions in ALICE in proton-proton collisions at $\sqrt{s} = 0.9$, 2.76, 7 TeV”. PhD thesis. University of Heidelberg, 2012. URL: `http://www.ub.uni-heidelberg.de/archiv/13113`.

[71] Christoph Schwick Jamie Boyd. *LHC Programme Coordination web pages*. CERN. URL: `http://lpc.web.cern.ch/`.

[72] K Aamodt et al. “Production of pions, kaons and protons in pp collisions at $\sqrt{s}$ = 900 GeV with ALICE at the LHC”. In: *Eur. Phys. J. C* 71.arXiv:1101.4110. CERN-PH-EP-2010-085 (2010). Comments: 30 pages, 18 figures, 1655. 30 p. URL: `https://cds.cern.ch/record/1314539`.

[73] Jaroslav Adam et al. “Measurement of pion, kaon and proton production in proton–proton collisions at $\sqrt{s} = 7$ TeV”. In: *Eur. Phys. J.* C75.5 (2015), p. 226. DOI: `10.1140/epjc/s10052-015-3422-9`. arXiv: `1504.00024 [nucl-ex]`.

[74] Betty Bezverkhny Abelev et al. “Production of charged pions, kaons and protons at large transverse momenta in pp and Pb–Pb collisions at $\sqrt{s_{\rm NN}}$ =2.76 TeV”. In: *Phys. Lett.* B736 (2014), pp. 196–207. DOI: `10.1016/j.physletb.2014.07.011`. arXiv: `1401.1250 [nucl-ex]`.

[75] C. Tsallis. “Possible Generalization of Boltzmann-Gibbs Statistics”. In: *J.Statist.Phys.* 52 (1988), pp. 479–487. DOI: `10.1007/BF01016429`.

[76] F. Bock. “Neutral Pion and Eta Meson Production in pp and Pb–Pb Collisions at the LHC with the ALICE Detector”. MA thesis. University Heidelberg, 2012. URL: `http://www.physi.uni-heidelberg.de//Publications/Bock-Masterthesis.pdf`.

[77] Nicolas Vincent Schmidt. “Neutral meson measurements with the photon conversion method in ALICE in pp Collisions at sqrt(s)=8 TeV”. ALICE Analysis Note. URL: `https://aliceinfo.cern.ch/Notes/node/490`.

[78] Satoshi Yano. “Measurement of pi0 production in pp collisions at 8 TeV with PHOS”. ALICE Analysis Note. URL: `https://aliceinfo.cern.ch/Notes/node/385`.

[79] Daniel Michael Muhlheim. “Neutral meson measurements with EMCal in ALICE in pp collisions at 8 TeV”. ALICE Analysis Note. URL: `https://aliceinfo.cern.ch/Notes/node/489`.

[80] Daniel Michael Muhlheim. “Neutral meson measurements with PCM-EMCal in ALICE in pp collisions at 8 TeV”. ALICE Analysis Note. URL: `https://aliceinfo.cern.ch/Notes/node/411`.

[81] Daniel Michael Muhlheim. “Combination of different neutral meson measurements at 8 TeV”. ALICE Analysis Note. URL: `https://aliceinfo.cern.ch/Notes/node/522`.

[82] Nicolas Vincent Schmidt. “Neutral meson and direct photon measurements using the photon conversion method with ALICE in pp collisions at sqrt(s)=7 TeV”. ALICE Analysis Note. URL: `https://aliceinfo.cern.ch/Notes/node/567`.

[83] Paraskevi Ganoti. “Neutral mesons production in p+p collisions at 7TeV with EMCal”. ALICE Analysis Note. URL: `https://aliceinfo.cern.ch/Notes/node/212`.

[84] Daniel Michael Muhlheim. “Neutral meson measurements with PCM-EMCal in ALICE in pp collisions at 7 TeV”. Analysis Note not yet available.

[85] B. Abelev et al. “Neutral pion and η meson production in proton-proton collisions at $\sqrt{s} = 0.9$ TeV and $\sqrt{s} = 7$ TeV”. In: *Phys.Lett.* B717 (2012), pp. 162–172. DOI: `10.1016/j.physletb.2012.09.015`. arXiv: `1205.5724 [hep-ex]`.

[86] Louis Lyons, Duncan Gibaut, and Peter Clifford. “How to Combine Correlated Estimates of a Single Physical Quantity”. In: *Nucl. Instrum. Meth.* A270 (1988), p. 110. DOI: `10.1016/0168-9002(88)90018-6`.

[87] Alexander Bylinkin, Nadezda S. Chernyavskaya, and Andrei A. Rostovtsev. “Predictions on the transverse momentum spectra for charged particle production at LHC-energies from a two component model”. In: *Eur. Phys. J.* C75.4 (2015), p. 166. DOI: `10.1140/epjc/s10052-015-3392-y`. arXiv: `1501.05235 [hep-ph]`.

[88] R. S. Thorne et al. “Status of MRST/MSTW PDF sets”. In: *Proceedings, 17th International Workshop on Deep-Inelastic Scattering and Related Subjects (DIS 2009): Madrid, Spain, April 26-30, 2009.* 2009. arXiv: `0907.2387 [hep-ph]`. URL: `https://inspirehep.net/record/825642/files/arXiv:0907.2387.pdf`.

[89] Daniel de Florian et al. “Parton-to-Pion Fragmentation Reloaded”. In: *Phys. Rev.* D91.1 (2015), p. 014035. DOI: `10.1103/PhysRevD.91.014035`. arXiv: `1410.6027 [hep-ph]`.

[90] Christine A. Aidala et al. “Global Analysis of Fragmentation Functions for Eta Mesons”. In: *Phys. Rev.* D83 (2011), p. 034002. DOI: `10.1103/PhysRevD.83.034002`. arXiv: `1009.6145 [hep-ph]`.

[91] Torbjörn Sjöstrand et al. “An Introduction to PYTHIA 8.2”. In: *Comput. Phys. Commun.* 191 (2015), pp. 159–177. DOI: `10.1016/j.cpc.2015.01.024`. arXiv: `1410.3012 [hep-ph]`.

[92] Peter Skands, Stefano Carrazza, and Juan Rojo. “Tuning PYTHIA 8.1: the Monash 2013 Tune”. In: *Eur. Phys. J.* C74.8 (2014), p. 3024. DOI: `10.1140/epjc/s10052-014-3024-y`. arXiv: `1404.5630 [hep-ph]`.

[93] Serguei Chatrchyan et al. “Study of the inclusive production of charged pions, kaons, and protons in *pp* collisions at $\sqrt{s} = 0.9$, 2.76, and 7 TeV”. In: *Eur.Phys.J.* C72 (2012), p. 2164. DOI: `10.1140/epjc/s10052-012-2164-1`. arXiv: `1207.4724 [hep-ex]`.

[94] Tim Adye. “Unfolding algorithms and tests using RooUnfold”. In: *Proceedings, PHYSTAT 2011 Workshop on Statistical Issues Related to Discovery Claims in Search Experiments and Unfolding, CERN,Geneva, Switzerland 17-20 January 2011.* CERN. Geneva: CERN, 2011, pp. 313–318. DOI: `10.5170/CERN-2011-006.313`. arXiv: `1105.1160 [physics.data-an]`. URL: `https://inspirehep.net/record/898599/files/arXiv:1105.1160.pdf`.

[95] Andreas Hocker and Vakhtang Kartvelishvili. “SVD approach to data unfolding”. In: *Nucl. Instrum. Meth.* A372 (1996), pp. 469–481. DOI: `10.1016/0168-9002(95)01478-0`. arXiv: `hep-ph/9509307 [hep-ph]`.

[96] Lucas Altenkämper. “Measurement of Direct Photons in Proton-Proton Collisions at $\sqrt{s} = 7$ TeV with ALICE”. MA thesis. PI University of Heidelberg, 2017.

[97] K. A. Olive et al. “Review of Particle Physics”. In: *Chin. Phys.* C38 (2014), p. 090001. DOI: `10.1088/1674-1137/38/9/090001`.

[98] Riabov, Viktor. “Omega production measured in the $\pi^+\pi^-\pi^0$ channel in pp collisions at 7 TeV”. In: *ALICE Analysis Note* (2012). ISSN: ANA-233. URL: `https://aliceinfo.cern.ch/Notes/node/90`.

[99] Betty Abelev et al. “Production of $K^*(892)^0$ and $\phi(1020)$ in *pp* collisions at $\sqrt{s} = 7$ TeV”. In: *Eur. Phys. J.* C72 (2012), p. 2183. DOI: `10.1140/epjc/s10052-012-2183-y`. arXiv: `1208.5717 [hep-ex]`.

[100] Jaroslav Adam et al. “Multiplicity-dependent enhancement of strange and multi-strange hadron production in proton-proton collisions at $\sqrt{s} = 7$ TeV”. In: (2016). arXiv: `1606.07424 [nucl-ex]`.

[101] K. Aamodt et al. “Strange particle production in proton-proton collisions at $\sqrt{(s)} = 0.9$ TeV with ALICE at the LHC”. In: *Eur.Phys.J.* C71 (2011), p. 1594. DOI: `10.1140/epjc/s10052-011-1594-5`. arXiv: `1012.3257 [hep-ex]`.

[102] Stephan Stiefelmaier. “A new weights approach for the material budget estimation.” MA thesis. University Heidelberg, 2017.

Acknowledgements

I'd like to thank Prof. Dr. Johanna Stachel and my supervisor apl. Prof. Dr. Klaus Reygers for giving me the opportunity to be a part of the PI Heidelberg photon group. Within this group I was able to carry out my bachelors and my masters thesis with huge support from everyone.

My greatest gratitude goes towards Friederike Bock who supported me throughout my thesis and served as a source of inspiration and motivation. She always found a way to let me further improve my work and provided great advice to overcome obstacles on the way.

Furthermore, I'd like to thank the remaining members of the PCM group, Dr. Ana Marin, Lucia Leardini, Lucas Altenkämper and Daniel Mühlheim, who provided fruitful discussions and advice. With the combined effort of everyone in the group, it was possible to resolve general problems in the analysis quickly.

I'd also wish to express my greatest gratitude to my family and friends for supporting me during my time in Heidelberg and always having an open ear for my matters.

I greatly appreciate the effort of Lucas Altenkämper, Meike Danisch, Lucia Leardini, Friederike Bock as well as my mother who were proof-reading my thesis and suggested useful improvements.

Erklärung

Ich versichere, dass ich diese Arbeit selbstständig verfasst und keine anderen als die angegebenen Quellen und Hilfsmittel benutzt habe.

Heidelberg, March 7, 2017 Unterschrift: ....
Nicolas Schmidt